Parametric System Identification of Rocket Combustion Instability Using the Fokker-Planck Equation

Pablo Nicolas Blanco

Principal Supervisor: Prof Bassam Dally

External Supervisors: Dr Justin Hardi, Prof Michael Oschwald

Parametric System Identification of Rocket Combustion Instability Using the Fokker-Planck Equation

Pablo Nicolas Blanco

School of Mechanical Engineering

The University of Adelaide

South Australia 5005

Australia

A thesis submitted in fulfilment of the requirements for the degree of MPhil in Mechanical Engineering

June 2018

Contents

List of Figures

List of Tables

Symbols

$p'(t)$	Acoustic pressure
t	Time
ν	Growth rate
β	Thermo-acoustic driving rate
α	Damping rate
ω	Frequency
ω_0	Natural frequency
$\xi(t)$	Stochastic heat release forcing
$\dot{q}(t)$	Heat release forcing (sum of deterministic and stochastic)
$\gamma\dot{q}(t)$	Heat release forcing term
κ	Non-linearity coefficient
$A(t)$	Amplitude envelope of acoustic pressure
$A'(t)$	Fluctuation of amplitude envelope about mean
$\overline{A}$	Mean of amplitude envelope
A_0	Deterministic amplitude envelope
Γ	White noise intensity (PSD height of stochastic heat release forcing $\xi(t)$)
c_0	Noise intensity coefficient
M	Maximum of Lorentzian fit to PSD of acoustic pressure
$S_{p'p'}(\omega)$	PSD (two-sided) of acoustic pressure
$S_{A'A'}(\omega)$	PSD (two-sided) of amplitude envelope fluctuation
$P(A)$	Stationary Fokker-Planck probability density function
$P(A,t)$	Evolving Fokker-Planck probability density function
$\mathcal{F}(A)$	Drift coefficient of the Fokker-Planck equation
$\mathcal{F}_A(A,\breve{B})$	Drift coefficient for the standing A mode component of a rotating transverse mode
$\mathcal{F}_B(\breve{A},B)$	Drift coefficient for the standing B mode component of a rotating transverse mode
$D_\tau^{(1)}$	First transition moment
$D_\tau^{(2)}$	Second transition moment
$B(t)$	Amplitude envelope of the standing B mode component of a rotating transverse mode
$\phi(t)$	Phase difference between the standing A and B modes of a rotating transverse mode

Acronyms

DLR	German Aerospace Centre
CNRS	French National Scientific Research Centre
ONERA	French National Aerospace Research Centre
LPRE	Liquid Propellant Rocket Engine
BKD	Combustion Chamber D (German: *Brennkammer D*)
BKH	Combustion Chamber H (German: *Brennkammer H*)
1L	First Longitudinal mode
1T	First Transverse (rectangular chamber) or Tangential (cylindrical chamber) mode
1L1T	First Longitudinal-Transverse mode
LOx	Liquid Oxygen
CRC	Common Research Combustor
MIC	Multi Injector Combustor
LHS	Left Hand Side
RHS	Right Hand Side
HF	High Frequency
ROF	Ratio of Oxidiser-to-Fuel Mass Flow
VR	Velocity Ratio
LH2	Liquid Hydrogen
GH2	Gaseous Hydrogen
PSD	Power Spectral Density
HWHM	Half Width Half Maximum
PDF	Probability Density Function
rms	root mean square

Abstract

This project seeks to advance understanding of thermo-acoustic instabilities in liquid-propellant rocket engines (LPREs). Unstable thermo-acoustic coupling between combustion and acoustic modes in a rocket engine thrust chamber can lead to high pressure oscillations and subsequent structural damage. Since the mechanisms involved are not yet fully understood, engine stability cannot be assured at the design stage. Consequently, costly ground testing is required such as that undertaken at the German Aerospace Centre (DLR) site in Lampoldshausen for Ariane engines. A deeper understanding of instabilities would reduce ground testing requirements, and allow for more economical rocket engine development.

This project, conducted in conjunction with the DLR, aims to extract key parameters governing thermo-acoustic behaviour in rocket combustors from dynamic pressure measurements using stochastic signal processing techniques. These system-defining parameters are the linear thermo-acoustic growth rate, the noise intensity of turbulence-induced stochastic heat release, and the coefficient of non-linear acoustic damping. In particular, knowledge of the growth rate would allow the efficient design of retrofitted acoustic dampers and the validation of linear thermo-acoustic models. Current parameter extraction methods in rocket literature are limited to stable (linear) conditions. In these conditions, a Lorentzian fit to the power spectral density of dynamic (acoustic) pressure is commonly used to find the growth rate. For unstable (non-linear) cases, the initially linear growth of instability is not directly observed by wall sensors due to time scale differences between localised thermo-acoustic effects and the response of acoustic chamber modes. The noise intensity and non-linearity coefficient are also not readily observable at non-linear conditions. In gas turbine literature, signal processing techniques based on the Fokker-Planck equation have been developed to extract system parameters from the statistics of unstable combustor data. The project focuses on applying these techniques to rocket engine conditions.

Fokker-Planck parameter extraction techniques have been applied to experimental data from two rocket combustors named 'BKH' and 'BKD', both operated at the DLR Lampoldshausen test site. These are representative of real rocket engine conditions; operating at sufficiently high pressures and flow rates with liquid oxygen/hydrogen propellants. While BKH is a rectangular and stable combustor, BKD is cylindrical and naturally unstable at some load points. Acoustic modes in BKH are purely standing, while in BKD they exhibited rotational characteristics, as occurs in real engines. This is significant since the parameter extraction techniques have different formulations for standing and rotational mode behaviour. This project has tested the two formulations of the Fokker-Planck techniques on BKH and BKD experimental data.

The Fokker-Planck parameter extraction techniques have been validated for stable BKH and BKD load points using Lorentzian fits, while positive indications of their applicability to an unstable BKD load point have been obtained. These indications consist of comparing the statistical phase behaviour of the unstable BKD load point to that of a stable load point, and observing differences which support the non-linear dynamical model assumed in the techniques.

Declaration of Originality

I certify that this work contains no material which has been accepted for the award of any other degree or diploma in my name in any university or other tertiary institution and, to the best of my knowledge and belief, contains no material previously published or written by another person, except where due reference has been made in the text. In addition, I certify that no part of this work will, in the future, be used in a submission in my name for any other degree or diploma in any university or other tertiary institution without the prior approval of the University of Adelaide and where applicable, any partner institution responsible for the joint award of this degree. I give permission for the digital version of my thesis to be made available on the web, via the University's digital research repository, the Library Search and also through web search engines, unless permission has been granted by the University to restrict access for a period of time.

I acknowledge the support I have received for my research through the provision of an Australian Government Research Training Program Scholarship.

Pablo Nicolas Blanco

June 2018

Acknowledgements and Disclaimer

I would like to acknowledge my supervisors Prof Bassam Dally and Prof Michael Oschwald for making my stay at the DLR in Germany possible. I had a very interesting time and gained many new experiences and skills for which I am grateful.

Special thanks go to my direct supervisor at the DLR, Dr Justin Hardi, for his generous help during my stay in Germany and his valuable assistance while undertaking research into rocket combustion instability.

This thesis would not have been possible without the collaborative help of Prof Nicolas Noiray and his team at ETH Zurich. Hence, I wish to express my gratitude to them for their guidance in applying the stochastic signal processing methods used in this work.

I would like to thank my family for their continued support during my overseas experience.

Finally, I thank Germany and many of its people who have been particularly kind to me.

This research project is sponsored with a grant from the Sir Ross and Sir Keith Smith Fund. Their funding support is acknowledged and appreciated.

THE SIR ROSS & SIR KEITH SMITH FUND

1. Introduction

Combustion instabilities were first encountered in liquid-propellant rocket engines (LPREs) in the 1930s, and since that time they have been problematic to most rocket development programs (Culick & Yang, 1995). Combustion inherently involves pressure fluctuations in the thrust chamber in the form of random noise. However, periodic pressure oscillations can also arise and are deemed to be combustion instabilities (CPIA, 1997). These can grow to levels that surpass the engine's structural integrity or that melt walls through flame undulation. High frequency (HF) instability, causing oscillations above 1000 Hz, is the most damaging type of instability. It occurs at the modal frequencies of the thrust chamber. Fuel (gaseous H_2) and oxidiser (liquid oxygen or LOx) jets enter the combustion chamber through multiple injectors where they atomise (break up into droplets), vaporise and mix in order to combust effectively. The resulting hot, high-pressure gases are then accelerated by a nozzle to maximise thrust. These combustion processes can couple thermo-acoustically with chamber modes through various mechanisms to produce HF instability. These mechanisms are not yet fully understood since they are multiple and interdependent. A fundamental part of each mechanism is Rayleigh's criterion. This states that oscillatory heat release from combustion will amplify pressure oscillations when the two are in-phase, and diminish them when out of phase (Lord Rayleigh, 1945).

Stochastic signal processing techniques to extract key parameters governing thermo-acoustic behaviour from the statistics of dynamic pressure data have been developed in gas turbine literature. These parameters are the linear thermo-acoustic growth rate, the noise intensity of turbulence-induced stochastic heat release, and the coefficient of non-linear acoustic damping; which are not directly measureable in unstable conditions. Some of the stochastic techniques have been successfully applied to data from a small-scale, unstable combustor representative of gas turbine conditions. The main motivation for the development of these techniques is that the linear growth rate of thermo-acoustic instability in a practical combustor, such as a gas turbine or rocket engine, is not directly obtainable from measurable pressure signals. This is due to a timescale difference between localised thermo-acoustic growth and the acoustic response of chamber modes (Noiray & Schuermans, IJNLM 2013). Knowledge of the growth rate is useful for the design of remedial dampers in industry, and for validating linear thermo-acoustic models commonly used for stability prediction. The stochastic techniques for extracting the growth rate and the other parameters have not been applied to rocket engine conditions.

This work consists of applying the stochastic signal processing techniques to dynamic pressure data of representative rocket combustors. The DLR facility at Lampoldshausen, Germany is one of the few facilities worldwide where combustion chambers simulating rocket engines can be operated under realistic conditions. Two combustors, named 'BKH' and 'BKD', are used by the DLR Combustion Dynamics Group to investigate HF instabilities at supercritical pressures. BKH is a stable rectangular combustor while BKD is a cylindrical chamber and naturally unstable at some operating conditions. This work applies the stochastic signal processing techniques to stable load points from both combustors in order to extract the governing thermo-acoustic parameters. These

parameter values are compared with those obtained using Lorentzian fitting; a simpler method for linearly stable dynamics. This work also analyses the non-linear phase dynamics of an unstable BKD load point to obtain insight into the underlying non-linear dynamics. This serves as a basis for future work consisting of applying the stochastic signal processing techniques to unstable BKD load points, where non-linear effects are significant and there are no alternative parameter extraction methods.

2. Literature Review

This chapter reviews literature encompassing a general background to rocket instability, the BKH and BKD combustors, the parameter extraction methods and their associated dynamical models.

2.1 Background

This section provides a general background to the literature on HF rocket instability. The most intensive industrial case of such instability was the development of the F-1 LPRE during the 1960's Apollo program. Early testing of this engine revealed acoustic oscillations equal to the mean pressure which caused significant internal damage (Culick & Yang, 1995). This instability was solved through numerous trial-and-error iterations involving different injector and internal chamber designs which amounted to over 2000 full scale tests lasting a period of four years (Culick & Yang, 1995). Rocket engines today still rely on expensive ground testing to ensure their stability; such as that carried out at the DLR Lampoldshausen for the Ariane rocket family. These costs have motivated researchers to seek a better understanding of HF instabilities in order to reduce testing requirements with the use of predictive models.

An important complication to rocket instability is the distinction between subcritical and supercritical fluid conditions. The critical pressures of oxygen and hydrogen are 50 and 13 bar, respectively. If oxygen is injected into a thrust chamber at a pressure above 50 bar, the operating condition is said to be supercritical. Rocket engines often operate in these high pressures to maximise thrust. However, atomisation and vaporisation are absent in the supercritical regime, instead a flow continuum occurs. Shadowgraph visualisation of LOx/H_2 injection at subcritical and supercritical conditions, shown in Figure 1, was carried out at the DLR by Mayer and Tamura (1996). The most noticeable differences in Figure 1 are the lack of droplet formation and the longer extension of dense structures for the supercritical condition. Supercritical instabilities therefore require separate study, and have significant literature gaps due to experimental complications (Hardi, 2012).

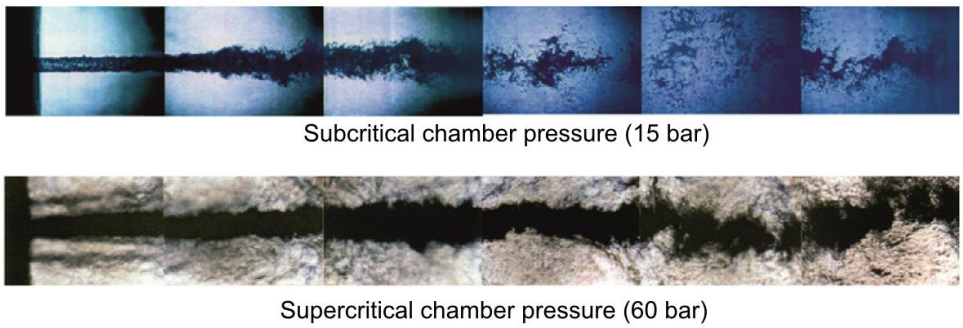

Figure 1: Differences in flow structure between subcritical and supercritical conditions of LOx/H_2 injection can be observed with shadowgraph imaging (Mayer & Tamura, 1996).

Scientific studies of HF instability focus on laboratory scale combustors that simulate LPRE conditions. These can be classified into two main types; forced and naturally unstable. Forced combustors commonly feature a nozzle wheel excitation system where a toothed wheel

periodically opens and closes a nozzle outlet to generate chamber pressure oscillations at a frequency given by the wheel's rotational speed. Three such systems are the Common Research Combustor (CRC) which is operated by the DLR and the French National Scientific Research Centre (CNRS), the Multi Injector Combustor (MIC) which is operated by the French Space Agency (ONERA), and BKH which is operated by the DLR. The CRC is a thin, quasi-2D chamber with a circular shape that allows optical observation of transverse modes with a quartz window. It has a single injection element and can only be operated up to 10 bar with LOx/H_2 propellants. The MIC has a rectangular chamber with three or five injection elements that are observable through a window, but it can only be operated up to 9 bar with the LOx/H_2 combination (Rey et al., 2004). BKH is the sole forced combustor in literature with the capacity to operate at supercritical pressures with LOx/H_2 propellants. Further description of BKH is provided in section 2.2.

Naturally unstable combustors do not have acoustic forcing but feature spontaneous instability. Three important cases in literature are the Pennsylvania State University rectangular combustor, the Purdue University rectangular combustor and the DLR cylindrical combustor 'BKD'. The first two combustors both operate with LOx/CH_4 (methane) study elements in a multi-element configuration. In the Pennsylvania combustor, any LOx/CH_4 study element is neighboured by equal elements, while in the Purdue configuration there is a single LOx/CH_4 study element surrounded by intrinsically unstable hydrogen peroxide/kerosene elements. Only the latter arrangement could generate high amplitude instability (Miller et al., 2005). BKD is a rocket combustor with LOx/H_2 propellants that naturally exhibits high amplitude unstable behaviour. Further description of BKD is in section 2.3. Hence, the BKH and BKD data available to this research project is of significant scientific value.

2.2 BKH

BKH (German: *Brennkammer H* or 'Combustion chamber H') is a DLR combustor designed to observe the acoustic response of a LOx/H_2 element with optical diagnostics at pressures up to 60 bar. Figure 2 shows a sketch of the configuration of BKH, which has chamber dimensions of 305 mm x 200 mm x 50 mm.

The rectangular geometry of BKH was designed to obtain resonant frequencies in the range 1-6 kHz; representative of those found in upper stage engines (Hardi, 2012). The BKH chamber modes for uniform acoustic properties are shown in Figure 3. Primary injection in BKH consists of five shear coaxial elements in a matrix configuration. These are five liquid jets; each has a circular LOx core surrounded by an H_2 annulus injected at a higher speed to create shear forces and effective mixing in the chamber since rocket combustion is non-premixed. The central jet is representative of real multi-element injectors where each element is bounded by others. Secondary H_2 injection comprises of smaller H_2 jets to maintain acoustic field uniformity and to prevent primary jet recirculation. Thus BKH features realistic resonant modes and propellant injection.

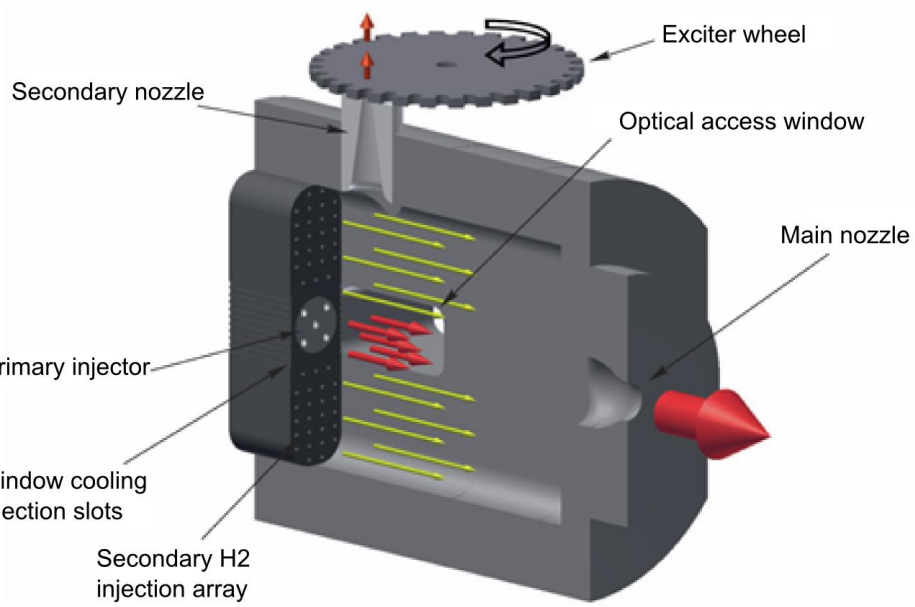

Figure 2: Sketch of the BKH configuration (Hardi, 2012).

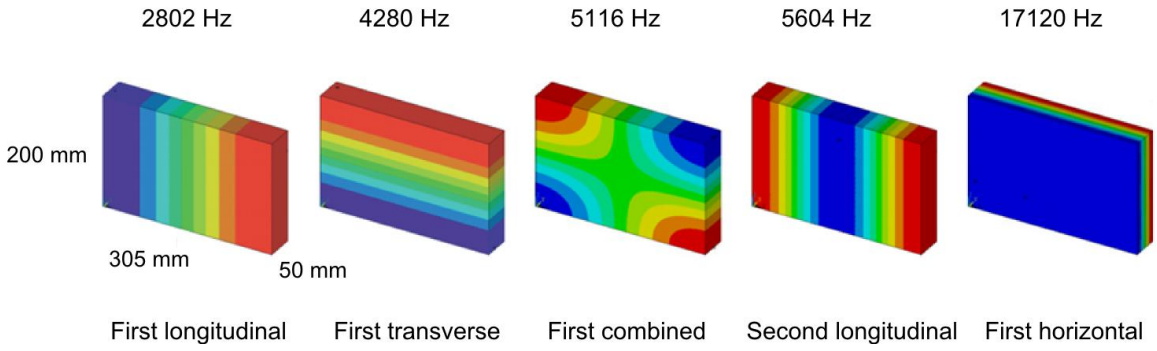

Figure 3: Calculated modal frequencies and shapes of acoustic chamber modes in BKH using uniform properties (Hardi, 2012).

The BKH flames can be externally excited by the secondary nozzle-wheel system as illustrated in Figure 2. Flame-acoustic interactions are then generated by exciting specific chamber modes. These are observed with optical windows and an extensive sensor array. Two quartz windows, each on a side of the combustor, provide optical access for shadowgraph and chemiluminescence imaging with cameras. The latter consists of using filtered ultra-violet light that is passed through an image intensifier to capture photon emission from the hydroxyl radical OH*; an intermediate species in the reaction that identifies a flame. To measure acoustic pressure, wall temperatures, and structural vibration, an array of dynamic pressure sensors, thermo-couples and accelerometers are employed. BKH thus provides insight into HF flame-acoustic interactions at realistic conditions.

An important feature of BKH is the use of sectored wheels where teeth cover only a portion of the wheel's perimeter such that the excited mode is allowed to decay. Figure 4 shows how this decay can be measured directly in order to obtain the damping rate. This method was used by Webster (2016) to measure the damping rate of various operating points in BKH.

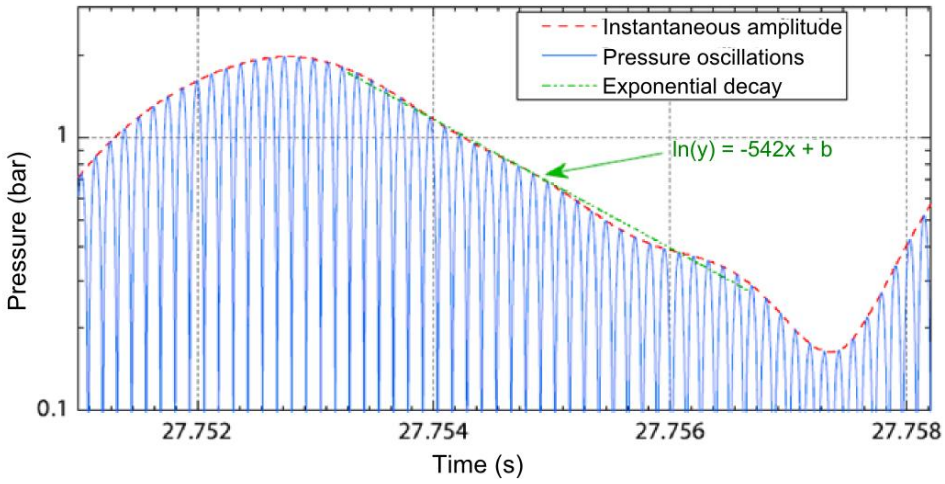

Figure 4: Exponential decay of an acoustic mode in BKH measured with linear regression to obtain the damping rate (Webster S. L., 2016).

A second method to measure the damping rate that is based on a linear ramp of nozzle wheel excitation through the mode of interest, as depicted in Figure 5, was also used by Webster (2016). This method consists of increasing the nozzle wheel rotation speed linearly (and therefore increasing the frequency of excitation linearly with time), such that the frequency response of the mode is mapped in the time domain. From this temporal response function, the damping rate was extracted by Webster (2016) with specialised profiles.

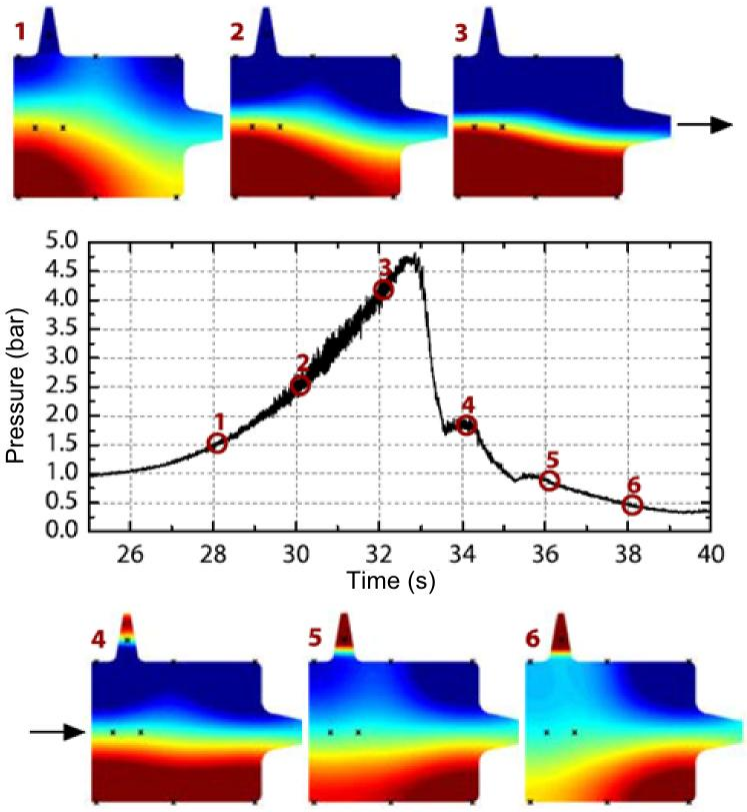

Figure 5: Acoustic excitation with the secondary nozzle being linearly ramped through the BKH first transverse (1T) mode, such that the frequency response of the mode is mapped in the time domain. From this response the damping rate was extracted by Webster (2016) with specialised profiles. The colour plots numbered 1 to 6 show pressure distributions of the 1T mode at different points in time during the linear ramp of the nozzle wheel speed through the 1T modal frequency (Webster S. L., 2016).

The two measurement methods used by Webster (2016) provided consistent measurements of the damping rate. The damping was found to vary significantly with only one parameter, the velocity ratio (VR) of the hydrogen to oxygen injection speeds. Damping rates were found to change particularly at low VR, but the underlying cause of this effect has not yet been explained (Webster S. L., 2016). These damping rates measured by Webster (2016) can be compared against the linear growth (or negative damping) rates obtained with the signal processing methods investigated in this work. Similarly, a study of turbulent jet noise at different operating conditions by Webster et al. (2015) serves as a comparison for the noise intensities obtained in this work.

2.3 BKD

BKD (German: *Brennkammer D* or 'Combustion chamber D') is a DLR combustor that exhibits naturally occurring HF instability characterised by its first tangential (1T) mode (the cylindrical equivalent of the BKH first transverse mode). Unlike BKH, BKD instabilities are self-excited and spontaneous. BKD is also more representative of real rocket engines as it can operate at higher pressures than BKH, is cylindrical, and does not feature secondary hydrogen injection but three concentric rings of primary elements. Figure 6 shows a sketch of the configuration of BKD, which has a chamber diameter of 80 mm. The top left image in Figure 6 shows the main components of BKD namely; an injector head, a combustion chamber and an HF measurement ring fitted with sensors. The injector head has 42 shear coaxial injection elements arranged concentrically as shown at the bottom left of Figure 6. This chamber can be operated up to 80 bar.

The measurement ring at the top right of Figure 6 measures high frequency pressure oscillations using 8 dynamic pressure sensors arranged axisymmetrically. Static pressure sensors and optical probes for OH*imaging are also housed by the ring. The sensors are positioned near the injection plane of the chamber in order to protect them from excessively high temperatures further downstream. Thus, the observability of instability mechanisms in BKD is limited to the injection plane. Current investigations at the DLR are focused on analysing dynamic pressure and OH*imaging signals from probes, while recent experimental runs have incorporated a window access for better visualisation of flame dynamics.

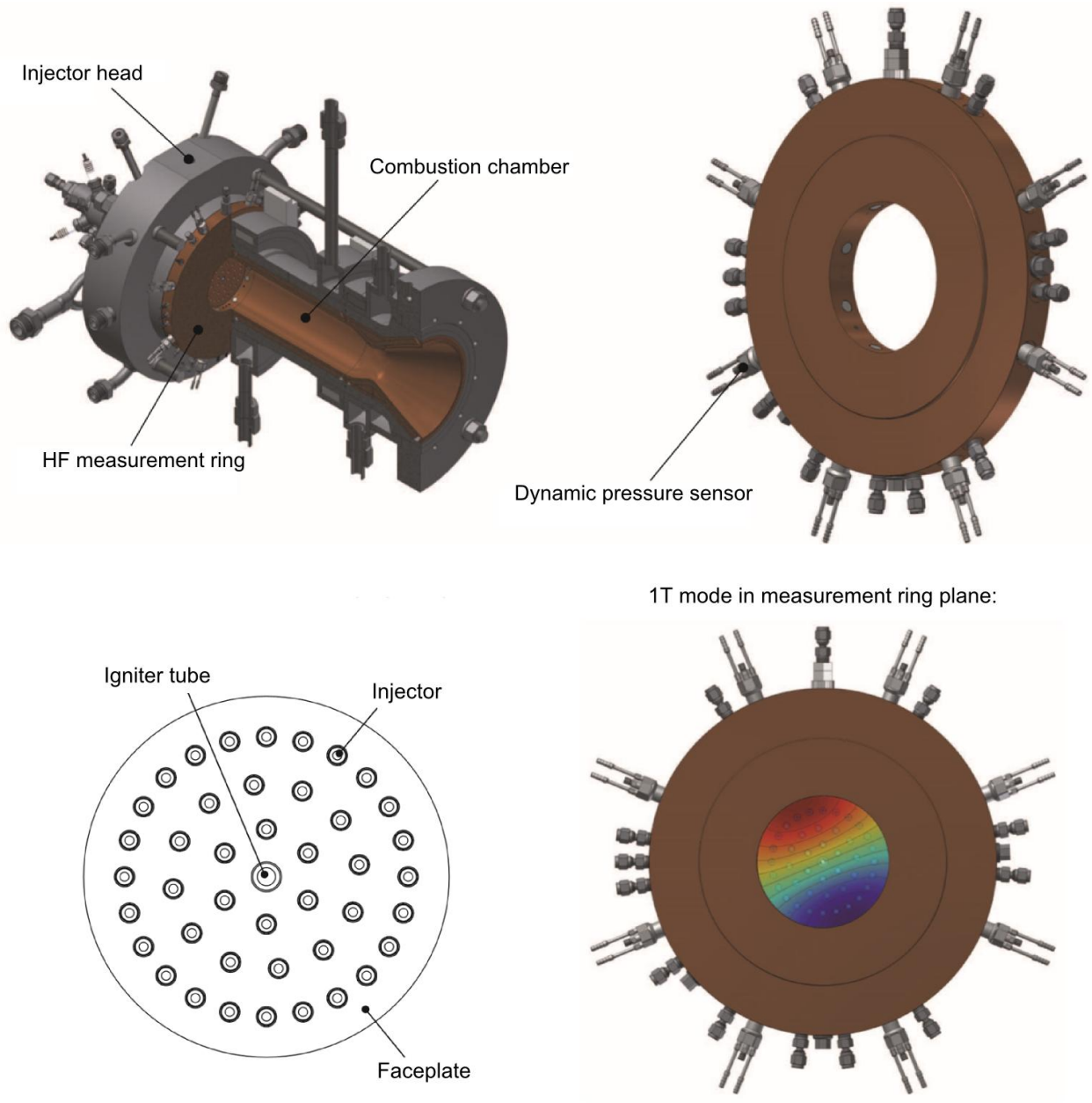

Figure 6: Sketch of the BKD combustor, its faceplate configuration, its measurement ring and the instability-prone first tangential (1T) mode (Groning et al., 2013).

2.4 Parameter Extraction Methods

This section discusses methods used to extract key parameters governing thermo-acoustic behaviour from dynamic pressure measurements, and their associated dynamical models. The current state of the art for parameter extraction in unforced rocket combustors (with no external acoustic excitation) is limited to obtaining the damping rate of a stable acoustic mode by fitting a Lorentzian function to the power spectral density (PSD) of acoustic pressure. This function is given by Eq. (4) in section 2.4.1, and has recently been used by Schulze (2016) to find damping rates of stable BKD load points. The use of the Lorentzian function to find the damping rate of a linear acoustic system is well established (Noiray & Denisov, 2016). However, the function is limited to linear (stable) conditions. Since the growth of an instability cannot be directly observed by wall

sensors, there is no existing method in rocket engine literature to find an unstable growth rate from pressure signals. There is also no mathematical model for the random effects of turbulence on the pressure of a thermo-acoustic mode in a rocket combustor, nor a model for the non-linear dynamics of an unstable rotational mode in a cylindrical rocket combustor. Models for such dynamics in gas turbines have been developed by Noiray and Schuermans (IJNLM 2013) and Noiray and Schuermans (PRSA 2013), with the goal of extracting model parameters from dynamic pressure data using stochastic signal processing techniques.

The stochastic signal processing techniques of Noiray and Schuermans (IJNLM 2013) have been successfully applied to extract system-defining parameters from experimental data of a small-scale, unstable combustor representative of gas turbine conditions (Noiray & Denisov, 2016). This work tests their applicability to rocket engine conditions using BKH and BKD experimental data. The main motivation for the development of these methods is that the linear growth rate of thermo-acoustic instability in a practical combustor, such as a gas turbine or rocket engine, is not directly obtainable from measurable pressure signals. This is due to a timescale difference between localised thermo-acoustic growth and the acoustic response of chamber modes (Noiray & Schuermans, IJNLM 2013). Finding the growth rate of an instability from measurable data is useful for the efficient design of dampers, and for the validation of linear thermo-acoustic models.

This section will discuss four growth rate extraction methods used for gas turbines described by Noiray and Schuermans (IJNLM 2013). Two alternative methods for linear conditions (addressed by the first of the four aforementioned methods) introduced by Noiray (2017) are described as well. Additionally, a chemiluminescence method to isolate the contribution of damping from thermo-acoustic driving in linear conditions is discussed; although its implementation is beyond the scope of this work. The fourth method described by Noiray and Schuermans (IJNLM 2013), which is the focus of this work, is the most complex and most broadly applicable. This method is based on a Fokker-Planck formulation of the acoustic dynamics and has different formulations for standing and rotational mode behaviour. For the latter case, a formulation is provided by Noiray and Schuermans (PRSA 2013) for azimuthal modes in annular combustion chambers. This formulation and its associated dynamical models are discussed at the end of this section.

2.4.1 Method 1: Power spectral density of acoustic pressure

This method uses a linear harmonic oscillator model to determine the net damping rate (negative growth rate) of a stable acoustic mode in a combustor. The dynamics of a stable acoustic mode can be described by Eq. (1) (Noiray & Schuermans, IJNLM 2013):

$$\frac{d^2p'}{dt^2} - 2\nu\frac{dp'}{dt} + \omega_0{}^2 p' = \xi \qquad (1)$$

where p' is the acoustic pressure, ν is the linear growth rate, ω_0 is the natural frequency of the mode, and ξ is turbulence-induced heat release of a stochastic (random) nature.

The growth rate ν can be decomposed into separate components representing thermo-acoustic driving and damping in Eq. (2):

$$\nu = \beta - \alpha \quad (2)$$

where β is the thermo-acoustic driving rate and α is the damping rate. It is noted that this formulation of a growth rate consisting of deterministic driving and damping contributions is stated by Culick and Yang (1995) as part of a harmonic oscillator model for the acoustic pressure in a rocket combustor. However, the stochastic effect of turbulence on a thermo-acoustic mode is not formulated by Culick and Yang (1995), nor by other existing rocket engine literature to the knowledge of the author.

The stochastic heat release ξ in a combustion chamber is induced by turbulent combustion noise (Noiray & Schuermans, IJNLM 2013). The frequency spectrum of ξ, which is the 'force' driving acoustic pressure in Eq. (1), follows a smooth decay due to its origin in turbulent combustion noise (Noiray & Schuermans, IJNLM 2013). For the narrow frequency band of interest around a modal peak, ξ can be approximated as Gaussian white noise. Such noise has equal power at all frequencies. This simplification of ξ means that the specific spectral decay of ξ is unimportant. Smooth spectral decay around a modal frequency can be accurately represented by an equivalent white noise intensity provided that the band-pass filtering is not excessively broad (Bonciolini et al., 2017). Hence, this theory from gas turbine literature can be similarly applied to rocket engines by assuming Gaussian white noise driving.

The PSD of a linear mode excited by ξ is given by Eq. (3) (Noiray & Schuermans, IJNLM 2013):

$$S_{p'p'}(\omega) = \frac{1}{2\pi}\frac{\Gamma}{({\omega_o}^2 - \omega^2)^2 + 4\nu^2\omega^2} \quad (3)$$

where $S_{p'p'}(\omega)$ is the two-sided PSD of p', ω is the frequency and Γ is the noise intensity of ξ (equal to its PSD height: a detailed explanation of the noise intensity theory is given in Appendix A). It is noted that the name 'noise intensity' refers to the origin of ξ in turbulent combustion noise, but that ξ is itself a heat release term not an acoustic term.

Eq. (3) can be derived from the analytical expression for a damped driven harmonic oscillator. If $\nu << \omega_o$, the peak frequency of the measured PSD closely approximates ω_o, and Eq. (3) can be simplified to a Lorentzian equation (explanation provided in Appendix A) as in Eq. (4):

$$S_{p'p'}(\omega) = M\frac{\nu^2}{(\omega_o - \omega)^2 + \nu^2} \quad (4)$$

where M is the maximum of $S_{p'p'}(\omega)$.

If the LHS of Eq. (3) is equated to $M/2$, it can also be shown that ν equals $\omega_o - \omega$. Thus the half-width-half-maximum (HWHM) of the PSD of acoustic pressure gives the net damping rate (negative growth rate) for linear stability.

2.4.2 Method 1 alternatives: Power spectral densities of amplitude envelope and its fluctuation

There exist two alternative methods for extracting the growth rate from linear conditions (Noiray N. , 2017). The first relates the PSD of amplitude envelope fluctuation to the noise intensity and the growth rate as given by Eq. (5):

$$S_{A'A'}(\omega) = \frac{1}{2\pi}\frac{1}{\omega^2 + 4\nu^2}\left(\frac{\Gamma}{2{\omega_0}^2}\right) \tag{5}$$

where the $S_{A'A'}(\omega)$ is the two-sided PSD of amplitude envelope fluctuation A'.

The second alternative method is a simple way of obtaining the growth rate from the cut off frequency of the PSD of the amplitude envelope A. This is given by Eq. (6):

$$\omega_{S_{AA(\omega)},\text{cut-off}} = 2\,\text{abs}(\nu) \tag{6}$$

where the $S_{AA}(\omega)$ is the two-sided PSD of amplitude envelope A.

These two alternative methods serve to verify the results obtained with method 1.

2.4.3 Method 1 complement: Chemiluminescence method to isolate damping rate

The methods described in the previous sub-sections allow the extraction of the growth rate ν, but not of its individual contributions β and α. Recent work by Boujo et al. (2016) has analysed flame chemiluminescence imaging from a methane-air combustor to extract the damping rate based on the same theoretical formulations discussed in section 2.4.1. The damping rate appears as an isolated variable in Eq. (7):

$$\frac{d^2p'}{dt^2} + 2\alpha\frac{dp'}{dt} + {\omega_0}^2 p' = \gamma\dot{q}(t) \tag{7}$$

where $\gamma\dot{q}(t)$ is a forcing term associated with heat release fluctuations of the flame, and $\dot{q}(t)$ is the sum of random heat release fluctuations driven by turbulence and of deterministic heat release fluctuations driven by thermo-acoustic coupling. This equation is equivalent to Eq. (1) in section 2.4.1, where the effect of the deterministic heat release fluctuations is represented by β on the LHS and the effect of random heat release fluctuations is represented by ξ on the RHS.

Based on Eq. (7), the flame transfer function in the complex frequency domain is given by Eq. (8):

$$H(s) = \frac{p(s)}{q(s)} = \frac{\gamma s}{(s-\lambda)(s-\lambda_*)} \tag{8}$$

where the pole is $\lambda = -\alpha + i\omega_o$. The damping rate α can thus be extracted by fitting Eq. (8) to an experimentally obtained flame transfer function. For LOx/H_2 propellants an estimate for the heat release can be obtained from OH* chemiluminescence data, by assuming a linear relationship between the measured light intensity and the heat release rate. The method's precision is limited by the validity of this heat release estimation, and thus requires investigation beyond the scope of this work.

2.4.4 Method 2: Power spectral density of amplitude envelope

When linear instability (that is $\beta > \alpha$) occurs, the amplitude envelope of the acoustic pressure grows exponentially at a rate of ν (that is, $\propto e^{\nu t}$ where ν is in rad/s) until restrained by non-linear damping to a limit cycle. The amplitude envelope of this limit cycle, obtained by applying the Hilbert transform to p', is not constant but randomly perturbed by the stochastic heat release ξ. By assuming a physical model for these dynamics, and matching it to the observed envelope, the growth rate ν and other parameters can be extracted.

A van der Pol oscillator described by Eq. (9) is assumed (Noiray & Schuermans, IJNLM 2013):

$$\frac{d^2p'}{dt^2} - (2\nu - \kappa p'^2)\frac{dp'}{dt} + \omega_0{}^2 p' = \xi \qquad (9)$$

where κ is the non-linearity coefficient. The non-linearity coefficient κ is related to the constant, unperturbed limit cycle amplitude that the system reaches if ξ is negligible. This occurs if the stochastic heat release is small compared to deterministic heat release oscillations that arise from thermo-acoustic coupling in a mode; that is, associated with β. This deterministic amplitude of the limit cycle A_0 is given by Eq. (10):

$$A_0 = \left(\frac{8\nu}{\kappa}\right)^{1/2} \qquad (10)$$

Theoretical manipulations of Eq. (10) by Noiray and Schuermans (IJNLM 2013) provide a differential equation for the amplitude envelope of the limit cycle given by Eq. (11):

$$\frac{dA}{dt} = A\left(\nu - \frac{\kappa}{8}A^2\right) + \frac{\Gamma}{4\omega_0{}^2 A} + \xi \qquad (11)$$

where A is the amplitude envelope.

If the van der Pol dynamics of Eq. (11) are assumed, three methods can be derived to extract the unstable growth rate, noise intensity and non-linearity coefficient from the amplitude envelope of a limit cycle. These are henceforth referred to as methods 2, 3 and 4.

Method 2 assumes linear fluctuations of A about its mean, and consists of fitting an analytical function to the PSD of these fluctuations given by Eq. (12) (Noiray & Schuermans, IJNLM 2013):

$$S_{A'A'}(\omega) = \frac{\bar{A}^2\, c_0/\pi}{\omega^2 + (2\nu + c_0)^2} \qquad (12)$$

where $S_{A'A'}(\omega)$ is the two-sided PSD of the amplitude envelope fluctuation A', $\bar{A}$ is the mean of the amplitude envelope, and c_0 is a noise intensity coefficient. The noise intensity coefficient c_0 is given by Eq. (13):

$$c_0 = \frac{\Gamma}{4\omega_0{}^2 A_0{}^2} \qquad (13)$$

Eq. (12) can be fitted to experimental data to extract ν and c_0 if the limit cycle amplitude is linearly perturbed, that is if $A' << \bar{A} \approx A_0$.

2.4.5 Method 3: Fokker-Planck stationary probability density function

Method 3 employs the Fokker-Planck equation; a formulation that can describe the statistics of the stochastic differential equation Eq. (11). For the assumed van der Pol dynamics, there is an analytical solution to the probability density function (PDF) of the amplitude envelope which can be used to extract parameters. This is given by Eq. (14) (Noiray & Schuermans, IJNLM 2013):

$$\mathrm{P(A)} = \frac{\sqrt{\frac{4\nu}{\pi c_0}}}{{A_0}^2 \mathrm{erfc}\left(-\sqrt{\frac{\nu}{4c_0}}\right)} \mathrm{A} \exp\left(-\frac{\nu}{c_0}\left(\frac{A^2 - {A_0}^2}{2{A_0}^2}\right)^2\right) \tag{14}$$

where $\mathrm{P(A)}$ is the PDF of the amplitude envelope A.

Method 3 consists of fitting Eq. (14) to the PDF of the experimental A to extract the ratio $\frac{\nu}{c_0}$, where ν may be negative or positive (applies to both stable and unstable cases). To isolate ν, c_0 can be found independently from the autocorrelation of the acoustic pressure time signal. It is equal to the exponential decay rate of this autocorrelation (Noiray & Schuermans, IJNLM 2013). Method 3 is not restricted to linear fluctuations of A but assumes a stationary PDF. That is, it assumes that the PDF of A is time invariant, which is the case for an established limit cycle.

It is noted that the original expression underlying Eq. (14) is Eq. (15) (Noiray N. , 2017):

$$\mathrm{P(A)} = \frac{1}{N} \exp\left(-\frac{4{\omega_0}^2}{\Gamma}\left(-\frac{\nu}{2}A^2 + \frac{\kappa}{32}A^4 - \frac{\Gamma}{4{\omega_0}^2}\ln(A)\right)\right) \tag{15}$$

where N is a normalisation constant such that $\mathrm{P(A)}$ is a PDF.

2.4.6 Method 4: Fokker-Planck coefficients method

Method 4 is the most general of the four methods and can be applied to both unstable and stable cases. The Fokker-Planck equation describes the time evolution of the PDF of A or $\mathrm{P(A,t)}$ in Eq. (16) (Noiray & Schuermans, IJNLM 2013):

$$\frac{\partial}{\partial t}\mathrm{P(A,t)} = -\frac{\partial}{\partial A}\left(\mathcal{F}(A)\mathrm{P(A,t)}\right) + \frac{\Gamma}{4{\omega_0}^2}\frac{\partial^2}{\partial A^2}\mathrm{P(A,t)} \tag{16}$$

where $\mathcal{F}(\mathrm{A})$ and $\frac{\Gamma}{4{\omega_0}^2}$ are the drift and diffusion coefficients respectively, named after the analogous application of the Fokker-Planck equation to Brownian motion.

The drift coefficient $\mathcal{F}(\mathrm{A})$ can be equated to the assumed dynamics of A. For an unstable case $\mathcal{F}(\mathrm{A})$ is given by the van der Pol dynamics of Eq. (11) as written in Eq. (17) (Noiray & Schuermans, IJNLM 2013):

$$\mathcal{F}(\mathrm{A}) = \mathrm{A}\left(\nu - \frac{\kappa}{8}A^2\right) + \frac{\Gamma}{4{\omega_0}^2 \mathrm{A}} \tag{17}$$

For a stable case, Eq. (17) can be used with $\kappa = 0$ to consider only linear dynamics.

The drift and diffusion coefficients can be computed from the first and second transition moments of the experimental amplitude envelope as written in Eq. (18) and Eq. (19) (Noiray & Schuermans, IJNLM 2013):

$$\mathcal{F}(A) = \lim_{\tau \to 0} D_{\tau}^{(1)} = \lim_{\tau \to 0} \frac{1}{\tau} \int_{0}^{\infty} (a - A)\, P\left(a, t + \tau \,\middle|\, A, t\right) da \qquad (18)$$

where $D_{\tau}^{(1)}$ is the first transition moment, and $P\left(a, t + \tau \,\middle|\, A, t\right)$ is the probability density function of amplitude a at time $t + \tau$ given an amplitude of A at time t. This conditional probability density function is defined by the ratio of the joint PDF to the total PDF such that $\int P\left(a \,\middle|\, A\right) da = \frac{\int\int P(a\, U\, A)\, da\, dA}{\int P(A)\, dA} = \frac{1}{1} = 1.$

$$\frac{\Gamma}{4{\omega_0}^2} = \lim_{\tau \to 0} D_{\tau}^{(2)} = \lim_{\tau \to 0} \frac{1}{2\tau} \int_{0}^{\infty} (a - A)^2\, P\left(a, t + \tau \,\middle|\, A, t\right)\, da \qquad (19)$$

where $D_{\tau}^{(2)}$ is the second transition moment.

These coefficients are computed by first considering the range of A from A_{min} to A_{max} for the entire time series, and defining intermediate amplitudes $a = A_{min} - \Delta A/2 + n\Delta A$ where n is an integer from 1 to $(A_{max} - A_{min})/\Delta A$ and ΔA is a change that defines the bin width of a and the number of bins n. For a given A value (defined by the same bin width ΔA), the points with this value for the experimental time series are identified and counted. For the identified points, a time shift of τ is applied. From these time-shifted positions in the time series, counts can be made for the range of a values using defined bins $a \pm \Delta A/2$, such that $P\left(a, t + \tau \,\middle|\, A, t\right)$ is calculated with a resolution of n bins. This is done for a range of τ such that the time shift limit to zero can be approximated. Calculating the limit to zero can require a considered extrapolation based on signal behaviour, however there is no universal extrapolation method[1]. This entire procedure is repeated for a range of A such that plots of coefficient computations versus A are generated. From such plots, parameters of interest such as ν, κ and Γ may be extracted as demonstrated in section 2.4.7.

A significant advantage of this fourth method is its general applicability. There are no dynamical assumptions behind the transition moment computations for the Fokker-Planck coefficients (Noiray & Schuermans, IJNLM 2013). By comparing the assumed dynamics to the computed coefficients, an indication can be obtained of the accuracy of the van der Pol oscillator model.

The main disadvantage of the Fokker-Planck coefficients method is its susceptibility to a broad set of signal processing effects generally referred to as 'finite time effects' (Boujo & Noiray, 2017). These cause deviations in the computed transition moments from their theoretical limits to zero at small values of τ. This is depicted in Figure 7 for a synthetic acoustic mode with three different band-pass widths. Band-pass filtering gives rise to a type of finite time effect. Increasing the band-pass width around the resonance frequency includes faster (or higher frequency) changes from

[1]Private communication with Prof N. Noiray

the resonance sinusoid in the modal time series. These fast changes must be increasingly included to obtain a meaningful transition moment for a decreasing τ as shown in Figure 7.

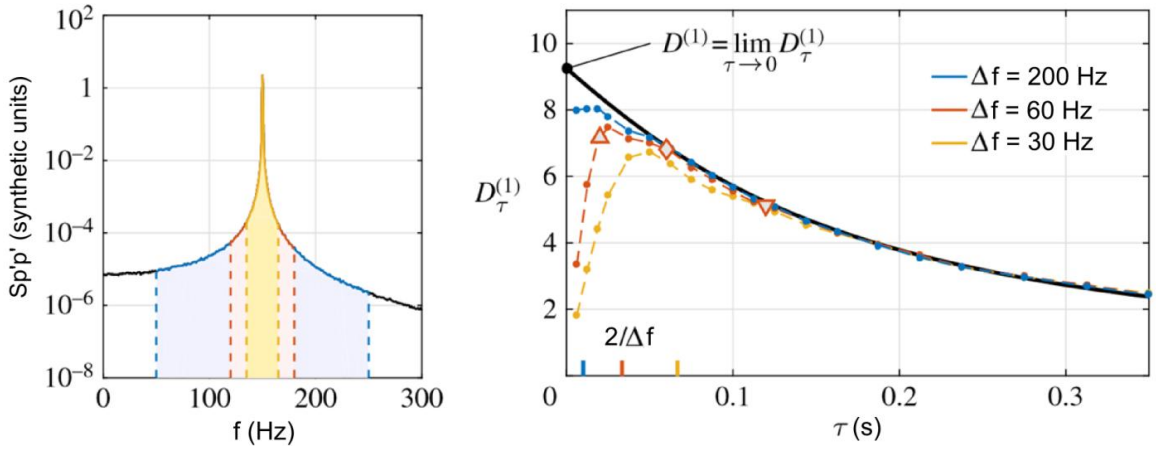

Figure 7: Signal collapses at low τ due to finite time effects for the first transition moment $D^{(1)}_\tau$ with different band-pass filters around a synthetic acoustic mode generated with Simulink. The black line shows an exponential extrapolation to obtain the correct limit to zero. Three symbols are plotted at τ = 0.02, 0.06 and 0.12 s for the 60 Hz band-pass filter. This signal begins to deviate from the black line between 0.02 and 0.06 s which, in this case, corresponds approximately to 2 divided by the band-pass filter width (Δf). Similar occurrences can be observed for the two other band-pass filters around their respective 2/Δf values (Boujo & Noiray, 2017).

A method to compute the Fokker-Planck drift and diffusion coefficients directly without requiring an extrapolation to account for finite time effects has been recently devised by Boujo and Noiray (2017). However, this new method has only been tested with synthetic signals. The effect of measurement noise on the robustness of the method is unknown (Boujo & Noiray, 2017). While an investigation of finite time effects and of the possible applicability of this method to rocket engines is beyond this project's scope, these are important directions for future work.

It is also noted that the theory presented in this sub-section is applicable to a standing acoustic mode such as a BKH mode. Tangential modes in cylindrical chambers, such as the 1T mode in BKD, have rotational behaviour. A dynamic model for such a situation was developed by Noiray and Schuermans (PRSA 2013). Expressions for Fokker-Planck coefficients were derived in this work and can be applied to the rotational 1T mode in BKD. These expressions are provided in section 2.4.8.

2.4.7 Method 4: Validation with unstable combustor experiment using active control

A premixed methane (CH_4) and air combustor with a naturally unstable longitudinal mode was used by Noiray and Denisov (2016) to observe instability growth directly with active control. The set-up used is shown in Figure 8.

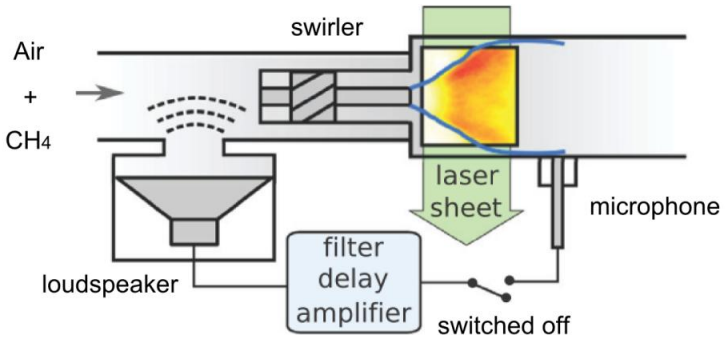

Figure 8: Cylindrical air and methane combustor with a premixing swirler featuring active control (Noiray & Denisov, 2016).

Three different operating points named c_1, c_2 and c_3 were studied with this combustor, which operates at atmospheric pressure and is representative of gas turbine conditions. The rms of acoustic pressure of these points is shown on the left of Figure 9 versus the equivalence ratio, while the spectral content and the PDF of acoustic pressure are shown on the right of Figure 9.

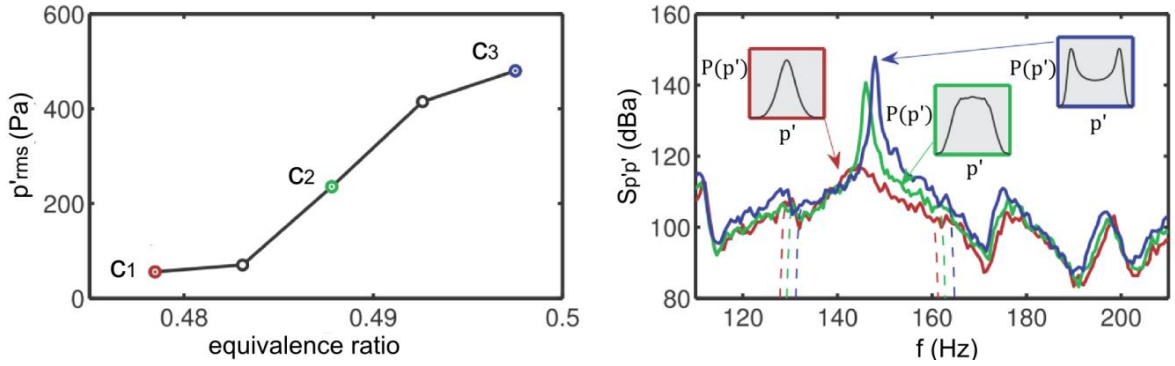

Figure 9: Three operating points c_1, c_2 and c_3 studied; on the left is the rms of acoustic pressure versus equivalence ratio, and on the right is the spectral content and the PDF of acoustic pressure. Instability is caused by coupling between the flame and a longitudinal mode of the chamber at high equivalence ratios (Noiray & Denisov, 2016).

Points c_1, c_2 and c_3 were classified by Noiray and Denisov (2016) as stable, semi-unstable and unstable, respectively. An indicator of instability is the acoustic pressure PDF as plotted on the right of Figure 9. For the stable c_1 case a uni-modal distribution with a sharp peak is observed, for the semi-unstable c_2 case a broadening of this profile occurs and its peak flattens, while for the unstable c_3 case two distinct peaks are present which renders a bimodal distribution. Noiray and Denisov (2016) applied methods 3 and 4 to both c_2 and c_3 to find their unstable growth rates.

Validation of van der Pol dynamics and of the Fokker-Planck approach by applying methods 3 and 4 to c_2 and c_3 are the principal results of the study. Noiray and Denisov (2016) obtained growth rates of $\nu = 0.5$ rad/s and $\nu = 10$ rad/s for c_2 and c_3 by applying method 4. For each case, this consisted of first finding the diffusion coefficient using Eq. (19) to obtain the noise intensity Γ. The convection coefficient $\mathcal{F}(A)$, given by Eq. (18), is then computed for a range of A and the van der Pol expression in Eq. (17) is fitted onto these results to extract the growth rate. Since Γ in Eq. (17) is known, the fit is only dependent on ν and κ. Physically, these represent a growing linear function of A and a decaying cubic of A, respectively, as illustrated in the middle row of Figure 10. For this known combination of ν and κ, a best fit can be obtained that determines their values.

To check method 4 results, Noiray and Denisov (2016) fed the obtained ν, κ and Γ into the expression for the stationary PDF of A in method 3 and obtained a close fit to the measured PDF in both cases. Hence, the application of methods 4 and 3 to the data provided a clear indication that the assumed van der Pol dynamics are correct. These findings are shown in Figure 10.

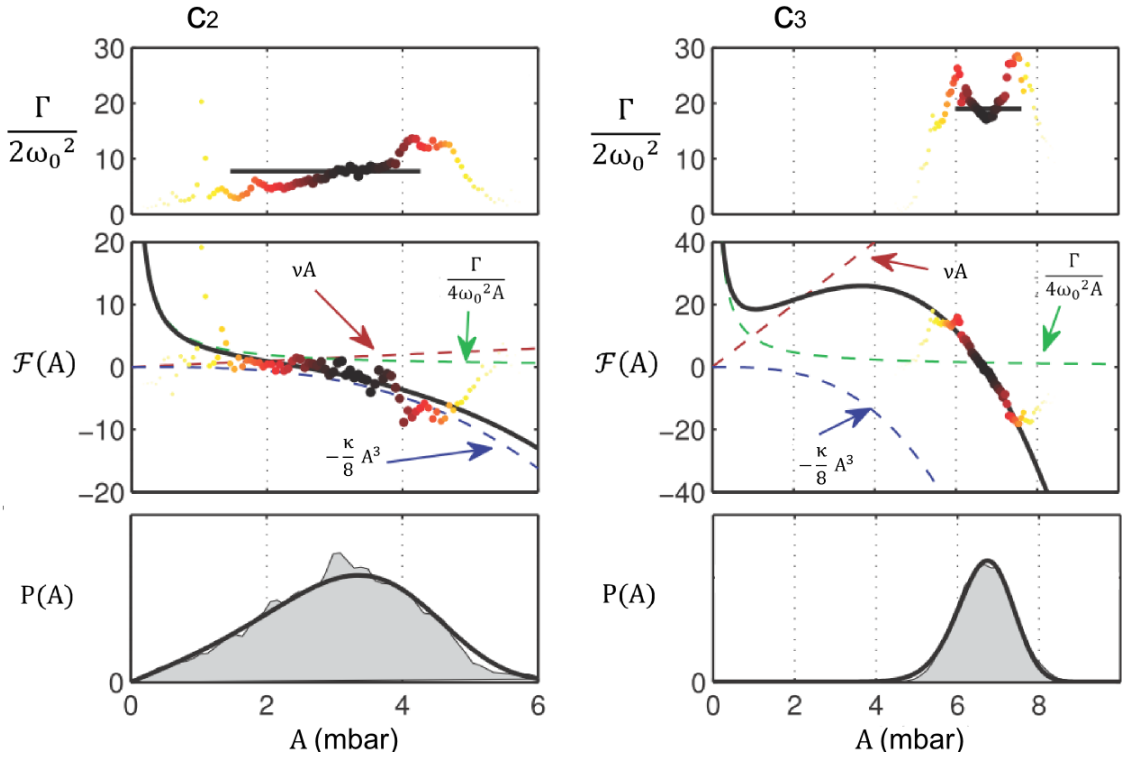

Figure 10: Top: best fits (black lines) for the diffusion (in this case twice its value $2 \times \Gamma/(4\omega_0{}^2)$) and drift coefficients for c_2 and c_3. Experimental coefficient values are shown in coloured dots indicating the occurrence intensity of the specific amplitude A. Bottom: plotted PDFs of the acoustic amplitude envelope (black lines) for c_2 and c_3 based on the Fokker-Planck stationary PDF analytical expression using parameters extracted from the coefficient fits. Experimental PDFs of A are shown in grey; a precise agreement can be observed with the analytical solution for the stationary PDF (Noiray & Denisov, 2016).

An important result of this study is a direct validation of the extracted parameters by observing the growth of c_2 and c_3. The active control system allows stabilisation of c_2 and c_3 to linear levels which can then be released to observe instability, as shown in Figure 11.

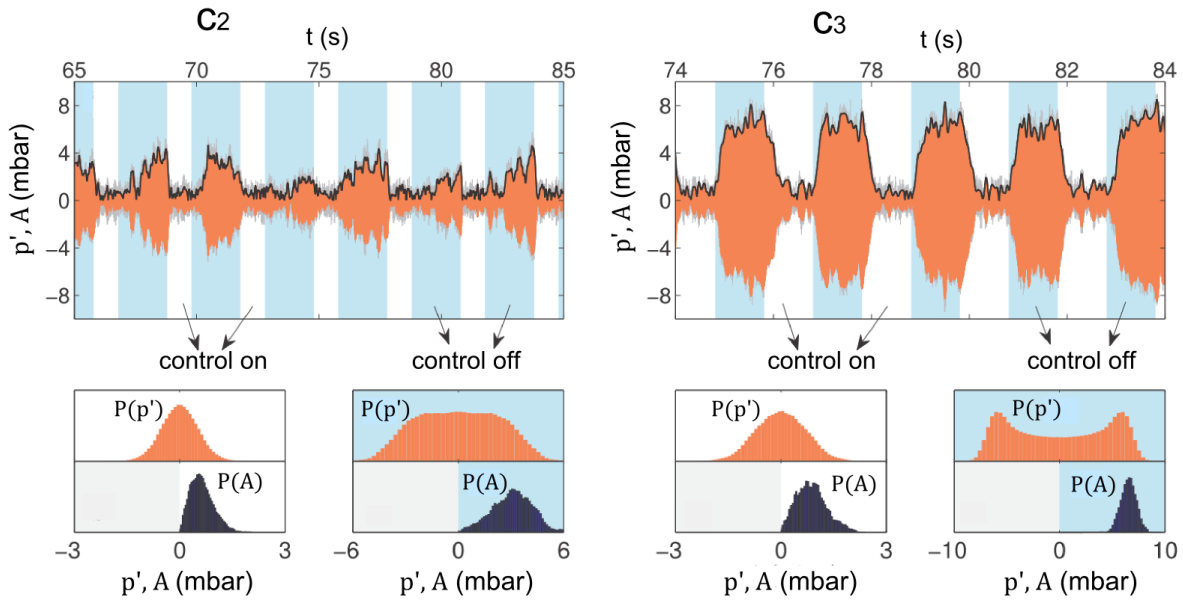

Figure 11: Acoustic levels of c_2 and c_3 with periodic switching on/off of the active control, and corresponding PDFs of acoustic pressure and amplitude envelope (Noiray & Denisov, 2016).

The uni-modal acoustic pressure PDF with control on, shown in Figure 11, identifies the reduction of acoustic pressure to linear levels. This active control of acoustics, after being applied for a length of time, can be switched off to observe the instability growth directly (Noiray & Denisov, 2016). The evolution of the PDF of A ($P(A)$) with time during the transient growth stages of c_2 and c_3 was compared to the simulated PDF of A using the Fokker-Planck equation with the extracted parameters. These are shown in Figure 12, where the depicted experimental PDFs are constructed by counting A values measured over 100 iterations of the same control on/off experiment.

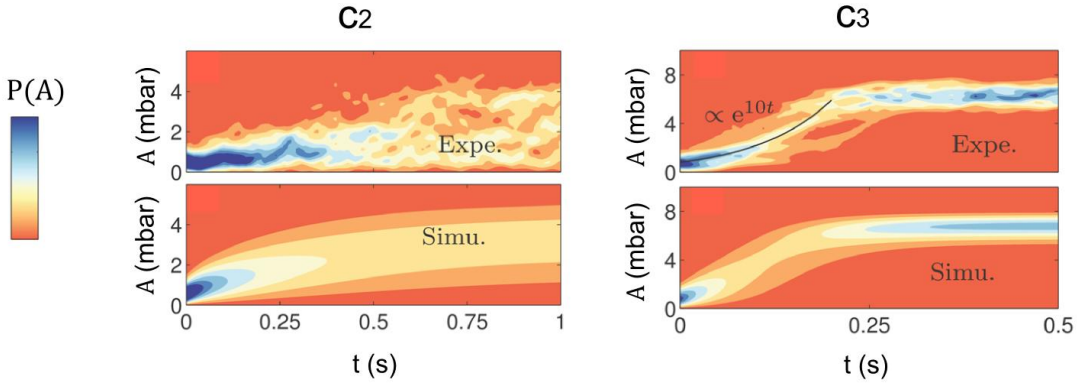

Figure 12: Time evolution of PDF of A for c_2 and c_3 where t=0 is the time when control is switched off. A good fit is obtained for the clearly unstable case c_3, with a growth rate of 10 rad/s matching the observed exponential growth (Noiray & Denisov, 2016).

For the clearly unstable case c_3, it can be seen from Figure 12 that the PDF of A is well captured during the growth period of 0.25 seconds until it reaches a stationary state. This directly validates the use of the Fokker-Planck equation and van der Pol dynamics to describe instability in the combustor.

2.4.8 Method 4: Formulation for cylindrical chamber with rotational mode behaviour

In a cylindrical combustion chamber such as BKD, or other rocket combustors, acoustic modes can exhibit rotational behaviour. At any point in time, a transverse chamber mode, such as the BKD 1T mode, can be theoretically represented by the superposition of two standing modes. These theoretical standing modes, with modal amplitudes A and B, are spatially oriented at 90° to each other and are temporally related by an instantaneous phase difference ϕ. A purely standing mode would consist of only one component (i.e. either $A = 0$ or $B = 0$), while a purely rotating mode would consist of equal amplitudes with a constant phase shift of $\pm\frac{\pi}{2}$ (i.e. $A = B$ and $\phi = \pm\frac{\pi}{2}$). In reality, modes in cylindrical combustors can switch stochastically between standing and rotating behaviour such that A, B and ϕ constantly change. A dynamical model for the thermo-acoustic behaviour of such modes was developed by Noiray and Schuermans (PRSA 2013) to derive appropriate Fokker-Planck coefficient formulations. These are described in this sub-section together with a modal reconstruction method which decomposes transverse modes into two standing modes.

The acoustic pressure of azimuthal modes at the wall perimeter of an annular gas turbine chamber can be expressed as the sum of two orthogonal standing modes as in Eq. (20) (Noiray & Schuermans, PRSA 2013):

$$p'(\theta,t) = p'_a(t)\cos(n\theta) + p'_b(t)\sin(n\theta) \tag{20}$$

where n is the modal index, θ is the angular position along the wall perimeter, p'_a is the A mode temporal acoustic pressure and p'_b is the B mode temporal acoustic pressure.

The temporal acoustic pressures for the A and B modes are given by Eq. (21) and Eq. (22):

$$p'_a(t) = A(t)\cos(\omega_o t + \varphi_a(t)) \tag{21}$$
$$p'_b(t) = B(t)\cos(\omega_o t + \varphi_b(t)) \tag{22}$$

where $A(t)$ and $B(t)$ are the amplitude envelopes of the A and B modes which are perturbed by stochastic forcing.

The phase difference between the A and B modes is given by Eq. (23):

$$\phi = \varphi_a(t) - \varphi_b(t) \tag{23}$$

where ϕ is the phase difference.

The decomposition of the experimental $p'(\theta,t)$ signal into its $p'_a(t)$ and $p'_b(t)$ components can be achieved with the reconstruction approximations given by Eq. (24) and Eq. (25) (Noiray & Schuermans, PRSA 2013):

$$p'_a(t) = \frac{1}{\pi}\int_{-\pi}^{+\pi} p'(\theta,t)\cos(n\theta)\,d\theta \approx \frac{2}{K}\sum_{k=1}^{K} p'(\theta_K,t)\cos(n\theta_K) \tag{24}$$

$$p'_b(t) = \frac{1}{\pi}\int_{-\pi}^{+\pi} p'(\theta,t)\sin(n\theta)\,d\theta \approx \frac{2}{K}\sum_{k=1}^{K} p'(\theta_K,t)\sin(n\theta_K) \tag{25}$$

where K is the index for sensor positions at specific θ values.

While these modal equations were derived for azimuthal modes in annular gas turbine combustion chambers, they are equally applicable for the tangential modes present in rocket combustors since the acoustic pressure distribution at the chamber wall perimeter are the same.

The thermo-acoustic dynamics of the A and B modes are given by the coupled equations Eq. (26) and Eq. (27) (Noiray & Schuermans, PRSA 2013):

$$\frac{d^2p'_a}{dt^2} + {\omega_0}^2 p'_a = (\beta - \alpha)\frac{dp'_a}{dt} - \frac{3\kappa_a\left(\frac{dp'_a}{dt}\left(3{p'_a}^2 + {p'_b}^2\right) + 2\frac{dp'_b}{dt}p'_a p'_b\right)}{4} + \xi_a \quad (26)$$

$$\frac{d^2p'_b}{dt^2} + {\omega_0}^2 p'_b = (\beta - \alpha)\frac{dp'_b}{dt} - \frac{3\kappa_b\left(\frac{dp'_b}{dt}\left(3{p'_b}^2 + {p'_a}^2\right) + 2\frac{dp'_a}{dt}p'_a p'_b\right)}{4} + \xi_b \quad (27)$$

From the dynamics in Eq. (26) and Eq. (27), relations for the amplitude envelopes and phase difference of the A and B modes can be obtained as written in Eq. (28), Eq. (29) and Eq. (30):

$$\frac{dA}{dt} = \nu_a A - \frac{3\kappa_a}{32}(3A^2 + (2 + \cos(2\phi))B^2)A + \frac{\Gamma_a}{4{\omega_0}^2 A} + \xi_a \quad (28)$$

$$\frac{dB}{dt} = \nu_b B - \frac{3\kappa_b}{32}(3B^2 + (2 + \cos(2\phi))A^2)B + \frac{\Gamma_b}{4{\omega_0}^2 B} + \xi_b \quad (29)$$

$$\frac{d\phi}{dt} = \frac{3\kappa}{32}(A^2 + B^2)\sin(2\phi) + \left(\frac{1}{A} + \frac{1}{B}\right)\xi_\phi \quad (30)$$

where ξ_a, ξ_b and ξ_ϕ are uncorrelated white noises.

From Eq. (28) and Eq. (29) analytical expressions can be obtained for the Fokker-Planck drift coefficients given by Eq. (31) and Eq. (32) (Noiray & Schuermans, PRSA 2013):

$$\mathcal{F}_A(A, \breve{B}) = \nu_a A - \frac{3\kappa_a}{32}\left(3A^2 + \breve{B}^2\right)A + \frac{\Gamma_a}{4{\omega_0}^2 A} \quad (31)$$

$$\mathcal{F}_B(\breve{A}, B) = \nu_b B - \frac{3\kappa_b}{32}\left(3B^2 + \breve{A}^2\right)B + \frac{\Gamma_b}{4{\omega_0}^2 B} \quad (32)$$

where $\breve{A} = (2 + \cos 2\phi)^{1/2}A$ and $\breve{B} = (2 + \cos 2\phi)^{1/2}B$.

These drift coefficients have a 2D dependency since the dynamics of the A and B modes are non-linearly coupled. They can be equated to the limit to zero of 2D first transition moments as written in Eq. (33) and Eq. (34) (Noiray & Schuermans, PRSA 2013):

$$\mathcal{F}_A(A, \breve{B}) = \lim_{\tau \to 0} \frac{1}{\tau}\iint_0^\infty (a - A)\ P(a, \breve{b}, t + \tau \,|\, A, \breve{B}, t)\ da\ d\breve{b} \quad (33)$$

where $P(a, \breve{b}, t + \tau \,|\, A, \breve{B}, t)$ is the 2D probability density function of a and $\breve{b}$ at time $t + \tau$ given amplitudes A and $\breve{B}$ occurred at time t. This 2D conditional probability density function is defined by $\iint P(a, \breve{b} \,|\, A, \breve{B})\ da\ d\breve{b} = \frac{\int\int\int\int P(a\ U\ \breve{b}\ U\ A\ U\ \breve{B})\ da\ d\breve{b}\ dA\ d\breve{B}}{\int\int P(A\ U\ \breve{B})\ dA\ d\breve{B}} = \frac{1}{1} = 1.$

$$\mathcal{F}_B(\breve{A}, B) = \lim_{\tau \to 0} \frac{1}{\tau}\iint_0^\infty (b - B)\ P(\breve{a}, b, t + \tau \,|\, \breve{A}, B, t)\ d\breve{a}\ db \quad (34)$$

A best fit procedure can be applied to Eq. (33) and Eq. (34) with respect to the computed drift coefficients. From this best fit the parameters of interest ν_a, ν_b, κ_a, κ_b, Γ_a, and Γ_b can be extracted. Such a fit is shown for the first and second azimuthal modes of an unstable gas turbine combustion chamber in Figure 13.

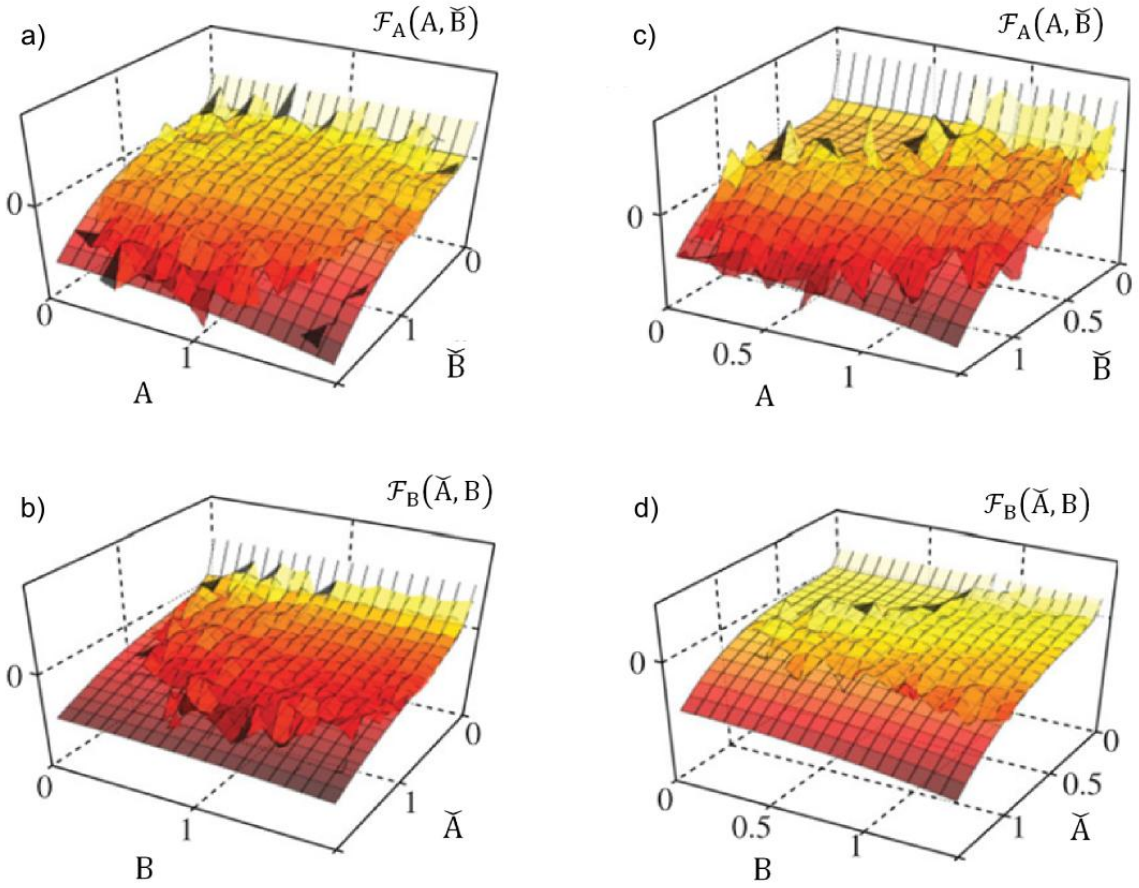

Figure 13: Fitting of theoretical Fokker-Planck drift coefficients onto experimentally computed coefficients for the a) A mode and b) B mode of a first azimuthal mode and the c) A mode and d) B mode of a second azimuthal mode in an unstable gas turbine combustion chamber. The smooth sheet is the theoretical fit while the more uneven contour is the experimental data (Noiray & Schuermans, PRSA 2013).

The noise intensities Γ_a and Γ_b can also be independently found from equating the diffusion coefficients to the limit to zero of 2D second transition moments as in Eq. (35) and Eq. (36):

$$\frac{\Gamma_a}{4{\omega_0}^2} = \lim_{\tau\to 0}\frac{1}{2\tau}\iint_0^\infty (a-A)^2\ P\left(a,\breve{b},t+\tau\,\middle|\,A,\breve{B},t\right)\,da\,d\breve{b} \qquad (35)$$

$$\frac{\Gamma_b}{4{\omega_0}^2} = \lim_{\tau\to 0}\frac{1}{2\tau}\iint_0^\infty (b-B)^2\ P\left(\breve{a},b,t+\tau\,\middle|\,\breve{A},B,t\right)\,d\breve{a}\,db \qquad (36)$$

It is noted that the noise intensities Γ_a and Γ_b , as well as the non-linearity coefficients κ_a and κ_b, are expected to differ from each other only slightly (Noiray & Schuermans, PRSA 2013). Due to the general two-dimensionality of these Fokker-Planck formulations, the parameter extraction equations described in this sub-section can be referred to as the 2D Fokker-Planck coefficients method.

2.4.9 Simplified dynamics for cylindrical chamber with rotational mode behaviour

A more simplified dynamics model for rotational modes than that discussed in the previous sub-section was also developed by Noiray and Schuermans (PRSA 2013). It originates with the assumption of a fixed phase difference at $\pm\frac{\pi}{2}$ (which constitutes a purely rotating mode if $A = B$). To understand this assumption, the equation for the phase difference dynamics, Eq. (30), can be expressed in potential form as written in Eq. (37) and Eq. (38).

$$\frac{d\phi}{dt} = -\frac{\partial U}{\partial \phi} + \left(\frac{1}{A} + \frac{1}{B}\right)\xi_\phi \tag{37}$$

$$U(A, B, \phi) = \frac{3\kappa}{64}(A^2 + B^2)\cos(2\phi) \tag{38}$$

where $U(A, B, \phi)$ is the phase difference potential.

For given values of A and B, the minima of the phase difference potential are at $\phi = \pm\frac{\pi}{2}$. The accumulation of ϕ in low potential wells at $\pm\frac{\pi}{2}$ and its equivalent values (at 2π spacings) is shown in Figure 14 for experimental data from the first and second azimuthal modes of a gas turbine combustion chamber.

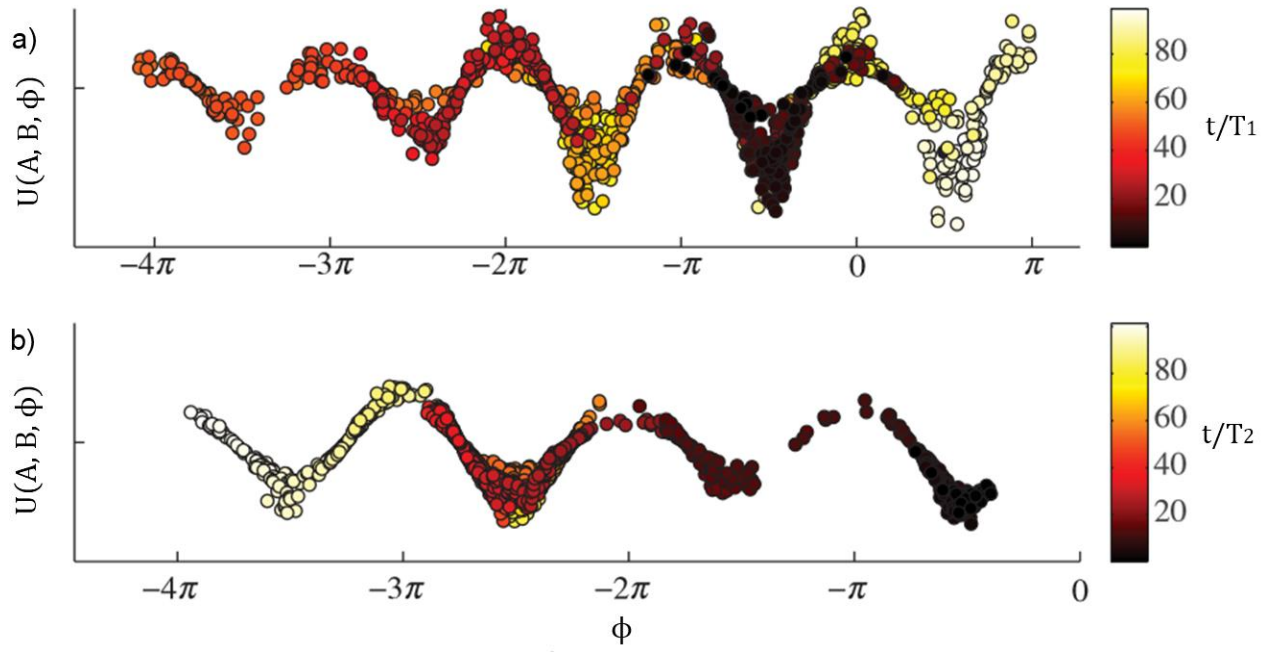

Figure 14: Phase difference potential as a function of phase difference for a) the first azimuthal mode and b) the second azimuthal mode in an annular gas turbine combustion chamber. Each point represents a phase difference value at point in time. The time series for the plot consists of 100 acoustic periods, i.e. $t_{max}/T = 100$ where T is the period (Noiray & Schuermans, PRSA 2013).

Although ϕ covers the entire range of values from 0 to 2π, it remains in potential wells at $\pm\frac{\pi}{2}$ for prolonged periods before stochastic forcing shifts it to another well as seen in Figure 14. If a characteristic ϕ of $\pm\frac{\pi}{2}$ is assumed and also that $\kappa_a \approx \kappa_b$ and $\Gamma_a \approx \Gamma_b$ then simplified versions of Eq. (28) and Eq. (29) are given by Eq. (39) and Eq. (40) in terms of a potential V:

$$\frac{dA}{dt} = -\frac{\partial V}{\partial t} + \xi_a \tag{39}$$

$$\frac{dB}{dt} = -\frac{\partial V}{\partial t} + \xi_b \tag{40}$$

The potential V is given by Eq. (41):

$$V(A,B) = -\frac{\nu_a}{2}A^2 - \frac{\nu_b}{2}B^2 + \frac{9\kappa}{128}(A^4 + B^4) + \frac{3\kappa}{64}(A^2B^2) - \frac{\Gamma}{4{\omega_0}^2}\ln(AB) \tag{41}$$

For this simplified system, there is an analytical solution to the Fokker-Planck stationary PDF given by Eq. (42):

$$P(A,B) = \frac{1}{N}\exp\left(-\frac{4{\omega_0}^2}{\Gamma}V(A,B)\right) \tag{42}$$

where N is a normalisation constant such that $P(A,B)$ is a PDF.

A comparison of the first and second azimuthal mode PDFs given by Eq. (42) (using the parameters extracted with the 2D Fokker-Planck coefficients method) with the experimental PDFs of an unstable gas turbine chamber is presented in Figure 15. While a good agreement is obtained for both modes, the first azimuthal has a more precise match. This may be attributed to a clearer domination of ϕ potential wells at $\pm\frac{\pi}{2}$ in the first azimuthal mode than in the second as can be observed in Figure 14.

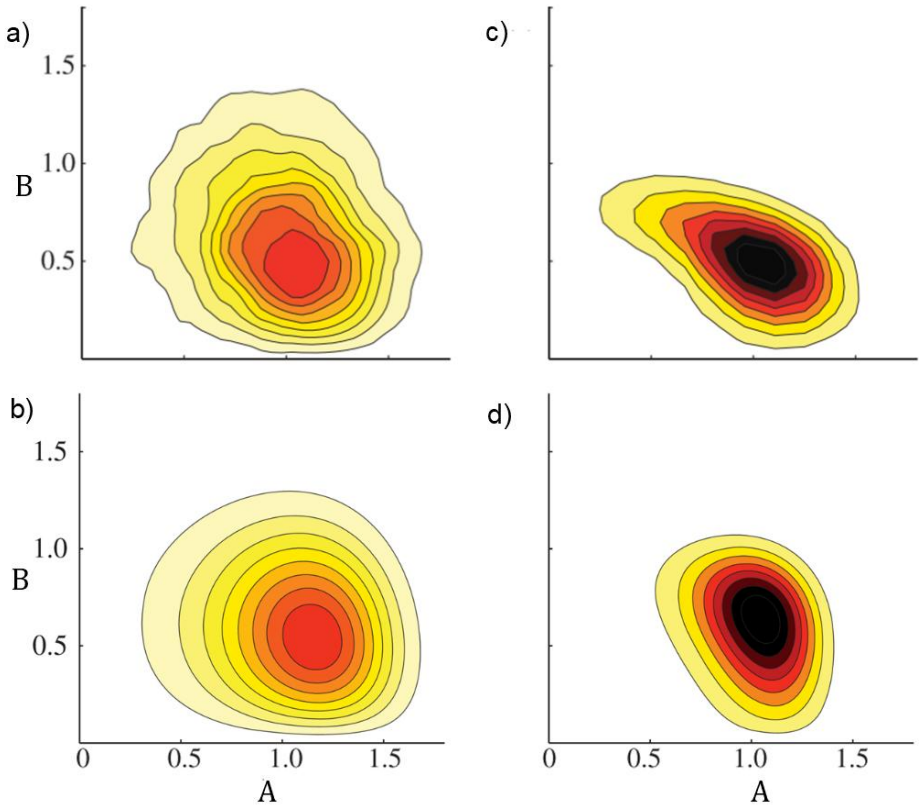

Figure 15: Experimental PDFs of A and B for a) the first azimuthal mode and c) the second azimuthal mode of an unstable gas turbine combustion chamber; these can be compared with analytical PDFs in b) and d) respectively. The analytical PDFs use parameters extracted with the 2D Fokker-Planck coefficients method (Noiray & Schuermans, PRSA 2013).

It is noted that Schulze (2016) attempted to match a simplified version of the 2D dynamics presented in this section (not the discussed 2D simplified model) to experimental data for two stable and two unstable BKD load points. This approach does not involve a Fokker-Planck formulation; consisting of simply matching the parameters to be extracted to the experimental dynamics, i.e. the amplitude envelope and its derivative. However, this approach did not provide accurate growth rate values for the stable load points with respect to those found with Lorentzian fitting. Since the approach of Schulze (2016) did not yield accurate values, and is fundamentally different to that undertaken in this work (i.e. not based on statistical behaviour), a more detailed discussion of this approach is not presented.

The good agreements between the analytical and experimental dynamics that are observed in Figure 15 complement the results in Figure 13. They provide a clear indication that the assumed dynamical model is correct. However, since there is no active acoustic control study with a gas turbine chamber or with a cylindrical combustor in literature, a validation of the parameter extraction or of the underlying dynamics is not present for the 2D Fokker-Planck coefficients method. For linear conditions, a comparison between the results of this advanced method and a simple Lorentzian fit has also not been carried out. Hence further study is required to better establish the reliability of the 2D Fokker-Planck coefficients method, as well as to test its applicability to rocket engine conditions which feature rougher, non-premixed combustion.

2.5 Literature Gap Statements

Two main gaps in the research literature have been identified in this review.

- Methods to extract system-identifying parameters from dynamic pressure time series have been successfully applied to gas turbine conditions. These may be applicable to rocket engine conditions but this is yet to be tested.
- A validation of parameters extracted with the 2D Fokker-Planck coefficients method has not been carried out in gas turbine literature, including linear conditions where a Lorentzian fit can be used to reliably find parameters.

This project will form research objectives around the identified literature gaps.

3. Aim, Objectives and Methodology

This chapter outlines the aim, objectives and methodology of this work. The aim of this work is:

- *To extract key parameters governing thermo-acoustic behaviour in rocket combustors from dynamic pressure measurements using stochastic signal processing techniques.*

The stated aim is broken down into three main objectives. The methodology of this work consists of applying the signal processing methods, as already described in detail in chapter 2, to experimental BKH and BKD data to achieve the three objectives. The three objectives and their associated signal processing techniques (methods) are:

1. Apply the 1D Fokker-Planck coefficients method to the first longitudinal (1L) and 1T modes of multiple BKH load points. These are linear, stable load points since BKH is naturally stable at all experimented load points. Due to linearity, results can be validated by fitting a Lorentzian profile to the PSD of dynamic pressure data (method 1). If a good match is observed between the Lorentzian profile and the experimental data then the extracted parameters can be regarded as reliable since the Lorentzian method is well established. Additionally, parameters extracted using the Lorentzian method are to be fed into the alternative methods for linear conditions (method 1 alternatives), and into the stationary PDF expression (method 3). Positive comparisons of these analytical expressions with experimental data serve as a check that the Lorentzian-extracted parameters are correct, and are consistent with the models assumed for the acoustic amplitude envelope and its PDF at linear conditions.
2. Apply the 2D Fokker-Planck coefficients method to the 1T mode of a stable BKD load point. Due to linearity, results can be validated by fitting Lorentzian profiles to the PSDs of acoustic pressure reconstructions of the A and B modes. Additionally, a phase difference analysis and a comparison of the 2D stationary PDF expression with experimental data provide indications of the validity of the assumed 2D linear dynamics and of the applicability of the 2D simplified model.
3. Carry out a phase difference analysis of the 1T mode of an unstable BKD load point. This provides an indication of the applicability of the 2D simplified model, and of the associated 2D stationary PDF expression. This expression may be useful in future work to compare a simulated 2D PDF, using parameters extracted from applying the Fokker-Planck coefficients method to an unstable case, to the experimental 2D PDF of an unstable case in order to gain an indication of the accuracy of parameter extraction in non-linear conditions.

The experimental data used in this work was obtained in past experiments at the DLR Lampoldshausen, and details of its processing are presented in Appendix B. Details of the creation of PSDs in this work are also presented in Appendix B, where the effects of statistical errors on parameter extraction are discussed and found to be negligible for the generated PSDs.

4. Results for Test Case 1: Rectangular Stable Combustor

This chapter presents the data analyses of BKH load points. These analyses fulfil objective 1 as set out in section 3. The data analyses were carried out with measurements from the dynamic pressure sensor 'PCCdyn2', shown in Figure 16. This sensor is situated at the pressure anti-node of the BKH 1T mode, and is also removed from local disturbances generated by the secondary nozzle. A summary of the results of BKH data analyses is provided at the end of the chapter.

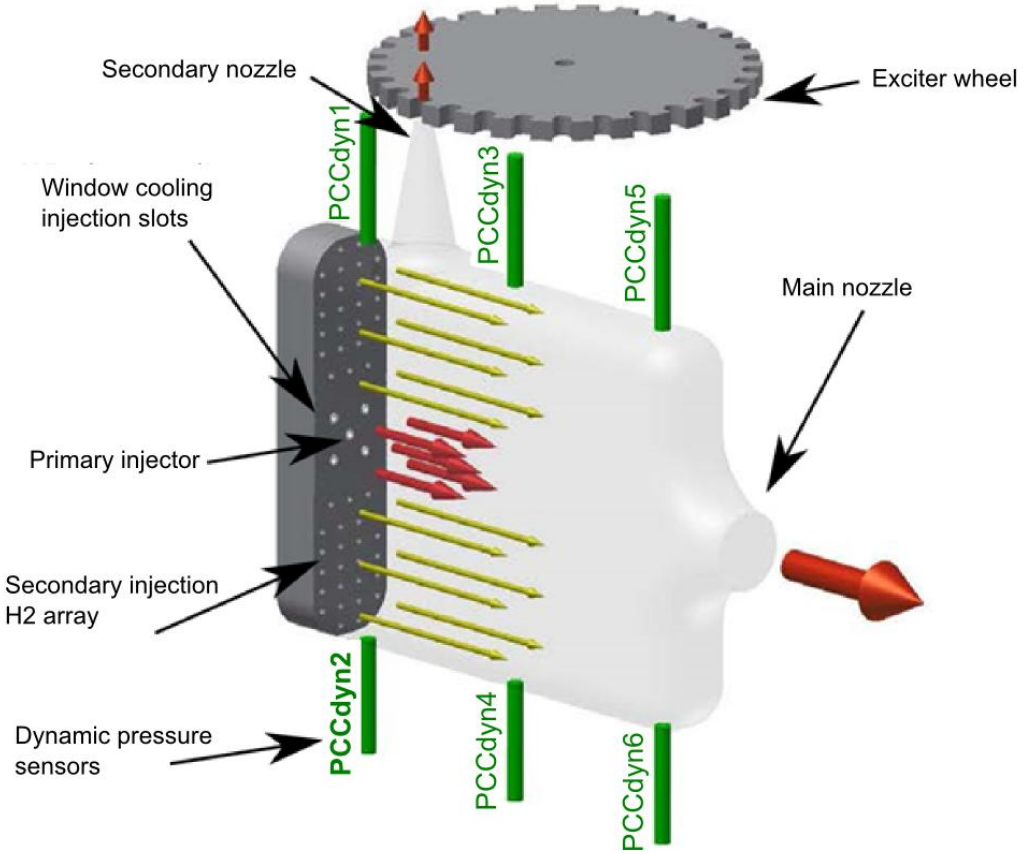

Figure 16: Six dynamic pressure sensors positioned along the walls of BKH. The 'PCCdyn2' sensor measurements are used for BKH data analyses (Webster S. L., 2016).

4.1 BKH Load Points and Lorentzian Parameter Extraction

This section presents the BKH load points selected for data analyses, and their modal growth rates and noise intensities extracted from Lorentzian fits. Four unforced BKH load points (with no acoustic excitation from the secondary nozzle) were selected for analysis. These entail two load points with a relatively high H_2 injection temperature, or so-called gaseous hydrogen (GH2), and two points with low H_2 injection temperature, or liquid hydrogen (LH2), which feature a low VR. Within the GH2 and LH2 sets there is a supercritical point at 60 bar of chamber pressure and a subcritical point at 40 bar. All four load points have a ratio of oxidiser-to-fuel mass flow (ROF) of 6. The details of the load points are specified in Table 1.

Table 1: Selected BKH load points and corresponding operating parameters.

BKH load point	ROF (-)	VR (-)	$T_{H2\ injection}$ (K)
GH2, 60 bar	6	36	287.8
GH2, 40 bar	6	55	288.2
LH2, 60 bar	6	7.6	64.1
LH2, 40 bar	6	13	73.1

For each of the operating points, the acoustic response of the 1L, 1T and first longitudinal first tangential (1L1T) BKH modes to noise has been measured in experiments. By applying Lorentzian fits to the PSDs of acoustic pressure for each of these modes the growth rate ν and the noise intensity Γ can be extracted. Lorentzian fits for the three modes of each of the load points are shown in Appendix C. While good Lorentzian fits are obtained for all cases, the 1L mode of the LH2 60 bar load point is considered the 'cleanest' case based on its undisturbed and precise Lorentzian profile. This Lorentzian fit for the LH2 60 bar 1L mode is shown in Figure 17. The time series length for this case is 10 seconds, and is selected from an experimental run time where the mode is unexcited by the secondary nozzle, as shown in Appendix C, together with the rest of the cases. The peak frequencies (approximately the natural frequencies ω_0), growth rates and noise intensities extracted with Lorentzian fits are presented in Table 2. The experimental PSDs presented in this work are one-sided, and hence when extracting Γ a factor of 2 is taken into account with respect to the equations in section 2.4.1 as detailed in Appendix A.

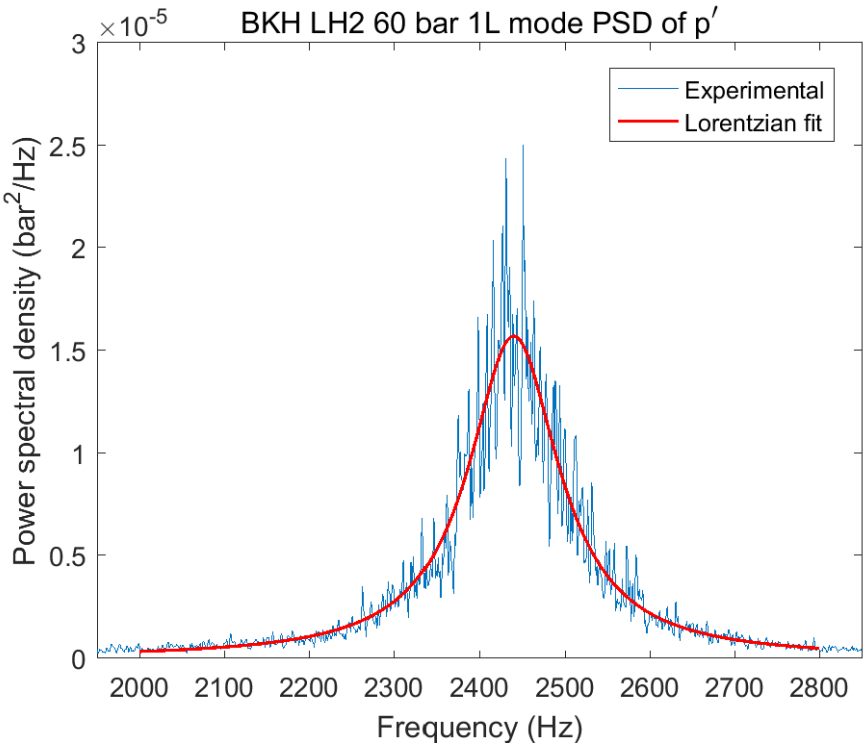

Figure 17: BKH LH2 60 bar 1L mode Lorentzian fit. The Lorentzian fit is optimised with a least squares error algorithm.

Table 2: Parameters extracted with optimised Lorentzian fits for the selected BKH load points. The peak frequency of a Lorentzian fit approximates the natural frequency ω_0.

BKH load point	Time series length (s)	Peak frequency $\omega_0/2\pi$ (Hz)	Growth rate $\nu/2\pi$ (Hz)	Noise intensity Γ (10^9 bar^2 s^{-3})
GH2, 60 bar				
1L	5	3250	-117	5.65
1T	10	4378	-67.2	0.980
1L1T	10	5432	-52.4	0.550
GH2, 40 bar				
1L	5	3157	-129	2.32
1T	10	4280	-73.1	0.505
1L1T	10	5325	-61.1	0.293
LH2, 60 bar				
1L	10	2440	-64.8	1.23
1T	10	4095	-63.0	2.00
1L1T	8	4958	-28.5	0.373
LH2, 40 bar				
1L	8	2378	-61.4	0.565
1T	10	4152	-76.6	0.403
1L1T	10	4977	-39.9	0.118

The results in Table 2 generally agree with expectations from literature. The mean net damping rates for the BKH 1L and 1T modes experimentally measured by Webster (2016) over many load points, and using both of the BKH-specific methods discussed in section 2.2, are 113 Hz and 72.4 Hz respectively. These values agree well with the growth rate results obtained in this work for the GH2 cases. A significant reduction in the absolute growth rate values of the 1L and 1L1T modes is observed for the low VR, LH2 cases. This agrees with the observations of significant VR influence on damping by Webster (2016).

The noise intensities are reduced with higher modal frequencies as would be expected from the turbulent energy cascade which is the origin of the stochastic noise. For the GH2 cases, the noise intensity is reduced by a factor of 5 from the 1L to the 1T mode, and by a factor of 2 from the 1T mode to the 1L1T mode. The LH2 cases have lower noise intensities and more gradual noise decays than the GH2 cases, while higher noise intensities are observed at higher chamber pressure for both GH2 and LH2 injection. Trends consistent with these results were observed by Webster et al. (2015) in unforced BKH experimental data (no excitation from the secondary nozzle); greater noise levels for higher chamber pressure and higher VR. The only inconsistency present in the extracted parameters is a higher noise intensity for the 1T than the 1L mode of the LH2 60 bar load point. In summary, the parameters found with Lorentzian fitting exhibit general trends consistent with those established in prior BKH studies.

4.2 Alternative Methods for Linear Conditions

The parameters extracted from Lorentzian fitting can be fed into the analytical expressions for alternative linear methods. This serves as a check that the Lorentzian-extracted parameters are correct, and consistent with the dynamical models assumed for the acoustic amplitude envelope and its PDF at linear conditions. For the LH2 60 bar 1L mode, good comparisons between data and the analytical expressions for the PSD of amplitude fluctuation, the cut-off frequency of the PSD of amplitude, and the Fokker-Planck stationary PDF of amplitude at linear conditions (Eq. (15) without the non-linear term) are shown in Figure 18, Figure 19 and Figure 20, respectively. These good fits, together with the Lorentzian fit of Figure 17, show that the LH2 60 bar 1L mode dynamics can be accurately described with the assumed linear model of Eq. (1), and the subsequent manipulations of Eq. (1) to describe the amplitude envelope and its PDF.

It is noted that the random error observable in the PSDs of Figure 17 and Figure 18 is typical of dynamic pressure signals in rocket combustion chambers. This random error is attributable to significant fluctuations in the combustion noise spectrum, which are caused by the highly turbulent rocket flames. In reality, the spectrum of the stochastic heat release driving would not be perfectly flat like theoretical white noise, but significantly jagged.

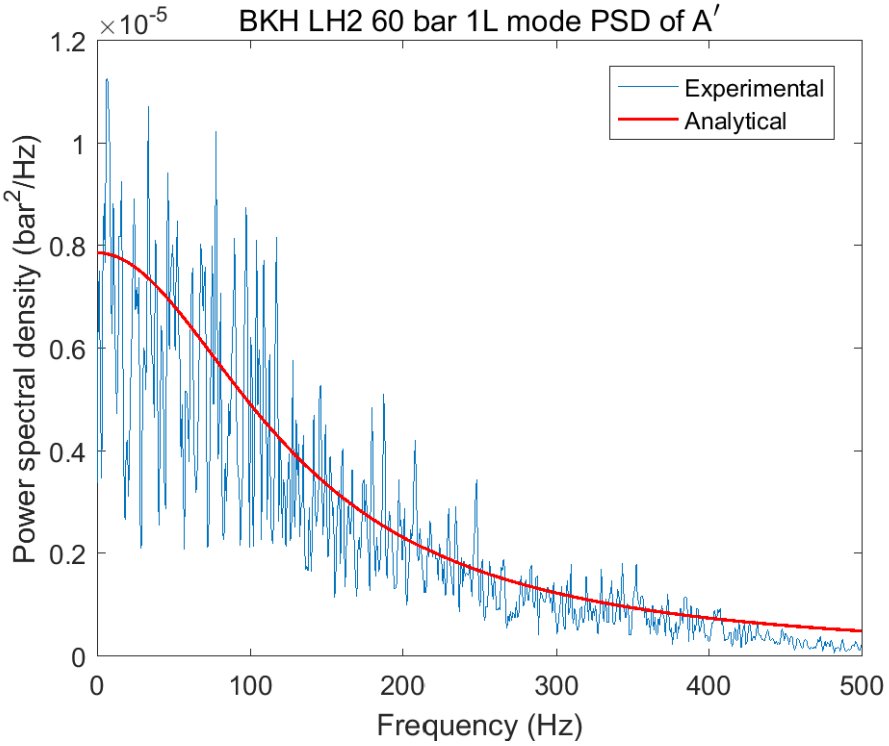

Figure 18: BKH LH2 60 bar 1L mode PSD of amplitude envelope fluctuation. The analytical expression uses parameters obtained from Lorentzian fitting.

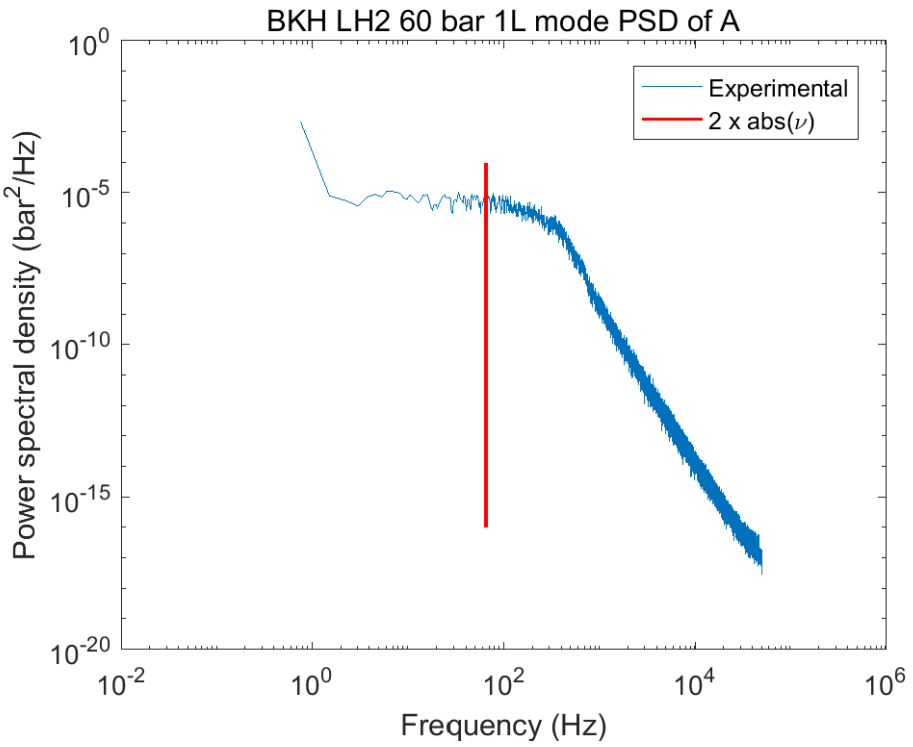

Figure 19: BKH LH2 60 bar 1L mode PSD of amplitude envelope. The cut-off frequency expectation; the frequency at which the PSD begins to decay, uses the growth rate obtained from Lorentzian fitting.

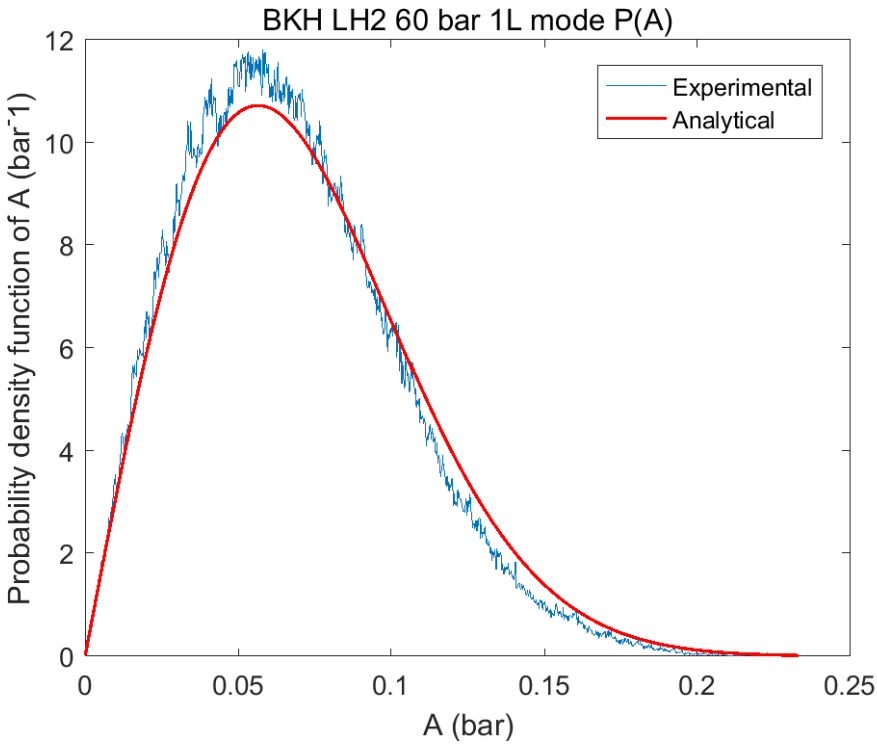

Figure 20: BKH LH2 60 bar 1L mode Fokker-Planck stationary PDF of amplitude envelope, compared with experimental data. The stationary PDF analytical expression uses parameters obtained from Lorentzian fitting.

4.3 1D Fokker-Planck Coefficients Method Application

This section presents the results of applying the 1D Fokker-Planck coefficients method to the 1L and 1T modes of the four BKH load points presented in section 4.1. Data for the 1L1T modes was not considered clean enough for the application of the Fokker-Planck coefficients method as discussed in Appendix C, section C2. A detailed analysis of the LH2 60 bar 1L mode is presented, and results for the other load points are tabulated at the end of the section.

A histogram of the amplitude envelope for the LH2 60 bar 1L mode with band-pass filtering from 2000 to 2800 Hz (matching the Lorentzian fit width in Figure 17) is shown in Figure 21. This histogram has a resolution of 100 bins, which is visibly sufficient to describe the statistical amplitude distribution.

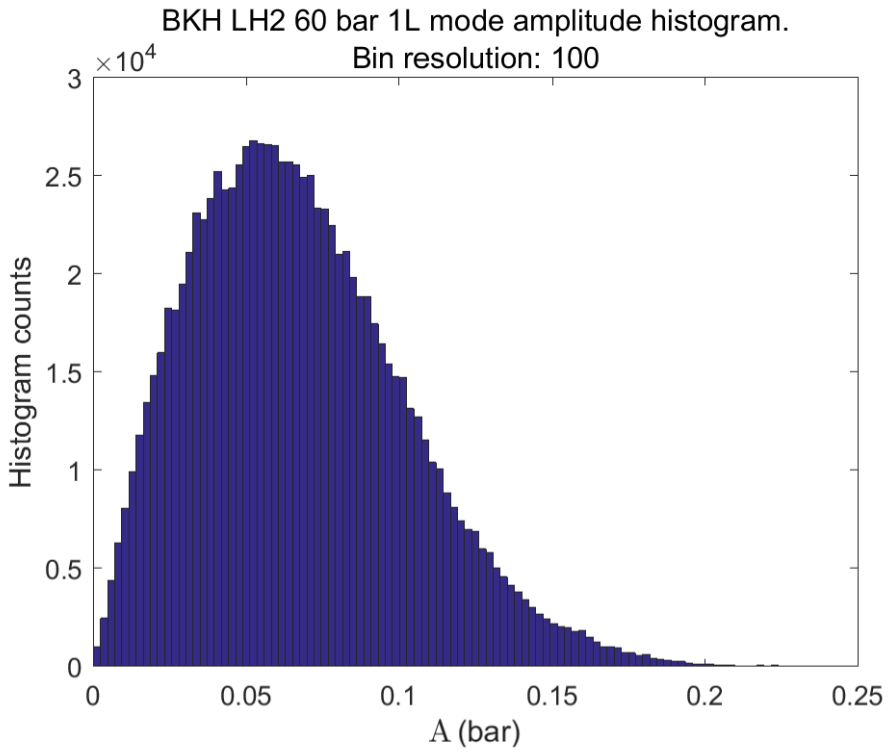

Figure 21: Histogram of the amplitude envelope of the BKH LH2 60 bar 1L mode with band-pass filtering of 2000 to 2800 Hz.

Computations of the first and second transition moments for 10th percentile interval values of the LH2 60 bar 1L mode amplitude are shown in Figure 22. These use a resolution of 100 bins as in Figure 21. It can be observed in Figure 22 that if signal collapses at low τ values (due to finite time effects) are ignored, the computed signals approximate the expected values of the drift and diffusion coefficients (plotted as dots on the y-axes of Figure 22), which are based on the parameters found with Lorentzian fitting, as τ approaches zero. The 80th and 90th percentile signals are of a visibly lower quality than the lower percentiles, which may be attributed to the skew of the amplitude histogram towards lower amplitudes. An evaluation of limits to zero using extrapolations can exclude these lower quality signals at high amplitudes.

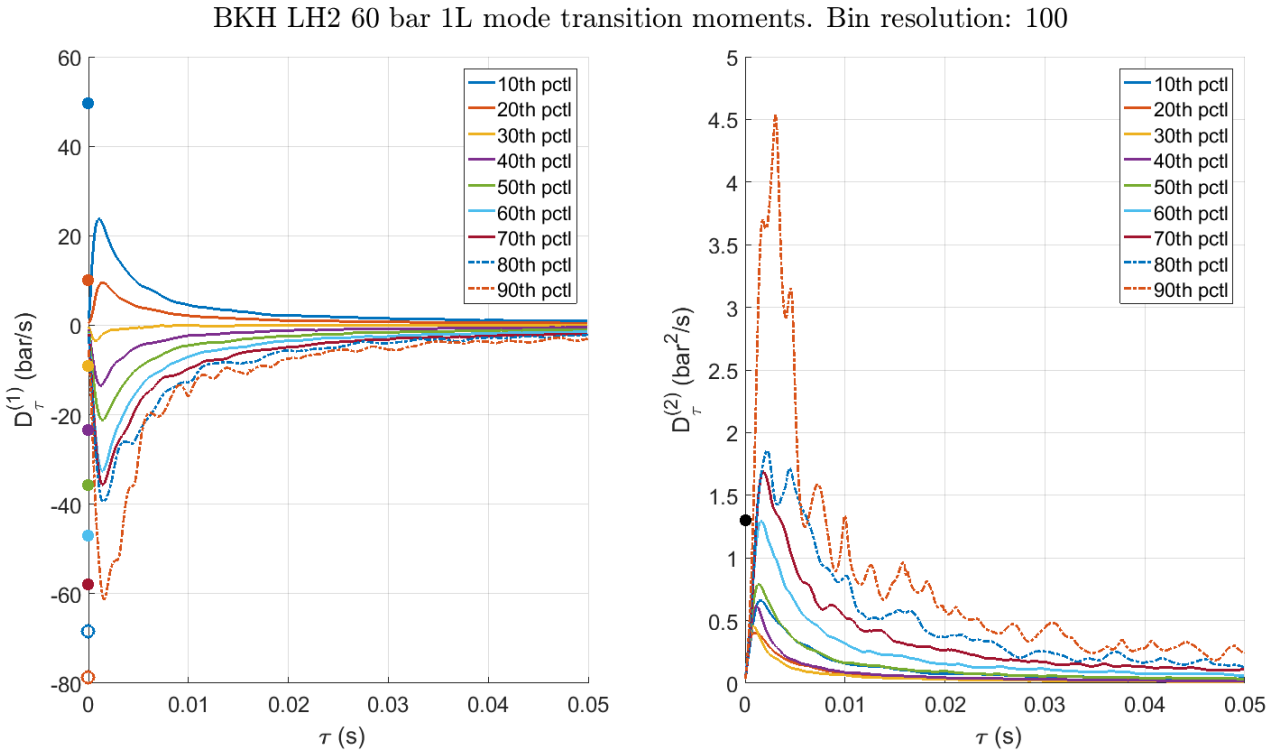

Figure 22: First $D_\tau^{(1)}$ (plot on left) and second $D_\tau^{(2)}$ (plot on right) transition moment computations for nine amplitudes at 10th percentile intervals using experimental data of the BKH LH2 60 bar 1L mode with band-pass filtering from 2000 to 2800 Hz. The limits to zero of the $D_\tau^{(1)}$ and $D_\tau^{(2)}$ computations correspond to the amplitude-dependent drift coefficient and the amplitude-independent diffusion coefficient respectively. Dots on the y-axes show the expected values based on parameters found with Lorentzian fitting. Finite time effects cause the signals to collapse at low τ values, and deviate from their true limits to zero.

Two extrapolation methods to evaluate the limits to zero of the transition moment signals were examined. These are a simple exponential function and a compound exponential function given by Eq. (41) and Eq. (42), respectively.

$$y = ab^{-fx} \tag{41}$$

where a and b are fitted to two points (x_1, y_1) and (x_2, y_2) and f is any non-zero constant.

$$y = a(bx^c)^{-x} \tag{42}$$

where a and b are fitted to two points (x_1, y_1) and (x_2, y_2) for a given value of the constant c.

The simple exponential extrapolation consists of fitting a and b to two points in a signal. The value of the constant f is non-effectual since any changes to f are absorbed into a and b such that the obtained function is the same. The only consideration in this extrapolation approach is deciding the signal points (x_1, y_1) and (x_2, y_2) to which the simple exponential is to be fitted. BKH transition moment signals, shown in Figure 22, peak at maxima or minima before collapsing towards zero at low τ values. Hence these maxima and minima are used for (x_1, y_1). The selection of (x_2, y_2) is arbitrary; it must include enough of the signal such that its overall behaviour is captured, but not an excessive length such that the extrapolation still focuses on low τ values. A value of x_2 = 0.025 s was chosen for all BKH signal extrapolations. Such an extrapolation is depicted in Figure 23 for the LH2 60 bar 1L mode, where smalls dots plotted in the y-axis mark the obtained limits to zero based on simple exponential extrapolations. It can be seen from Figure 23 that simple exponentials do not capture signal curvatures appropriately.

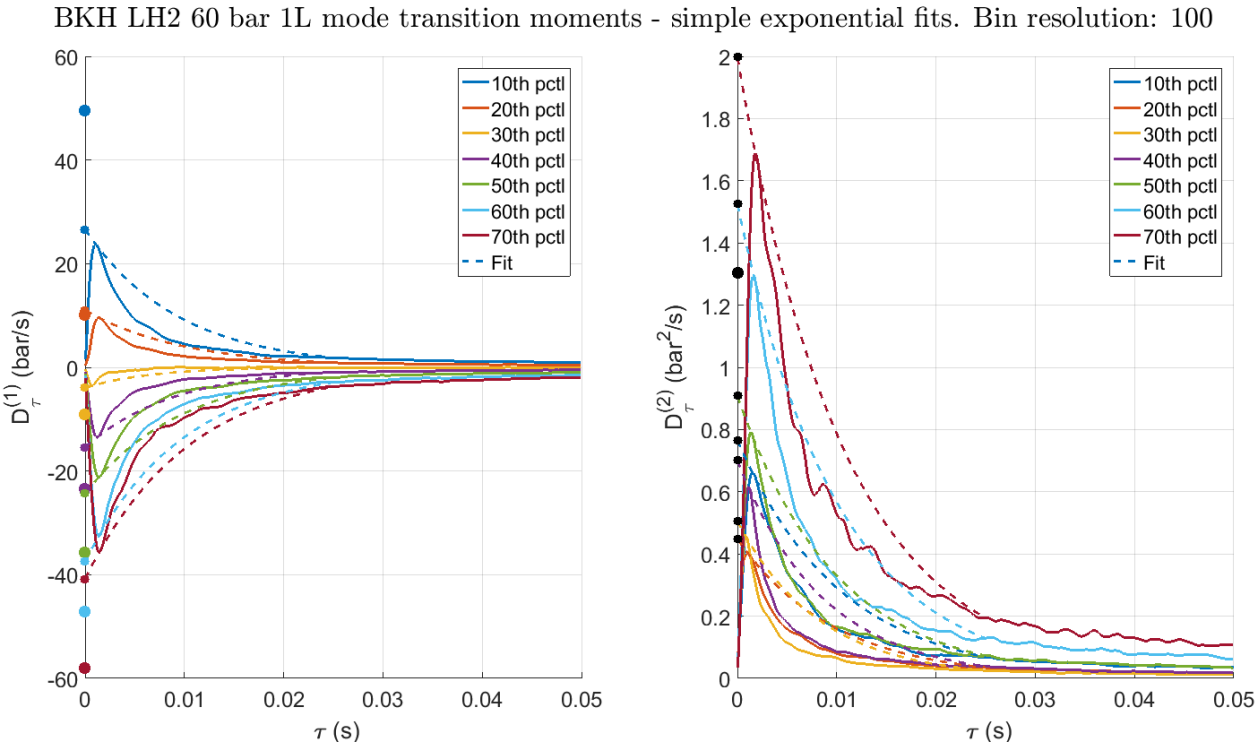

Figure 23: First $D_\tau^{(1)}$ (plot on left) and second $D_\tau^{(2)}$ (plot on right) transition moment computations for seven amplitudes at 10th percentile intervals using experimental data of the BKH LH2 60 bar 1L mode with band-pass filtering from 2000 to 2800 Hz. The limits to zero of the $D_\tau^{(1)}$ and $D_\tau^{(2)}$ computations correspond to the amplitude-dependent drift coefficient and the amplitude-independent diffusion coefficient respectively. Dotted lines are simple exponential extrapolations used to find the limits to zero of the signals. Small dots on the y-axes are the limits to zero obtained with extrapolations, while big dots are the expected values based on parameters found with Lorentzian fitting.

The compound exponential function has a constant c which can be used to modify the curvature of exponential extrapolations to closely match signal behaviour. It is noted that this function given by Eq. (42) is not present in existing literature. An optimisation algorithm was implemented which iterates through values of c until the least squares error between the signal and the extrapolation is minimised. The algorithm devised was found to be sensitive to the initial guess for c and hence different initial guesses were tested by the author until good extrapolations were obtained. For

the LH2 60 bar 1L mode, an initial guess of c = -70 s^{-1} was found to yield good extrapolations for all signals (the obtained individual c values are in Appendix C). These compound exponential extrapolations are shown in Figure 24. It can be seen from Figure 24 that compound exponential extrapolations closely follow the signal curvatures.

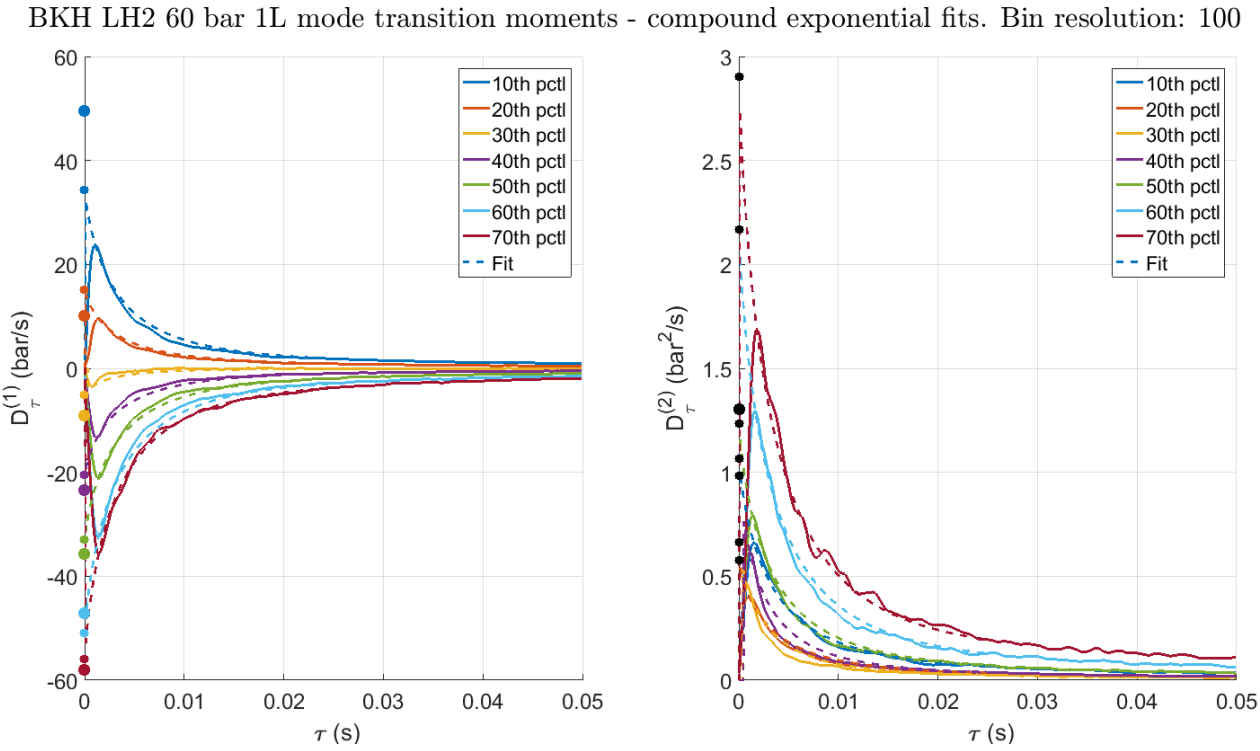

Figure 24: First $D_\tau^{(1)}$ (plot on left) and second $D_\tau^{(2)}$ (plot on right) transition moment computations for seven amplitudes at 10th percentile intervals using experimental data of the BKH LH2 60 bar 1L mode with band-pass filtering from 2000 to 2800 Hz. The limits to zero of the $D_\tau^{(1)}$ and $D_\tau^{(2)}$ computations correspond to the amplitude-dependent drift coefficient and the amplitude-independent diffusion coefficient respectively. Dotted lines are compound exponential extrapolations used to find the limits to zero of the signals. Small dots on the y-axes are the limits to zero obtained with extrapolations, while big dots are the expected values based on parameters found with Lorentzian fitting.

After an appropriate extrapolation is used to obtain the limits to zero of transition moments, these limits can be equated to analytical expressions for the Fokker-Planck drift and diffusion coefficients as written in Eq. (18) and Eq. (19) in section 2.4.6. The noise intensity Γ can be found from taking an average of the limits to zero of the second transition moments for the considered amplitudes. This average can then be equated to the diffusion coefficient $\frac{\Gamma}{4{\omega_0}^2}$.

Since all the BKH load points have linearly stable modes (as explained in Appendix C, section C2), the non-linear term in Eq. (17) can be ignored and only the growth rate ν remains to be found. The growth rate can be extracted by a least squares error optimisation of the analytical expression for $\mathcal{F}(A)$ to fit the limits to zero of the first transition moments for the considered amplitudes. Unlike the extrapolation optimisation, this parameter extraction optimisation was robust (i.e. independent of the initial guess for ν).

The extracted growth rate using this method is -64.6 Hz which precisely matches the Lorentzian growth rate of -64.8 Hz. The noise intensity found from the diffusion coefficient is 1.29×10^9 bar^2 s^-

^{3} which also agrees precisely with the Lorentzian noise intensity of 1.23×10^9 bar^2 s^{-3}. Therefore, for the LH2 60 bar 1L mode, the Fokker-Planck coefficients method yields parameters with less than 5% error with respect to those found with Lorentzian fitting.

It is of interest to investigate the effect of reducing the band-pass filter width around the LH2 60 bar 1L mode when applying the Fokker-Planck coefficients method. This interest arises from the common occurrence of closely neighbouring modes in the acoustic spectrum of a combustor, which reduces the frequency range for band-pass filtering around the mode of interest. The first step of this analysis is to establish a pass band which is exactly symmetric around the Lorentzian peak frequency (2440 Hz), in order to eliminate any possible asymmetry effects - these can be considered separately. Such filtering would be from 2080 Hz to 2800 Hz (instead of the original 2000 to 2800 Hz). The centre-to-cut-off width of this band-pass filter is $5.56 \times \nu$, that is 5.56 times the growth rate. The width of this symmetric band-pass filter can be reduced until significant errors in the parameter extraction are observed.

The results of the band-pass filter analysis are presented in Table 3, where they can be compared to Lorentzian fit results. It can be seen from Table 3 that a minimum centre to cut-off width of $2 \times \nu$ is required to estimate parameters. With this filtering width, errors of 13% and 32% are present for the growth rate and noise intensity respectively, in comparison to Lorentzian parameters. It is also of interest to consider the effect of increasing the filter width asymmetrically. If a band-pass filter is taken from $-5 \times \nu$ to $+2 \times \nu$ around the peak frequency instead of at $\pm 2 \times \nu$, the Fokker-Planck coefficients method yields a growth rate of -53.3 Hz (18% error) and a noise intensity of 0.927×10^9 bar^2 s^{-3} (25% error) which is not an improvement on the $\pm 2 \times \nu$ results. Hence, according to this analysis, band-pass filtering for the Fokker-Planck coefficients method should have a minimum centre-to-cut-off width of $2 \times \nu$ which can only be effectively improved symmetrically.

Table 3: Symmetric band-pass filter analysis.

Method	Centre-to-cut-off width of symmetric band-pass filter	Growth rate $\nu/2\pi$ (Hz)	Noise intensity Γ (10^9 bar^2 s^{-3})
Lorentzian fit	N.A. (2000, 2800 Hz)	-64.8	1.23
Fokker-Planck coefficients	$5.56 \times \nu$	-64.0	1.35
Fokker-Planck coefficients	$5 \times \nu$	-65.0	1.23
Fokker-Planck coefficients	$4 \times \nu$	-64.6	1.13
Fokker-Planck coefficients	$3 \times \nu$	-66.1	1.39
Fokker-Planck coefficients	$2 \times \nu$	-56.5	0.842
Fokker-Planck coefficients	$1.5 \times \nu$	-44.4	0.539

The Fokker-Planck coefficients method was applied to the 1L and 1T modes of the four BKH load points studied in this work. The approach taken for all modes is the same as that already described for the LH2 60 bar 1L mode. The noise intensity is obtained from the diffusion coefficient, and the growth rate is obtained from a robust optimisation of the analytical expression for the drift coefficient. Details of the data processing and the parameter extraction results for all processed modes are presented in Table 4. The data used for the Fokker-Planck coefficients method was band-pass filtered using the original Lorentzian fit widths for all modes except for the LH2 40 bar 1T mode. These Lorentzian fit widths are approximately symmetric around the peak frequency (which cannot be precisely known until a Lorentzian fit is applied with a pre-determined width), except for the LH2 40 bar 1T mode. In this case, a reduction in the band-pass filtering to obtain symmetry around the peak frequency was found to improve the results given by the Fokker-Planck coefficients method. For all cases, the shorter centre-to-cut-off width of the band-pass filter is specified in Table 4.

Interestingly, good results are obtained for cases with filter widths encompassing less than $2 \times \nu$. Table 4 also shows that the 80^{th} percentile amplitude was included for the GH2 60 bar and 40 bar 1L mode analyses, and that an initial guess of $c = -150\ s^{-1}$ was used for the GH2 extrapolation optimisations. These modifications were found to yield better results.

Errors for parameter extraction using the Fokker-Planck coefficients method with respect to Lorentzian fitting are highlighted in Table 4 in italic text. It can be seen that the parameters extracted with the Fokker-Planck coefficients method agree well with Lorentzian values in all cases.

Table 4: Details of the data processing and the parameter extraction results for the 1L and 1T modes of the BKH load points. The errors of the Fokker-Planck coefficients method compared to Lorentzian fitting are highlighted in italic text.

Variable	BKH load point, acoustic mode							
	GH2				LH2			
	60 bar, 1L	**60 bar, 1T**	**40 bar, 1L**	**40 bar, 1T**	**60 bar, 1L**	**60 bar, 1T**	**40 bar, 1L**	**40 bar, 1T**
Lorentzian fit width (Hz)	2800, 3650	4250, 4500	2850, 3450	4150, 4400	2000, 2800	3800, 4400	2150, 2600	3900, 4300
Fokker-Planck coefficients band-pass filter (Hz)	2800, 3650 [3.4 × ν]	4250, 4500 [1.8 × ν]	2850, 3450 [2.3 × ν]	4150, 4400 [1.6 × ν]	2000, 2800 [5.6 × ν]	3800, 4400 [4.7 × ν]	2150, 2600 [3.6 × ν]	4000, 4300 [1.9 × ν]
Maximum amplitude percentile considered	80^{th}	70^{th}	80^{th}	70^{th}	70^{th}	70^{th}	70^{th}	70^{th}
Initial guess for c (s^{-1})	-150	-150	-150	-150	-70	-70	-70	-70
Lorentzian $\nu/2\pi$ (Hz)	-117	-67.2	-129	-73.1	-64.8	-63.0	-61.4	-76.6
Fokker-Planck coefficients $\nu/2\pi$ (Hz)	-99.5	-80.2	-102	-76.4	-64.6	-51.9	-64.3	-62.5
Error for ν	*15%*	*19%*	*21%*	*4.5%*	*0.3%*	*18%*	*4.7%*	*18%*
Lorentzian Γ (10^9 bar^2 s^{-3})	5.65	0.980	2.32	0.505	1.23	2.00	0.565	0.403
Fokker-Planck coefficients Γ (10^9 bar^2 s^{-3})	5.10	1.20	1.80	0.410	1.29	1.58	0.631	0.314
Error for Γ	*10%*	*22%*	*22%*	*19%*	*4.9%*	*21%*	*12%*	*22%*

4.4 Summary of Results for Test Case 1

The growth rate and noise intensity of BKH acoustic modes at different operating conditions were extracted with Lorentzian fitting and the Fokker-Planck coefficients method. Good Lorentzian fits were obtained for the 1L, 1T and 1L1T modes of four unforced BKH load points, as would be expected for linearly stable cases. These load points are defined by hot or cold hydrogen injection (GH2 vs LH2), and by supercritical or subcritical pressures (60 bar vs 40 bar). The growth rates and noise intensities obtained with Lorentzian fits for the three acoustic modes of the four load points exhibit general trends consistent with BKH studies by Webster (2016) and Webster et al. (2015).

A detailed data analysis was presented for the LH2 60 bar 1L mode which is considered the 'cleanest' case based on its undisturbed and precise Lorentzian profile. The Lorentzian parameters were fed into the analytical expressions of alternative methods for linear conditions consisting of the PSD of amplitude fluctuation, the cut-off frequency of the PSD of amplitude, and the Fokker-Planck stationary PDF. These analytical expressions all compare well with experimental data. These comparisons serve as a check for the Lorentzian parameters and provide further indication that the assumed linear dynamical model is correct.

The application of the Fokker-Planck coefficients method to the LH2 60 bar 1L mode was presented in detail. A compound exponential function was found to provide appropriate signal extrapolations that establish the limits to zero of the transition moments. Consequently, the noise intensity was obtained from the diffusion coefficient (equal to the limit to zero of the second transition moment), while the growth rate was obtained from optimising the analytical expression for the drift coefficient (equal to the limit to zero of the first transition moment). This paramater extraction using the Fokker-Planck coefficients yielded values in close agreement with Lorentzian parameters, with an error of 0.3% for the growth rate and of 4.9% for the noise intensity of the LH2 60 bar 1L mode.

An analysis of the effects of band-pass filtering width and symmetry was carried out with the experimental data of the LH2 60 bar 1L mode. Significant errors in the parameter extraction were found when the band-pass filter width was symmetrically reduced to a centre to cut-off width of $2 \times \nu$. Asymmetric expansion of the band-pass filter width did not improve the results.

The Fokker-Planck coefficients method was applied to the 1L and 1T modes of the four BKH load points. Good results were obtained for all cases with some variances in the data processing. Band-pass filters approximately symmetric around the peak frequency were used for all the modes. Three cases featured a centre-to-cut-off width lesser than $2 \times \nu$ but good results were still obtained with a maximum parameter error of 22%. Analyses of the 1L modes of the GH2 cases included the 80^{th} amplitude percentile, while analyses for the rest of the modes included up to the 70^{th} percentile. Greater extrapolation coefficients were used for the GH2 cases than for LH2 cases to better match signal curvatures. Overall, there is no systematic trend in the errors for the parameters extracted with the Fokker-Planck coefficients method, with both overpredictions and underpredictions being present with respect to Lorentzian results. Therefore, the Fokker-Planck

coefficients method yielded growth rates and noise intensities for BKH 1L and 1T modes at four different operating conditions with acceptable[2] random errors of less than 25%.

[2] Private communication with Prof N. Noiray

5. Results for Test Case 2: Cylindrical Unstable Combustor

This chapter presents the data analyses of BKD load points. These analyses fulfil objectives 2 and 3 as set out in section 3. The data analyses were carried out with measurements from 8 dynamic pressure sensors 'DYN' 1 to 8 placed around the perimeter of the BKD chamber at 45° to each other, as shown in Figure 25. A summary of the results of BKD data analyses is provided at the end of the chapter.

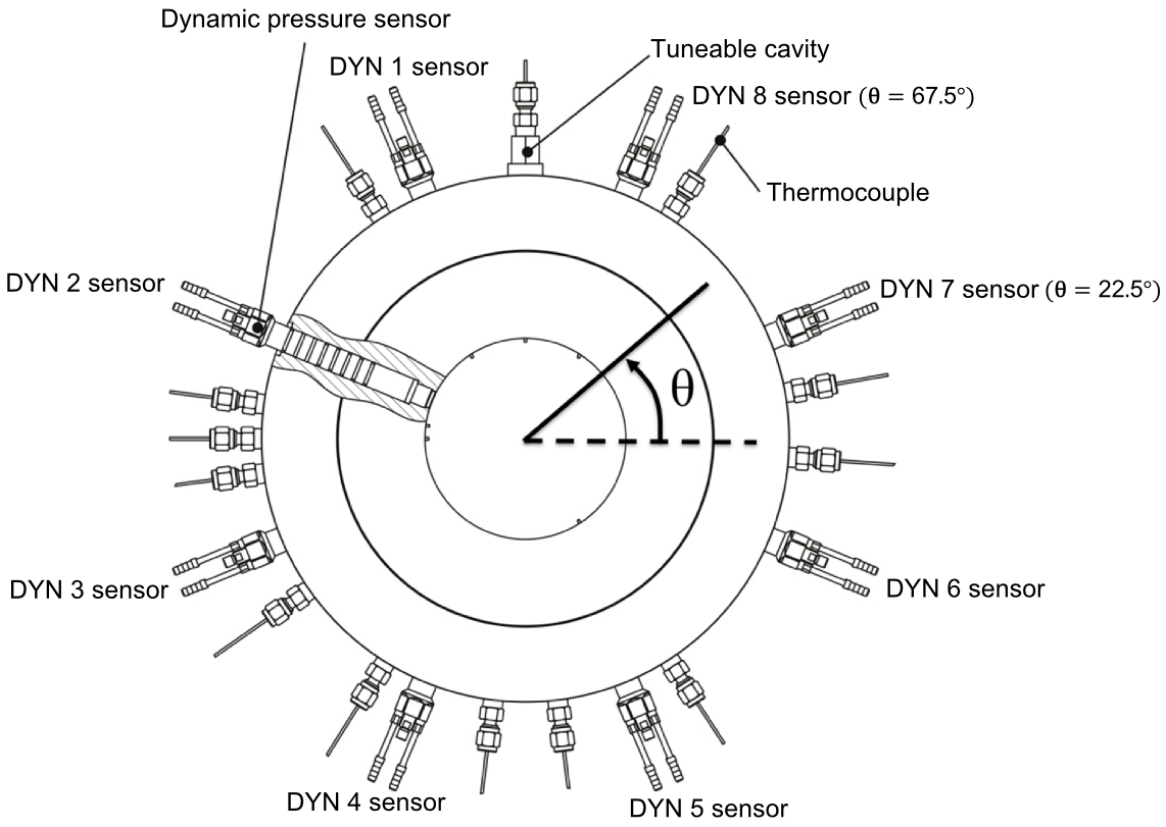

Figure 25: BKD sensor array illustration. The 8 dynamic pressure sensors, positioned at 45° to each other, are labelled DYN 1 to 8.

5.1 BKD Load Points

This section presents the BKD load points selected for the BKD data analyses, which consist of a stable and an unstable load point. These load points were selected from different time segments of an experimental run as shown in Figure 26. The stable load point is named 'LP7' and has a 60 bar chamber pressure and a ROF of 4. The unstable load point is named 'LP4' has an 80 bar chamber pressure and a ROF of 6. Both time series for these load points have a length of 2 s; LP7 was selected from the run time segment 43 to 45 s and LP4 was selected from the run time segment 23 to 25 s. The LP4 instability can be clearly observed in the spectrogram of Figure 26 where the LP4 1T mode is significantly more excited than the LP7 1T mode.

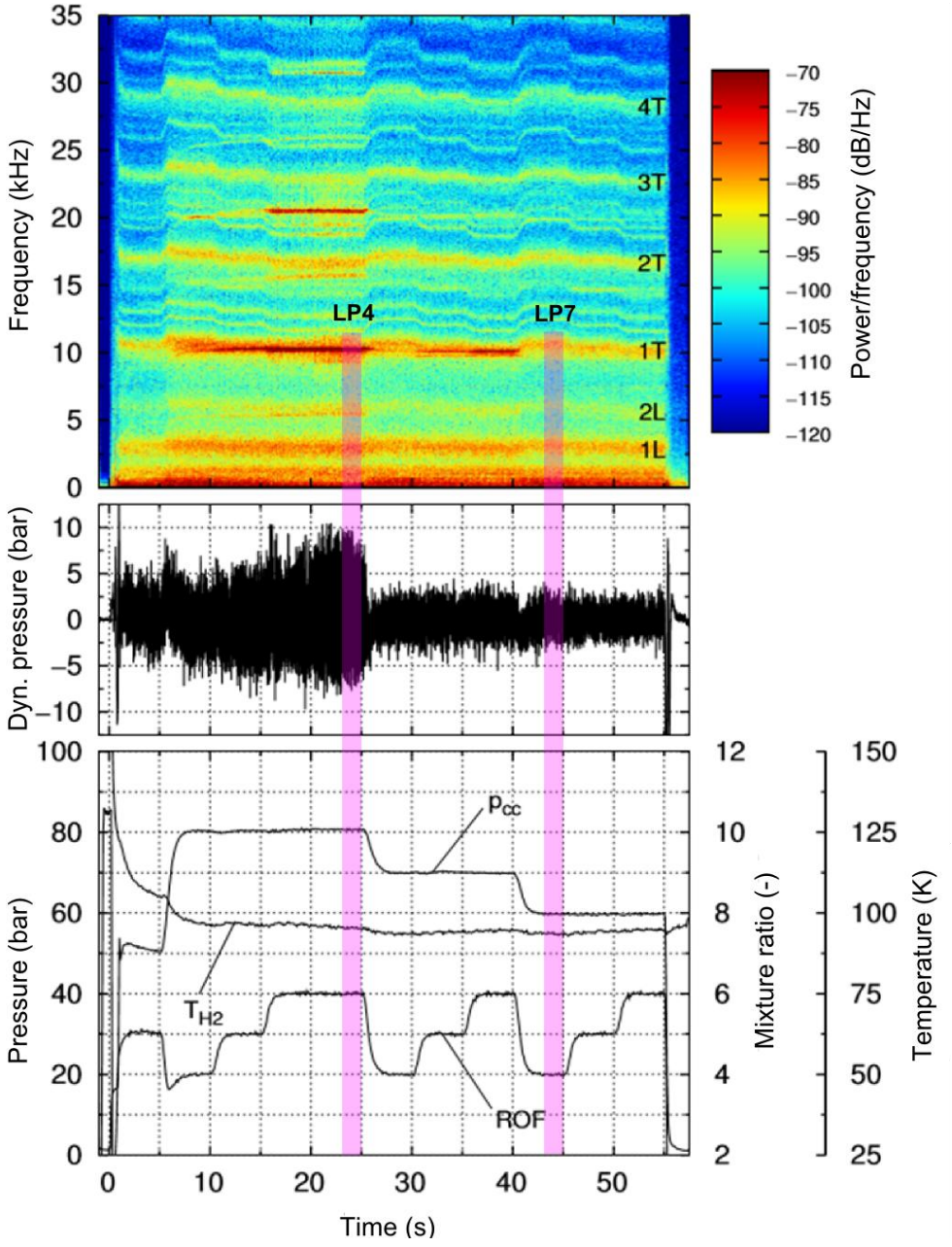

Figure 26: BKD load point selection for the stable load point 'LP7' and the unstable load point 'LP4'. LP7 is selected from the run time segment 43 to 45 s, at a 60 bar chamber pressure and a ROF of 4, which has a stable 1T mode. LP4 is selected from the run time segment 23 to 25 s, at a 80 bar chamber pressure and a ROF of 6, which has an unstable 1T mode (Groning et al., 2016).

The acoustic pressure and amplitude envelope of LP7 and LP4 are shown in Figure 27, while their acoustic pressure PDFs are shown in Figure 28. The relatively high amplitudes and bi-modal PDF shape of LP4 clearly identify this load point as being unstable.

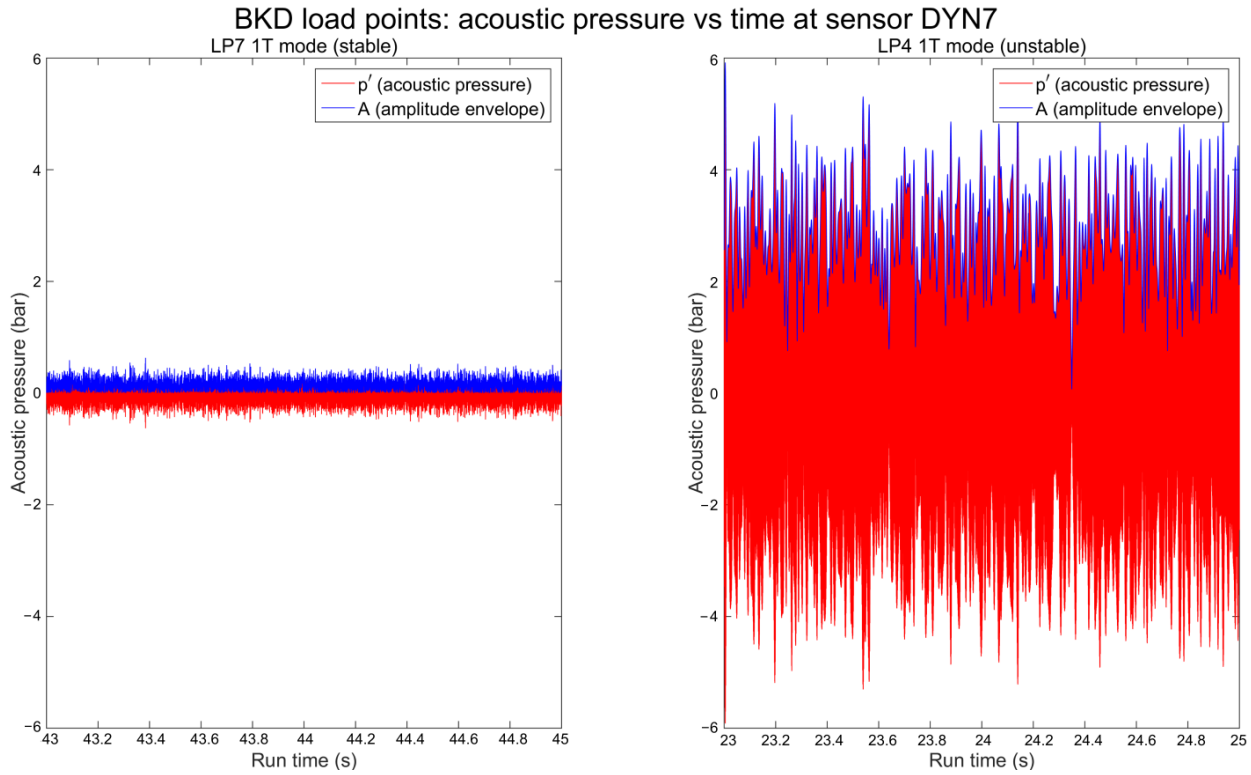

Figure 27: Acoustic pressure and amplitude envelope of the BKD load points LP7 (stable) and LP4 (unstable) vs run time.

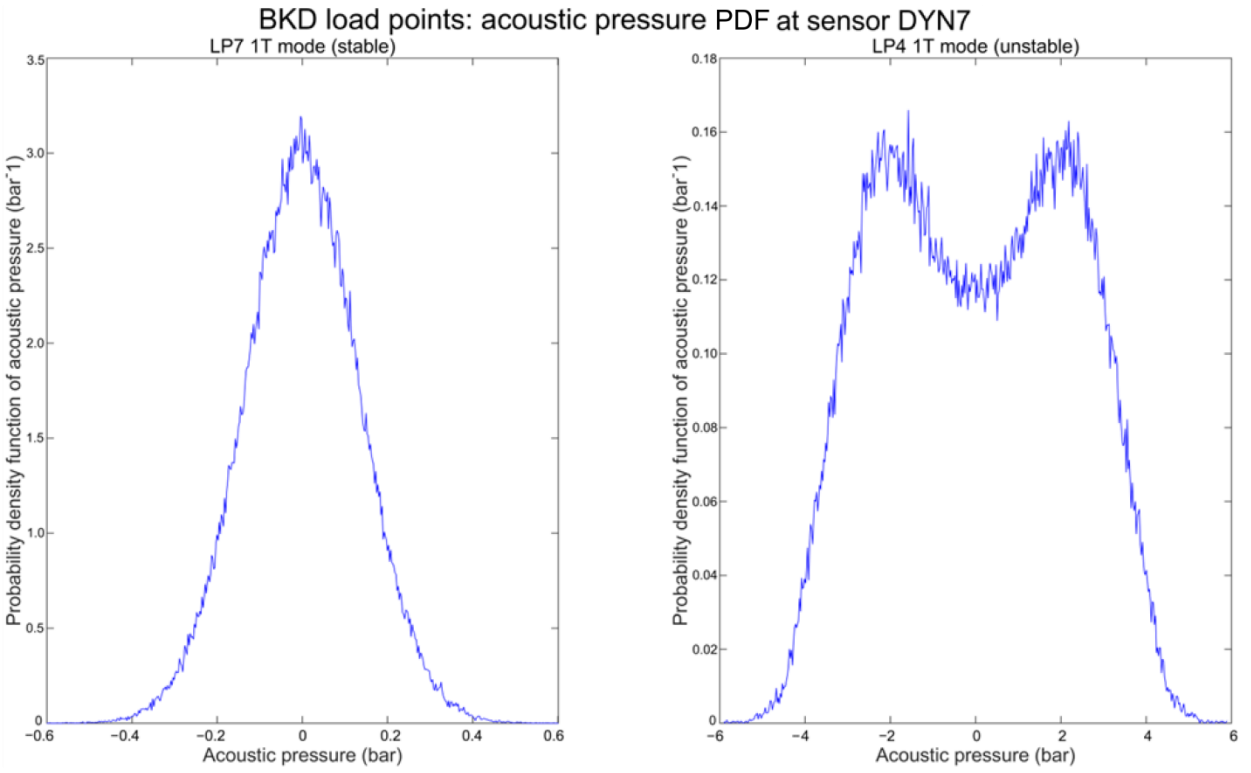

Figure 28: Acoustic pressure PDFs of the BKD load points LP7 (stable) and LP4 (unstable).

5.2 Stable Load Point LP7 1T Reconstruction and Lorentzian Parameters

This section presents the reconstruction of the LP7 1T mode and its Lorentzian parameter extraction. The acoustic pressure PSD of the LP7 1T mode (averaged over the 8 sensors) is shown in Figure 29. The LP7 1T mode can be decomposed into two orthogonal standing modes 'A' and 'B' as described in section 2.4.8. Using the reference for θ in Figure 25, the A mode has pressure anti-nodes at θ = 0°, 180° while the B mode has pressure anti-nodes at θ = ±90°. Good comparisons between the reconstructed and experimental signals are shown in Figure 30 and Figure 31 for the sensors DYN7 and DYN1 respectively. Lorentzian fits to the PSDs of the reconstructed A and B modes can be used to extract their growth rates and noise intensites. Such fits are plotted in Figure 32 and Figure 33 which show the A and B mode PSDs for DYN7 and DYN1 where either the A or B mode is dominant. Good agreements can be observed between these PSDs and their Lorentzian profiles, provided that the Lorentzian fitting avoids neighbouring modes. These Lorentzian profiles indicate that the LP7 1T mode is indeed linearly stable since a Lorentzian profile occurs only at linear conditions.

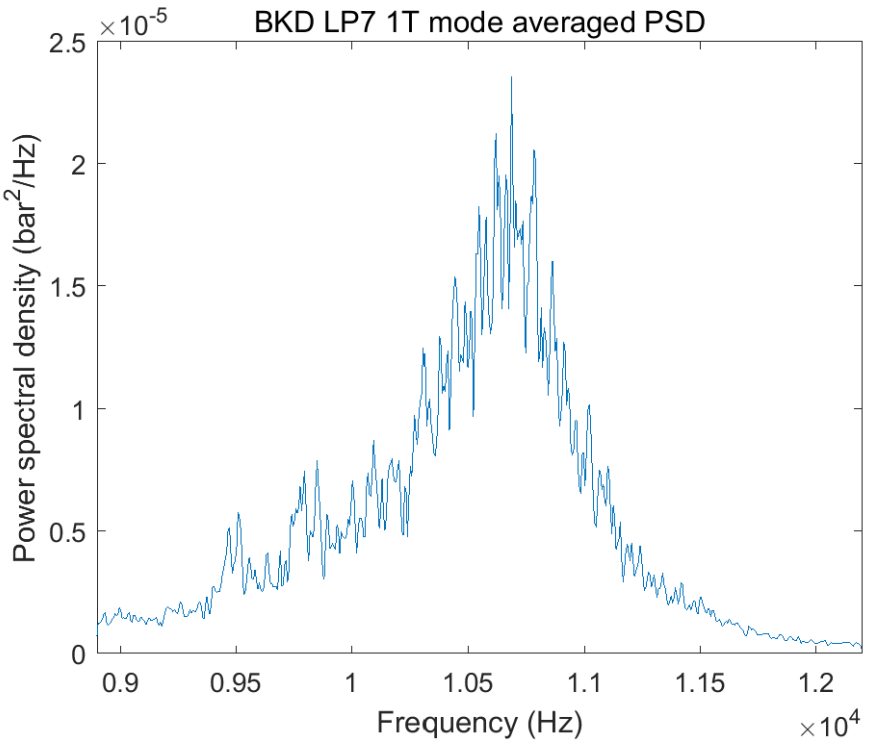

Figure 29: BKD LP7 1T mode PSD consisting of an average of the 8 PSDs for each sensor.

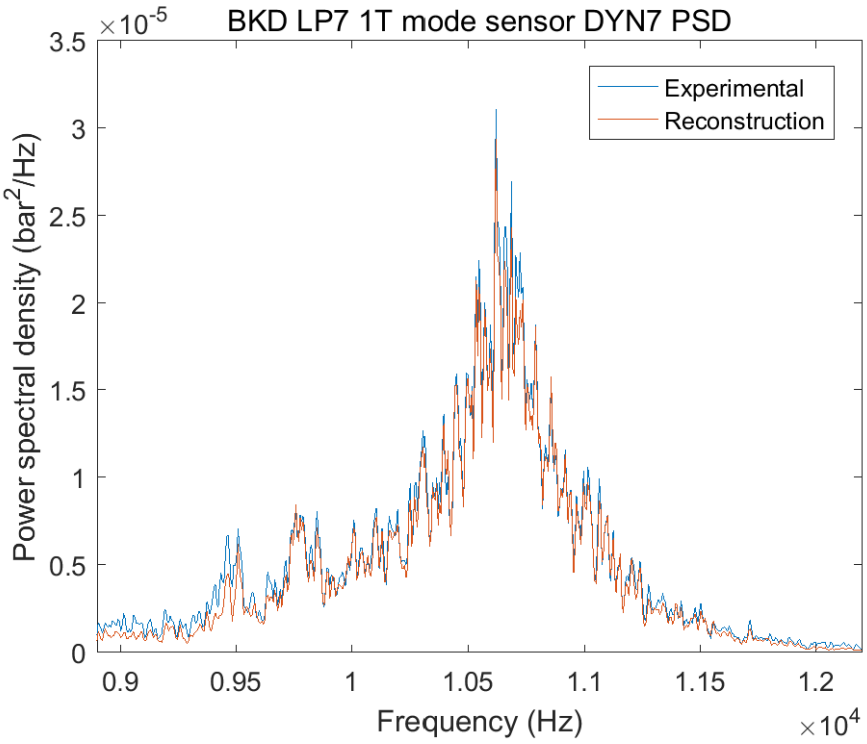

Figure 30: BKD LP7 1T mode experimental and reconstructed PSDs for the DYN7 sensor.

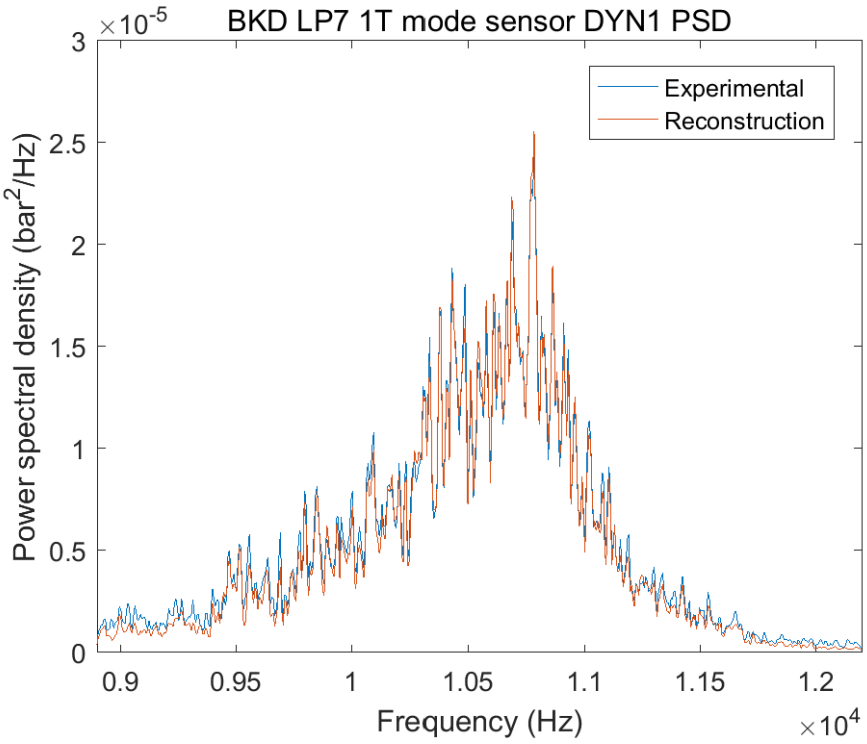

Figure 31: BKD LP7 1T mode experimental and reconstructed PSDs for the DYN1 sensor.

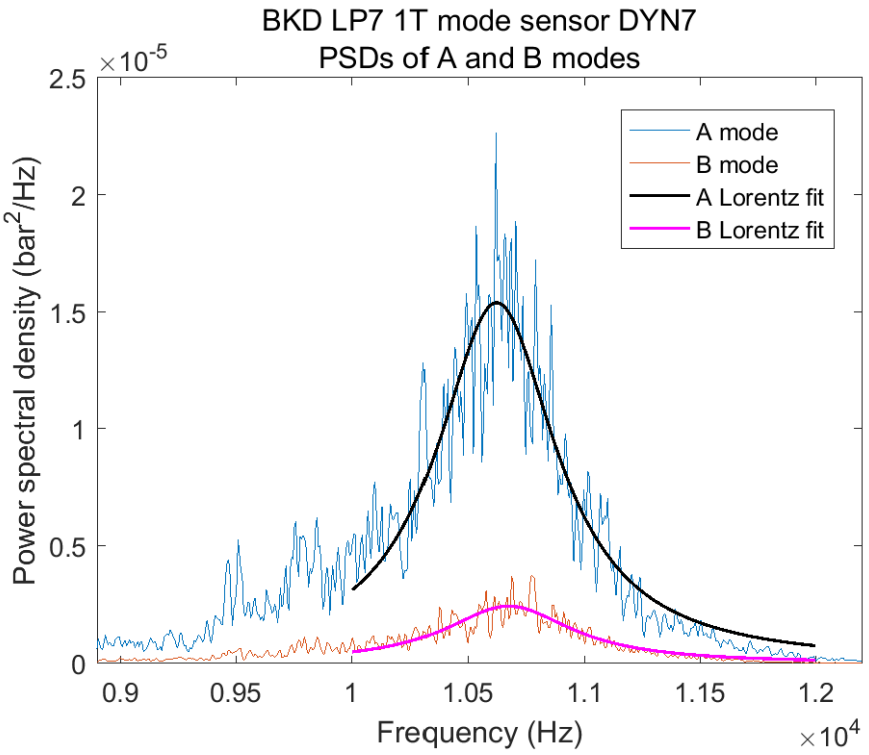

Figure 32: BKD LP7 1T mode reconstructed PSDs of the A and B modes for the DYN 7 sensor. Optimised Lorentzian fits to these PSDs are plotted in thick lines.

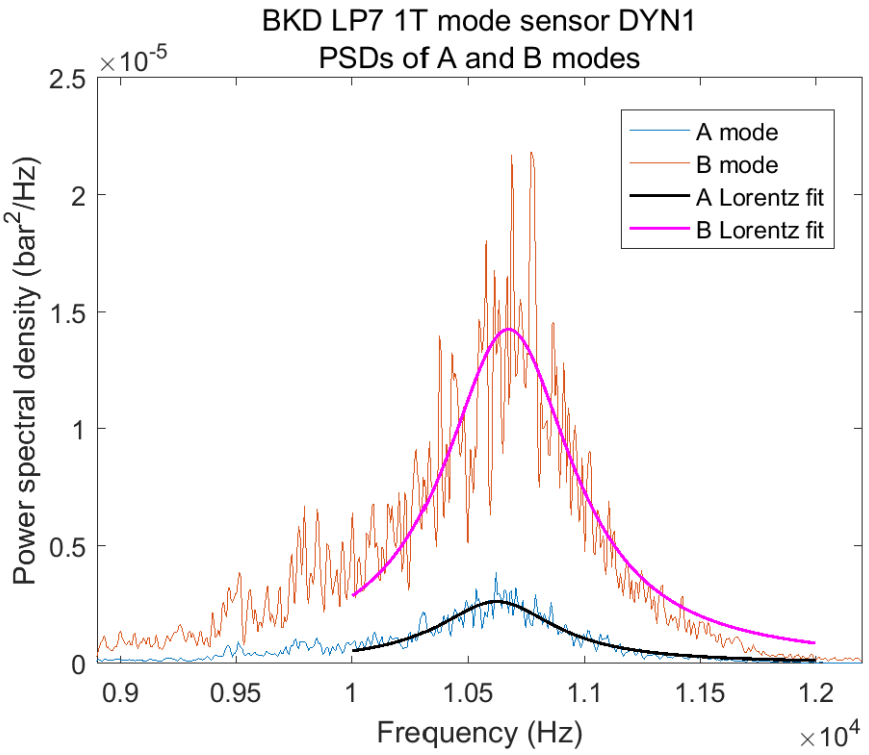

Figure 33: BKD LP7 1T mode reconstructed PSDs of the A and B modes for the DYN 1 sensor. Optimised Lorentzian fits to these PSDs are plotted in thick lines.

The growth rates and noise intensities for the A and B modes extracted with Lorentzian fitting are presented in Table 5, alongside the mean and maximum values of the A and B amplitude envelopes. The slightly higher mean amplitude for the A mode than the B mode can be attributed to ν_a being slightly higher (less net damping) than ν_b, while the higher maximum amplitude the B mode can be attributed to Γ_b being slightly higher than Γ_a. Therefore the Lorentzian fits yield parameter trends in agreement with direct observations of the reconstructed signals. The peak frequencies of the Lorentzian profiles for the A and B modes are 10623 Hz and 10674 Hz respectively; an average of 10649 Hz provides a value for $\omega_0/2\pi$ which completes the Lorentzian parameter extraction.

Table 5: BKD LP7 1T mode amplitude envelope mean and maximum, and Lorentzian growth rates and noise intensities for the reconstructed A and B modes.

LP7 1T amplitude envelope mean and max.				Lorentzian growth rate and noise intensity			
A mode		B mode		A mode		B mode	
mean(A) (bar)	max(A) (bar)	mean(B) (bar)	max(B) (bar)	$\nu_a/2\pi$ (Hz)	Γ_a (10^{11} bar^2 s^{-3})	$\nu_b/2\pi$ (Hz)	Γ_b (10^{11} bar^2 s^{-3})
0.162	0.555	0.159	0.611	-314	6.25	-338	6.75

5.3 Stable Load Point LP7 1T A Mode Analysis

An analysis of the A mode (and also the B mode in the next section) of the LP7 1T mode was carried out using the same compound extrapolation function that was applied to BKH data analyses. Since BKD data analyses require the use of the 2D Fokker-Planck coefficients method, the two-dimensionality of the Fokker-Planck coefficient computations must be considered.

The approach taken in this work is to focus on variations of the primary variable, i.e. A in the evaluation of the A mode drift coefficient $\mathcal{F}_{\mathrm{A}}(\mathrm{A}, \breve{\mathrm{B}})$, while keeping the secondary variable constant (in this case $\breve{\mathrm{B}}$). The modal value of the secondary variable, or values close to it, provide the most data for transition moment computations. Hence the evaluation of 2D Fokker-Planck coefficients in this work consists of fixing the secondary variable based on statistical occurence, and then analysing signals with primary variable variations. This approach allows a detailed observation of the signals and of the extrapolation fits used.

The analysis of the LP7 1T A mode encompasses seven amplitudes A1 to A7 which were selected from an amplitude histogram of 20 bins as shown in Figure 34. The secondary variable $\breve{\mathrm{B}}$ was fixed at the modal value (or those of its neighbours) of a 20 bin histogram as depicted in Figure 35. It is noted that the coarser the bin resolution the greater the amount of data that is available for a fixed secondary variable. Hence, a relatively coarse resolution of 20 bins is an appropriate baseline resolution for applying the 2D Fokker-Planck coefficients method to LP7. For the LP7 1T A mode, increasing the resolution from this baseline of 20 bins was found to decrease signal quality as shown in Appendix D. Hence, the detailed analyses of the LP7 1T A mode presented in this section have an amplitude resolution of 20 bins.

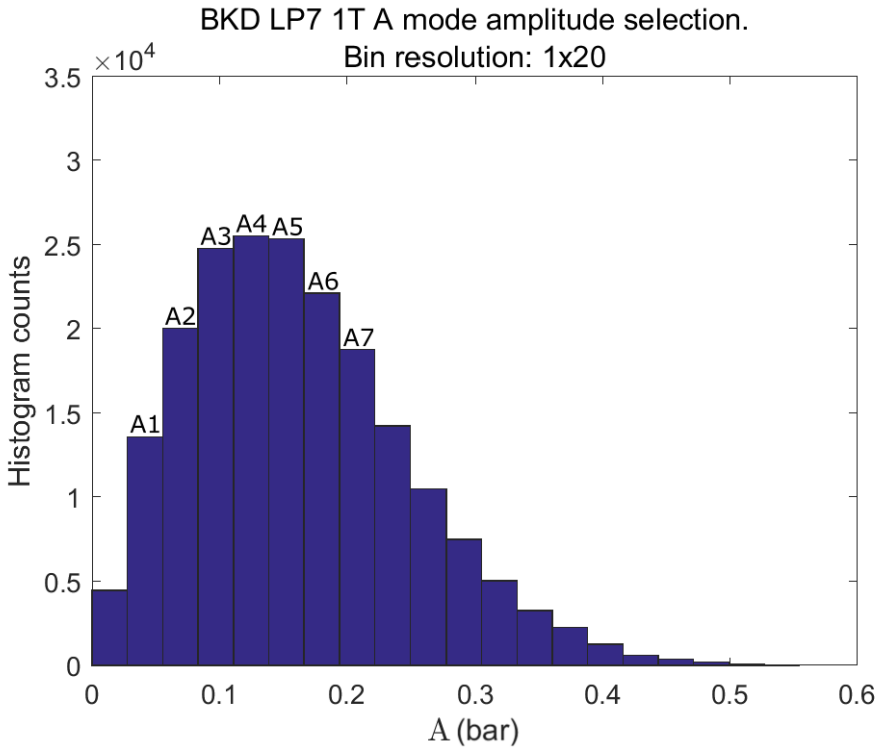

Figure 34: BKD LP7 1T A mode selection of seven amplitudes A1 to A7.

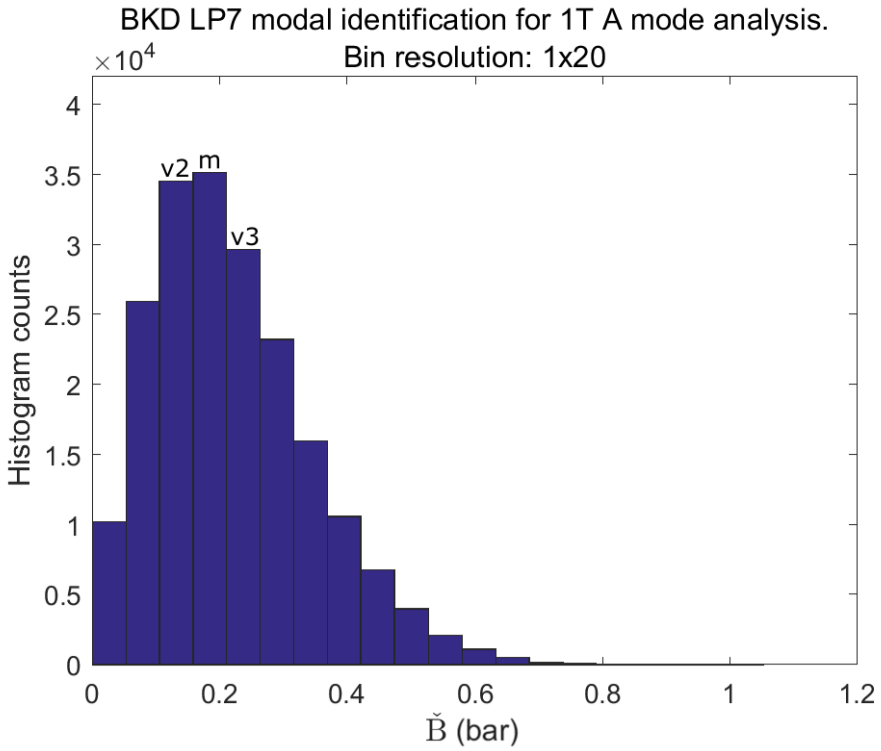

Figure 35: BKD LP7 modal identification for 1T A mode analysis. The 'm' indicates the modal peak, 'v2' and 'v3' are its neighbours (versions 2 and 3).

The 2D Fokker-Planck coefficients method was applied to the LP7 1T A mode using the three different fixed values for $\check{B}$: 'm' (mode), 'v2' (version 2) and 'v3' (version 3) as labelled in Figure 35. The transition moments and corresponding extrapolations for these three cases are shown in Figures 36, 37 and 38. For all cases, the time series used for transition moment computations was band-pass filtered from 8900 to 12200 Hz, i.e. the entire frequency range shown in Figure 32 and Figure 33. This filtering thus includes the neighbouring mode disturbances on the left of the 1T mode spectrum. Their inclusion in the analysis serves to check if weak disturbances in the modal spectrum are allowable in the use of the 2D Fokker-Planck coefficients method.

An initial guess of c = -800 s^{-1} was used for the extrapolation optimisations of all transition moment signals. A value of c = -550 s^{-1} was manually set for the $D_\tau^{(1)}$ A1 signal, and of c = -500 s^{-1} for the $D_\tau^{(1)}$ A2, A3 and A4 signals since for these signals the optimisation procedure did not yield good extrapolation fits (the extrapolation optimisation algorithm was not sufficiently robust). The c values used for all signals are documented in Appendix D. It is noted that these relatively high c values with respect to those used for BKH data also correspond to a shorter τ length for extrapolation fitting of 0.004 s compared to BKH's 0.025 s. Good agreements can be observed between the expected Fokker-Planck coefficients based on Lorentzian parameters and the extrapolated limits to zero of 2D transition moments.

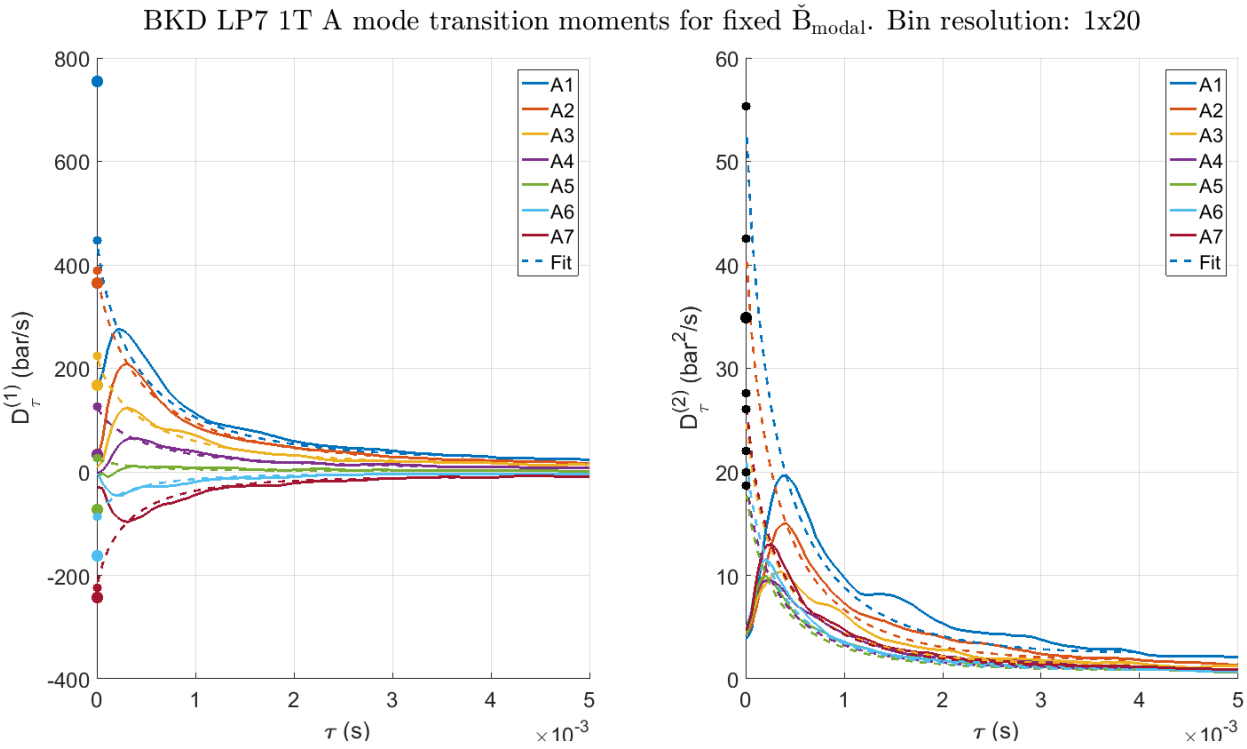

Figure 36: BKD LP7 1T A mode first $D_\tau^{(1)}$ (plot on left) and second $D_\tau^{(2)}$ (plot on right) transition moment computations for seven amplitudes of A for the modal value of $\check{B}$. The limits to zero of the $D_\tau^{(1)}$ and $D_\tau^{(2)}$ computations, given by the extrapolation fits shown in dotted lines, correspond to the drift and diffusion coefficients respectively. Small dots on the y-axes are the limits to zero obtained with extrapolations, while big dots are the expected values based on parameters found with Lorentzian fitting.

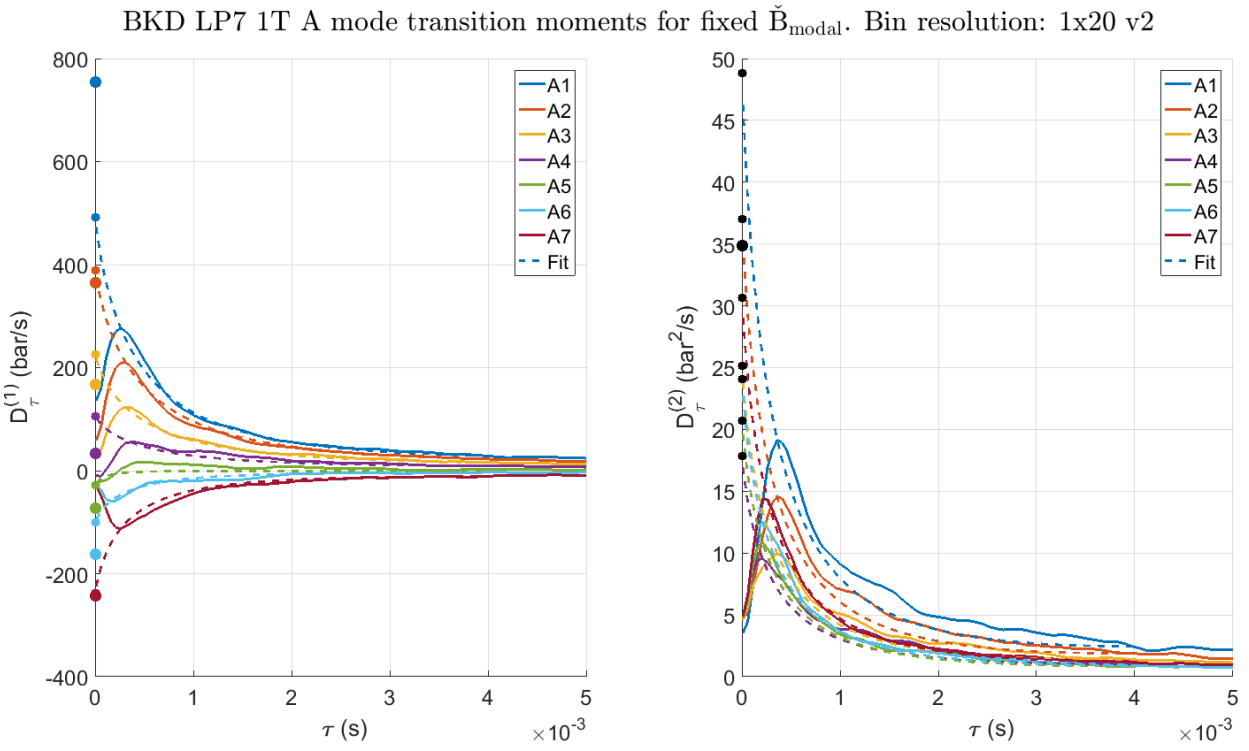

Figure 37: BKD LP7 1T A mode first $D_\tau^{(1)}$ (plot on left) and second $D_\tau^{(2)}$ (plot on right) transition moment computations for seven amplitudes of A for the modal (v2) value of $\check{B}$. The limits to zero of the $D_\tau^{(1)}$ and $D_\tau^{(2)}$ computations, given by the extrapolation fits shown in dotted lines, correspond to the drift and diffusion coefficients respectively. Small dots on the y-axes are the limits to zero obtained with extrapolations, while big dots are the expected values based on parameters found with Lorentzian fitting.

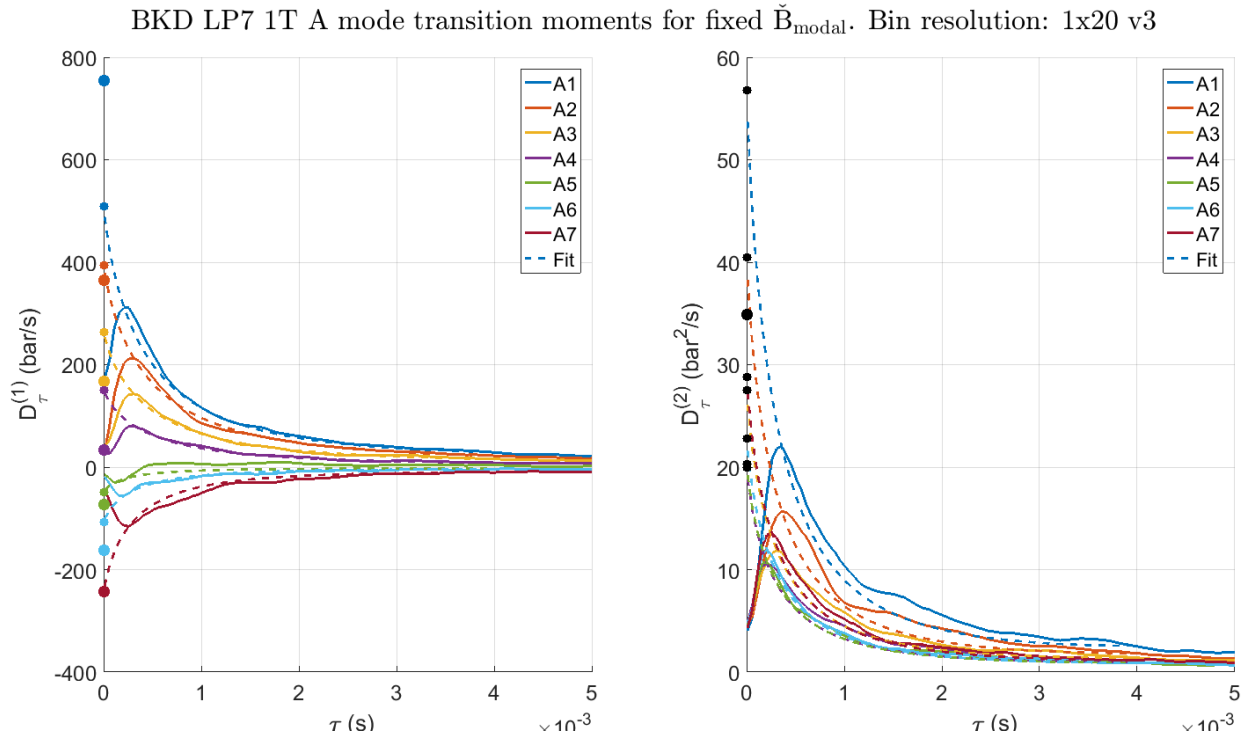

Figure 38: BKD LP7 1T A mode first $D_\tau^{(1)}$ (plot on left) and second $D_\tau^{(2)}$ (plot on right) transition moment computations for seven amplitudes of A for the modal (v3) value of $\check{B}$. The limits to zero of the $D_\tau^{(1)}$ and $D_\tau^{(2)}$ computations, given by the extrapolation fits shown in dotted lines, correspond to the drift and diffusion coefficients respectively. Small dots on the y-axes are the limits to zero obtained with extrapolations, while big dots are the expected values based on parameters found with Lorentzian fitting.

A robust optimisation algorithm (independent of initial guesses) was implemented to extract the growth rate and noise intensity of the LP7 1T A mode for each of the three considered cases using the 2D Fokker-Planck coefficients method.

Two approaches were used in the application of this method. The first consists of finding the noise intensity from the diffusion coefficient $\frac{\Gamma_a}{4{\omega_0}^2}$ by averaging the limits to zero of second transition moment signals, and finding the growth rate by optimising the analytical expression for the drift coefficient $\mathcal{F}_A(A, \breve{B})$ to fit the limits to zero of first transition moment signals. This is the same approach that was used for BKH data analyses. A second approach consists of finding both the noise intensity and growth rate from the analytical expression for $\mathcal{F}_A(A, \breve{B})$ which features both parameters. These two variants of the Fokker-Planck coefficients method can be abbreviated as F.P.C 1 and F.P.C 2 respectively.

The parameter extraction results of applying F.P.C. 1 and 2 to the LP7 1T A mode are presented in Table 6 and compared with the Lorentzian parameters. From Table 6 it can be seen that the errors are systematic, with the 2D F.P.C. 1 method providing more accurate results than the 2D F.P.C. 2 method. For all cases, the latter underpredicts the noise intensity and the net damping rate more than the former. The best result is obtained with the 2D F.P.C. 1 method for the v3 case, with an error of 22% for ν_a and 11% for Γ_a. Since v3 is the least statistically rich case, error variances cannot be explained by data deficits. The 2D Fokker-Planck coefficients method therefore yielded accurate parameters for the LP7 1T A mode, but with systematic errors of unclear origin.

Table 6: BKD LP7 1T A mode parameter extraction results from applying Lorentzian fits and two variants of the 2D Fokker-Planck coefficients method.

Method	LP7 1T A mode analysis cases and parameters					
	$\breve{B}$ fixed to modal value		$\breve{B}$ fixed to v2		$\breve{B}$ fixed to v3	
	$\nu_a/2\pi$ (Hz)	Γ_a (10^{11} bar^2 s^{-3})	$\nu_a/2\pi$ (Hz)	Γ_a (10^{11} bar^2 s^{-3})	$\nu_a/2\pi$ (Hz)	Γ_a (10^{11} bar^2 s^{-3})
Lorentzian	-314	6.25	-314	6.25	-314	6.25
2D F.P.C. 1	-228 [error: 27%]	5.45 [error: 13%]	-235 [error: 25%]	5.20 [error: 17%]	-245 [error: 22%]	5.55 [error: 11%]
2D F.P.C. 2	-183 [error: 42%]	4.50 [error: 28%]	-216 [error: 31%]	4.82 [error: 23%]	-220 [error: 30%]	5.00 [error: 20%]

5.4 Stable Load Point LP7 1T B Mode Analysis

The LP7 1T B mode analysis was carried out similarly to the 1T A mode analysis. The main difference is that a higher amplitude resolution of 2x20 bins was used since, unlike for the A mode, signal quality is not reduced at twice the baseline resolution. A resolution analysis of the LP7 1T B mode transition moments is presented in Appendix D. Seven amplitude values B1 to B7 were selected from the baseline resolution as shown in Figure 39. Detailed analyses were undertaken using these amplitudes at a 2x20 bin resolution with $\breve{A}$ fixed at its modal or neighbouring values as shown in Figure 40.

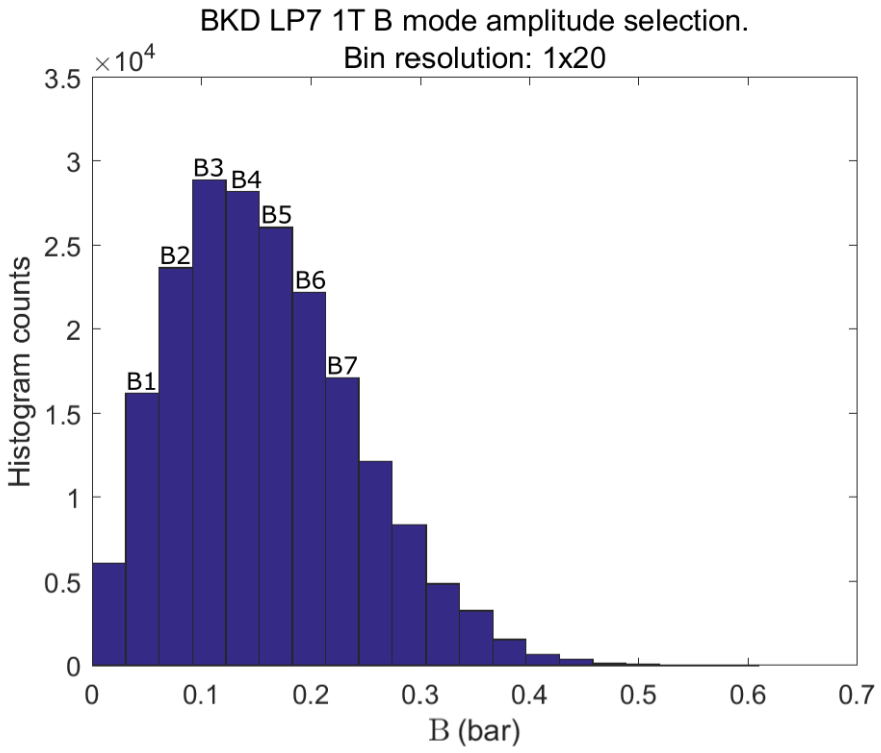

Figure 39: BKD LP7 1T B mode selection of seven amplitudes B1 to B7.

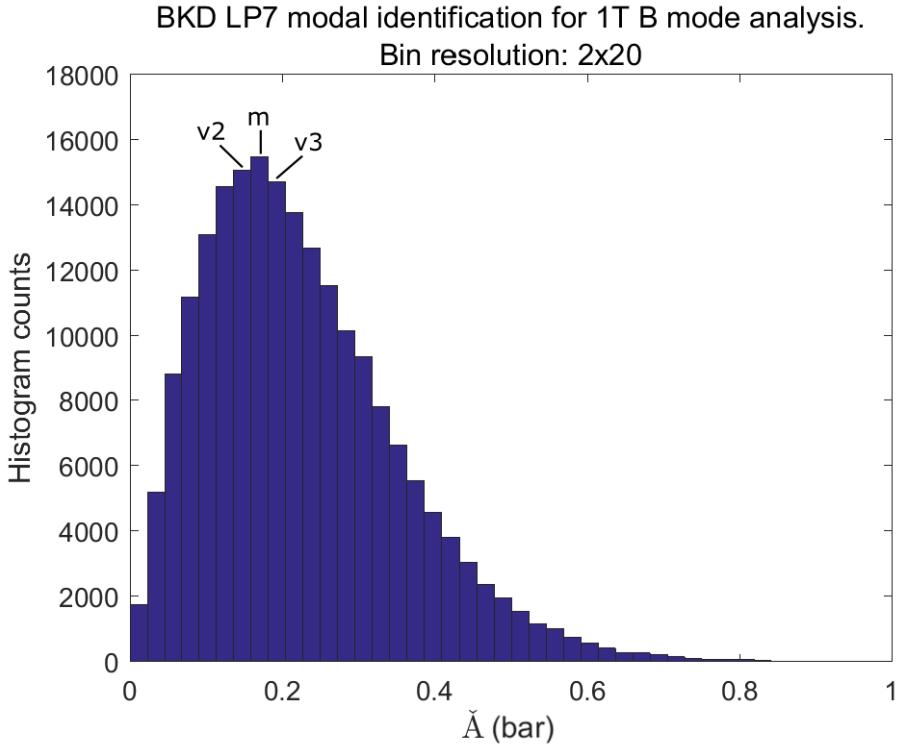

Figure 40: BKD LP7 modal identification for 1T B mode analysis. The 'm' indicates the modal peak, 'v2' and 'v3' are its neighbours (versions 2 and 3).

2D transition moments were computed for the LP7 1T B mode using the three different fixed values for $\breve{A}$: 'm' (mode) and 'v2' (version 2) and 'v3' (version 3) as labelled in Figure 40. The quality of first transition moment signals is reduced as the $\breve{A}$ value is changed from the mode to v2 to v3. This is appreciable in Figures 41, 42 and 43 which depict the transition moments for the three cases. Interestingly, this is an opposite trend to that observed for the LP7 1T A mode analysis.

The 2D Fokker-Planck coefficients method was only applied to the highest quality case shown in Figure 41. An initial guess of c = -800 s^{-1} was used for the extrapolation optimisations of all transition moment signals. This resulted in good extrapolation fits for all signals. In Figure 41 it can be seen that limit to zero extrapolations of the transition moments using compound exponential functions agree well with expected Fokker-Planck coefficient values based on Lorentzian parameters.

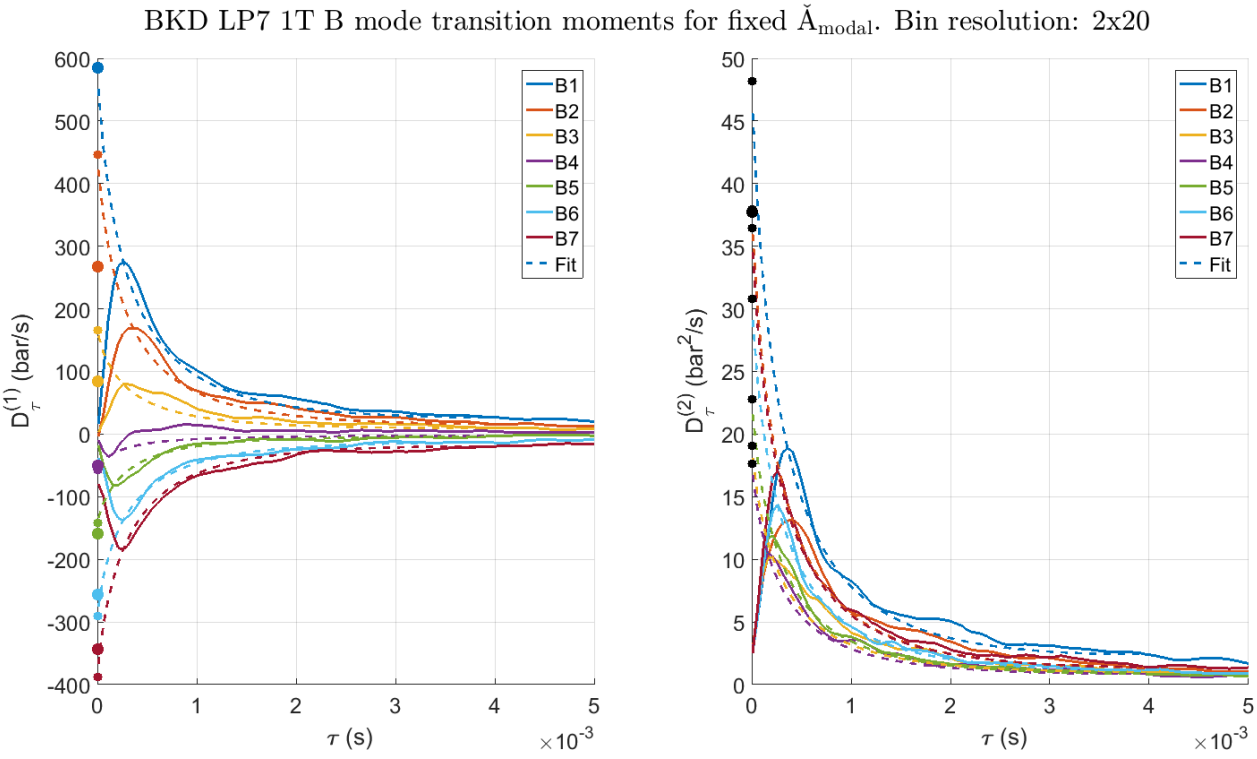

Figure 41: BKD LP7 1T B mode first $D_\tau^{(1)}$ (plot on left) and second $D_\tau^{(2)}$ (plot on right) transition moment computations for seven amplitudes of B for the modal value of $\breve{A}$. The limits to zero of the $D_\tau^{(1)}$ and $D_\tau^{(2)}$ computations, given by the extrapolation fits shown in dotted lines, correspond to the drift and diffusion coefficients respectively. Small dots on the y-axes are the limits to zero obtained with extrapolations, while big dots are the expected values based on parameters found with Lorentzian fitting.

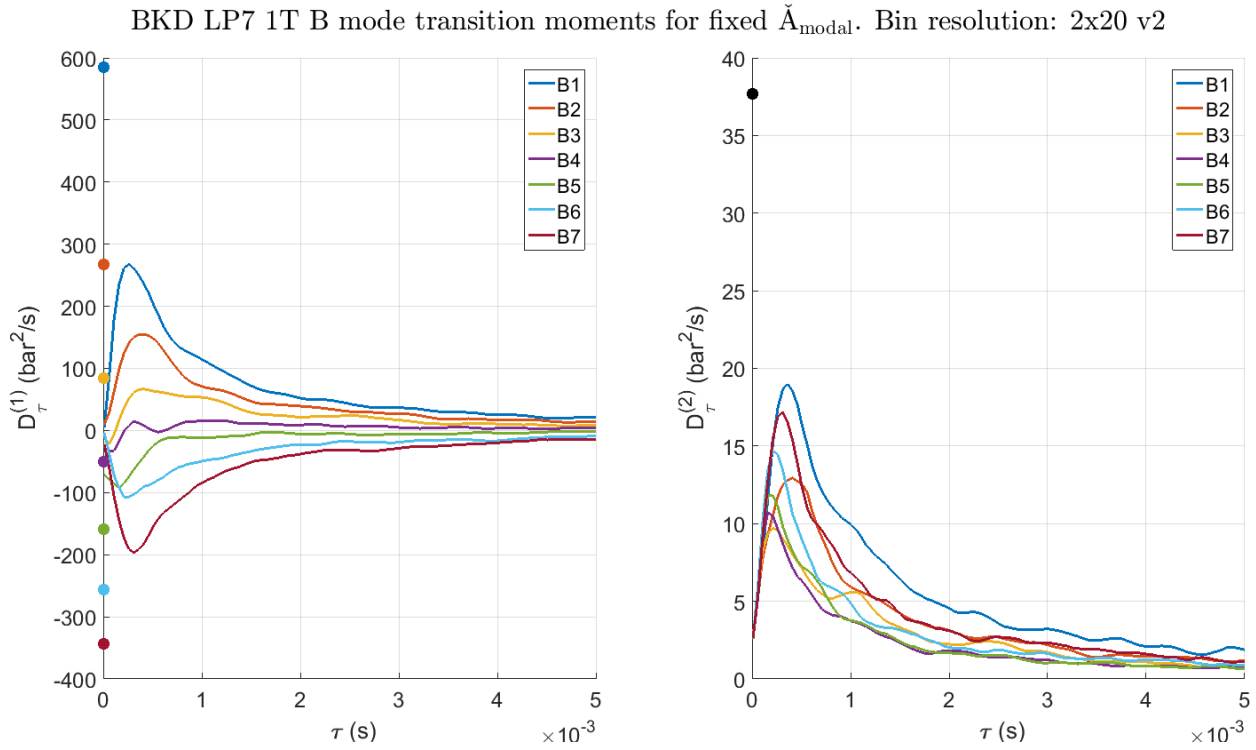

Figure 42: BKD LP7 1T B mode first $D_\tau^{(1)}$ (plot on left) and second $D_\tau^{(2)}$ (plot on right) transition moment computations for seven amplitudes of B for the modal (v2) value of Ă. The limits to zero of the $D_\tau^{(1)}$ and $D_\tau^{(2)}$ computations correspond to the drift and diffusion coefficients respectively. Small dots on the y-axes are the limits to zero obtained with extrapolations, while big dots are the expected values based on parameters found with Lorentzian fitting.

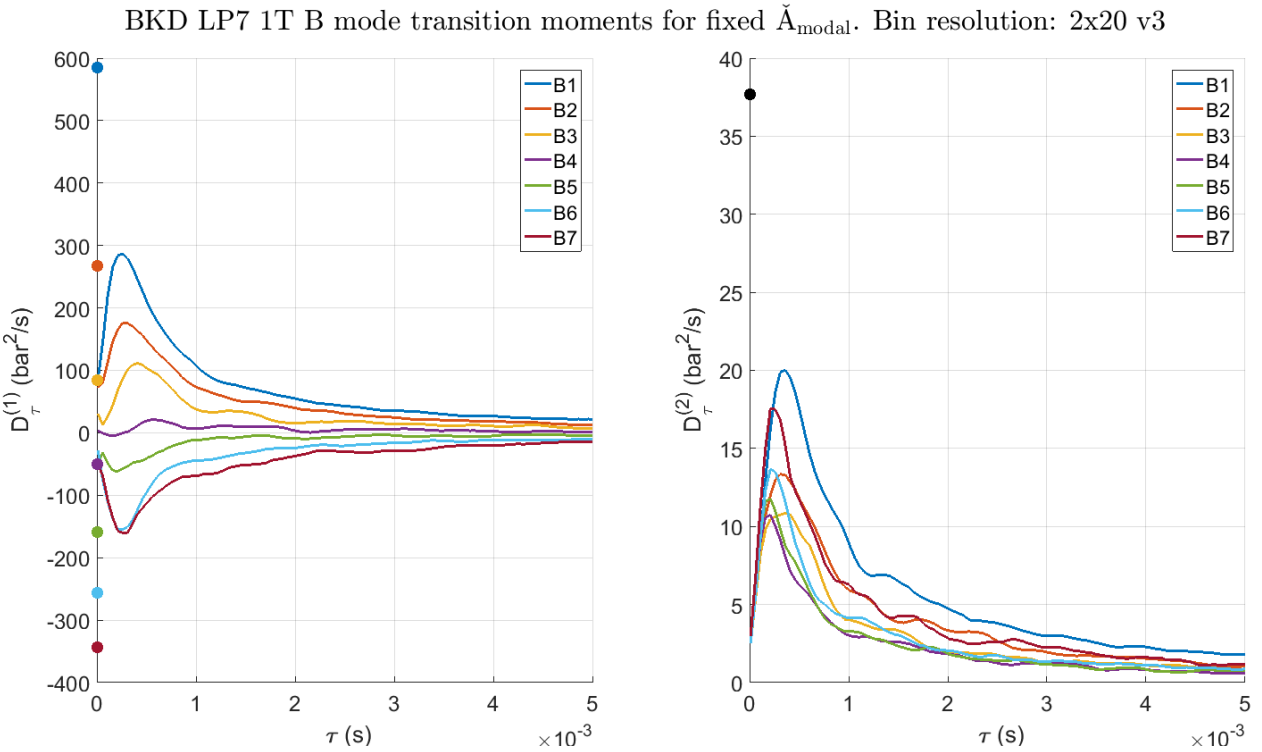

Figure 43: BKD LP7 1T B mode first $D_\tau^{(1)}$ (plot on left) and second $D_\tau^{(2)}$ (plot on right) transition moment computations for seven amplitudes of B for the modal (v3) value of Ă. The limits to zero of the $D_\tau^{(1)}$ and $D_\tau^{(2)}$ computations correspond to the drift and diffusion coefficients respectively. Small dots on the y-axes are the limits to zero obtained with extrapolations, while big dots are the expected values based on parameters found with Lorentzian fitting.

A robust optimisation algorithm (independent of initial guesses) was implemented to extract the growth rate and noise intensity of the LP7 1T B mode for the considered case using the 2D Fokker-Planck coefficients method. Results in good agreement with Lorentzian paremeters were obtained with both the 2D F.P.C. 1 and 2D F.P.C. 1 methods, as shown in Table 7. The 2D F.P.C. 1 method underpredicts the net damping rate and the noise intensity, while the 2D F.P.C. 2 method overpredicts both parameters with lesser errors. This constrasts the trend observed in the LP7 1T A mode analysis where the 2D F.P.C. 2 method undepredicted parameter values to a greater extent than the 2D F.P.C. 1 method. Hence the 2D Fokker-Planck coefficients method yielded accurate parameters for the LP7 1T B mode, albeit with error trends inconsistent with those obseved in the LP7 1T A mode analysis.

Table 7: BKD LP7 1T B mode parameter extraction results from applying Lorentzian fits and two variants of the 2D Fokker-Planck coefficients method.

Method	LP7 1T B mode analysis case and parameters	
	$\breve{\mathbf{B}}$ fixed to modal value	
	$\nu_b/2\pi$ (Hz)	Γ_b (10^{11} bar^2 s^{-3})
Lorentzian	-338	6.75
2D F.P.C. 1	-283 [error: 16%]	5.45 [error: 19%]
2D F.P.C. 2	-364 [error: 8%]	7.70 [error: 14%]

5.5 Stable Load Point LP7 Simplified Model Analysis

This section analyses the applicability of the simplified 2D dynamical model to the LP7 1T mode. The simplified model assumes that $\kappa_a \approx \kappa_b$ and $\Gamma_a \approx \Gamma_b$, and that the phase difference ϕ is characterised by potential wells at $\phi = \pm\frac{\pi}{2}$. Since the LP7 1T mode is linearly stable, the effect of the non-linear condition $\kappa_a \approx \kappa_b$ is negligible. The condition $\Gamma_a \approx \Gamma_b$ was found to be true in the noise intensity results obtained using both Lorentzian and Fokker-Planck coefficients methods.

Phase difference accumulation at potential wells of $\phi = \pm\frac{\pi}{2}$ is the third assumption behind the 2D simplified model. However, since ϕ only appears in the non-linear terms of the 2D dynamical equations, its effect is negligible. A PDF of ϕ for the LP7 1T mode is shown in Figure 44, where it can be seen that the statistical distribution of ϕ is uniform. This indicates that there is no coupling between the 1T A and B modes. Their dynamics are independent such that any value of the phase difference between them is equally likely to occur. This observation supports the implications from the 2D dynamical equations that coupling between the A and B modes only occurs at non-linear conditions, and that the A and B modes are independent at linear amplitudes.

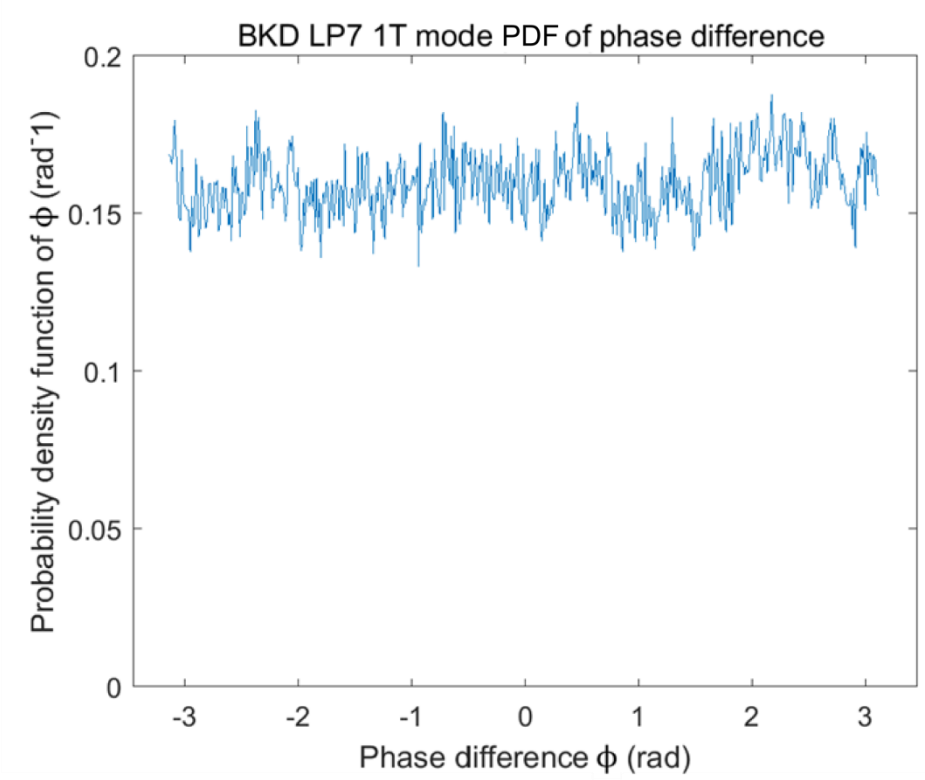

Figure 44: BKD LP7 1T mode PDF of phase difference between A and B modes.

If the non-linear terms of the 2D PDF equation (Eq. (42) in section 2.4.9) are removed, what is left is a superposition of the 1D amplitude PDF equation (Eq. (15) in section 2.4.5) for each of the A and B modes. A plot of the analytical 2D PDF using the linear terms of Eq. (42) with the parameters extracted from Lorentzian fitting is shown in Figure 45 alongside the experimental 2D PDF. A good match can be observed between the analytical and experimental PDFs; this is a strong indication that the assumed 2D linear dynamics are correct, and that $\Gamma_a \approx \Gamma_b$ is an appropriate simplification.

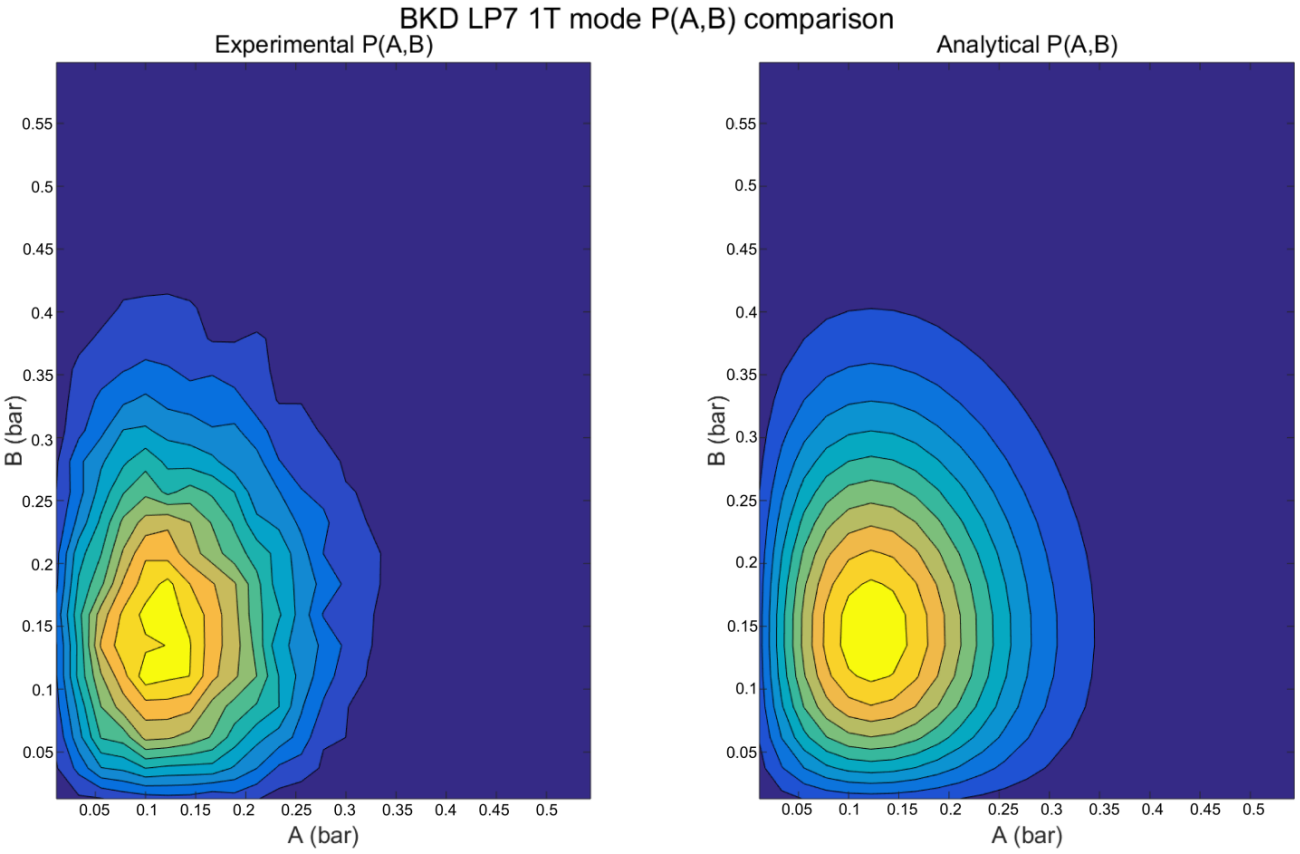

Figure 45: BKD LP7 1T mode comparison between the experimental and analytical $P(A, B)$. On the left, the experimental 2D PDF of the 1T mode amplitudes A and B. On the right, the analytical expectation based on the 2D Fokker Planck stationary PDF expression using parameters found with Lorentzian fitting. An amplitude resolution of 25 bins was used to make the contour plots, which consist of 12 contour levels where the maximum contour is 0.95 times the maximum experimental PDF value.

5.6 Unstable Load Point LP4 1T Frequency Analysis and Reconstruction

This section analyses the PSD of the LP4 1T mode to establish its modal frequency, and also presents its modal reconstruction results. The averaged PSD (over all 8 sensors) of the LP4 1T mode is shown in Figure 46. Two dominant peaks at 10257 Hz and 10262 Hz are present in this PSD which is taken over the entire load point run time (23 to 25 s). The two peaks can be attributed to a natural frequency shift of the 1T mode caused by small changes in operating conditions during the experimental run. This shift can be seen in the PSDs of Figure 47 and Figure 48 which are taken for two different time segments: 23 to 24 s and 24 s to 25 s respectively. Hence, the natural frequency $\omega_0/2\pi$ can be taken to be the average of the two peaks at 10260 Hz.

Comparisons between the experimental and the reconstructed PSDs at the DYN7 and DYN1 sensors are shown in Figure 49 and Figure 50 respectively. Good agreements between the experiment and reconstruction can be seen for both sensors, with a more precise agreement for DYN7 where the acoustic pressure signal is stronger.

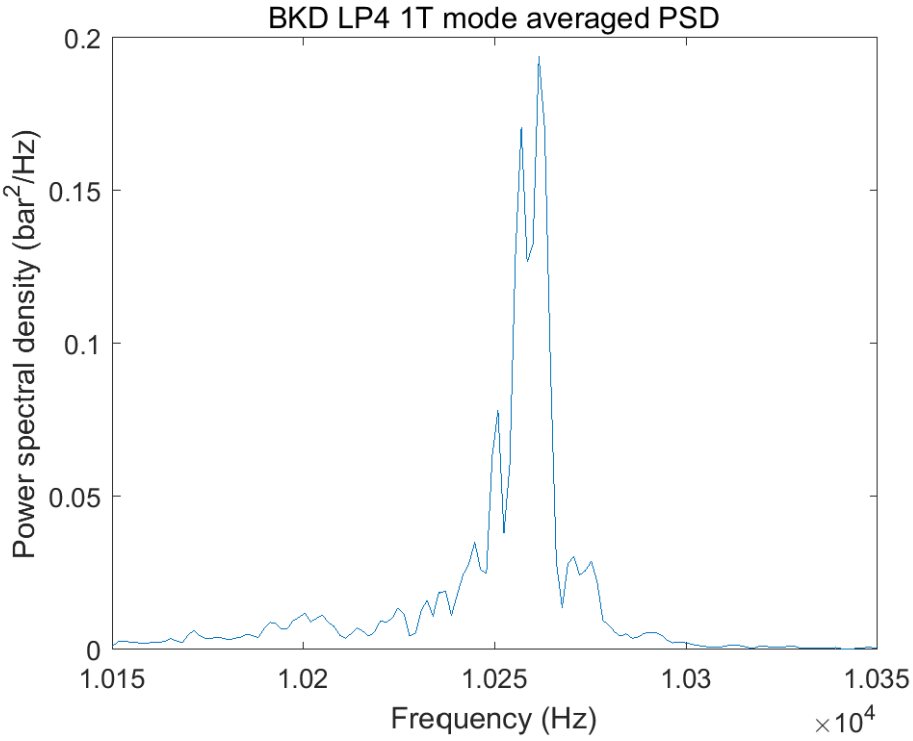

Figure 46: BKD LP4 1T mode averaged PSD for the entire run time (23 to 25 s).

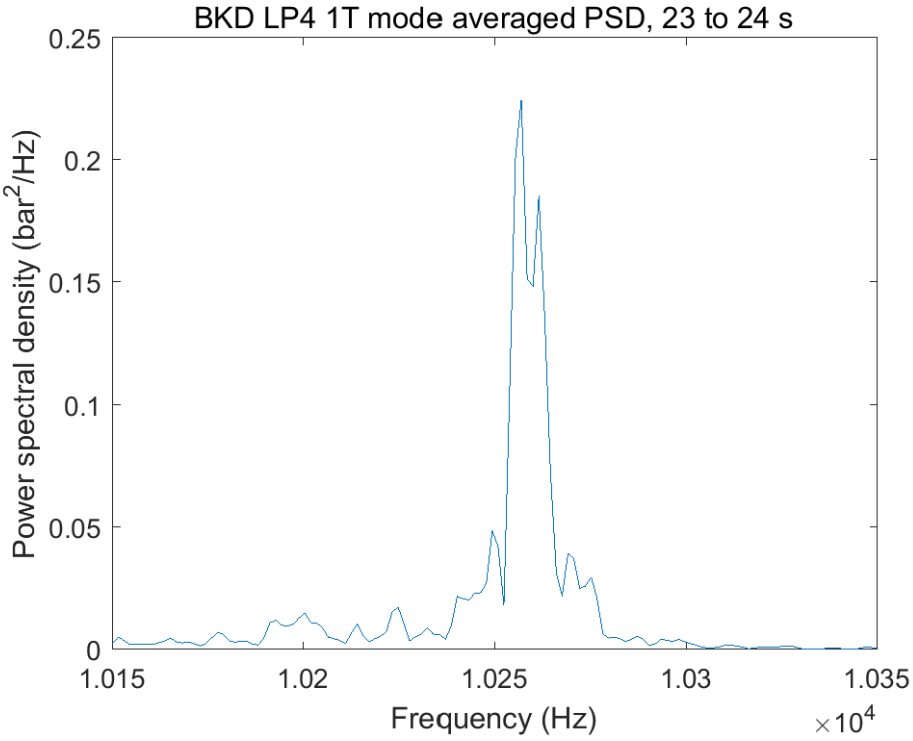

Figure 47: BKD LP4 1T mode averaged PSD for the 23 to 24 s run time segment.

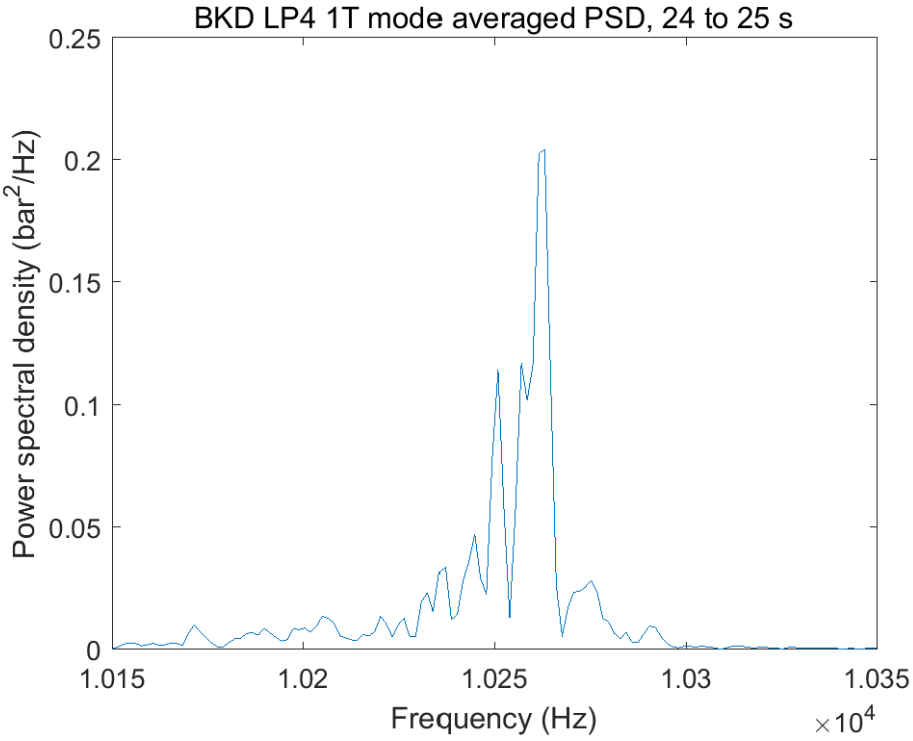

Figure 48: BKD LP4 1T mode averaged PSD for the 24 to 25 s run time segment.

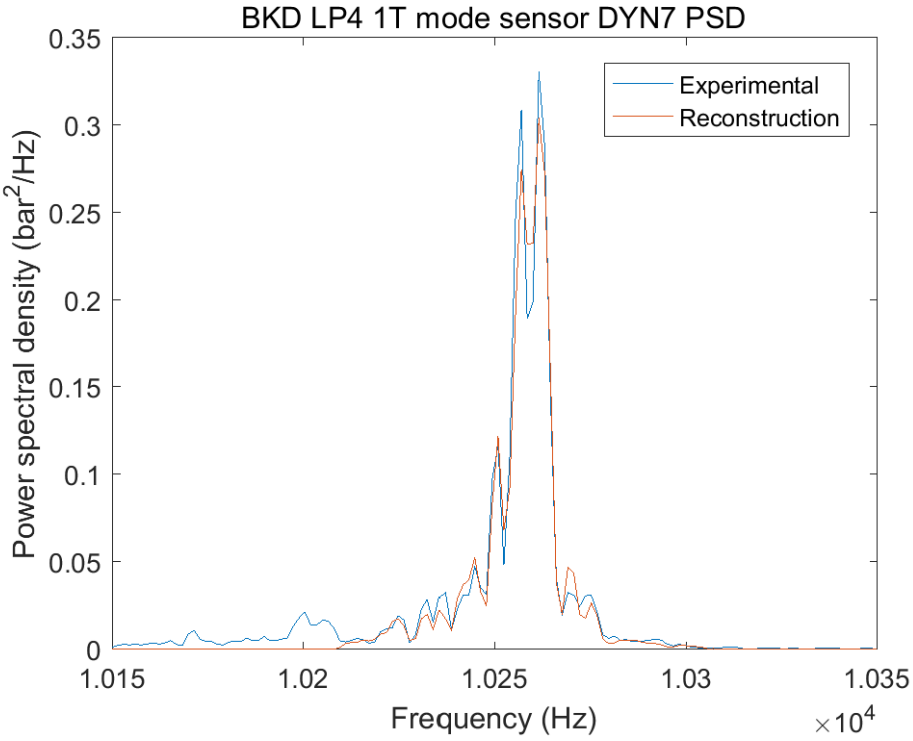

Figure 49: BKD LP4 1T mode experimental and reconstructed PSDs for the DYN7 sensor.

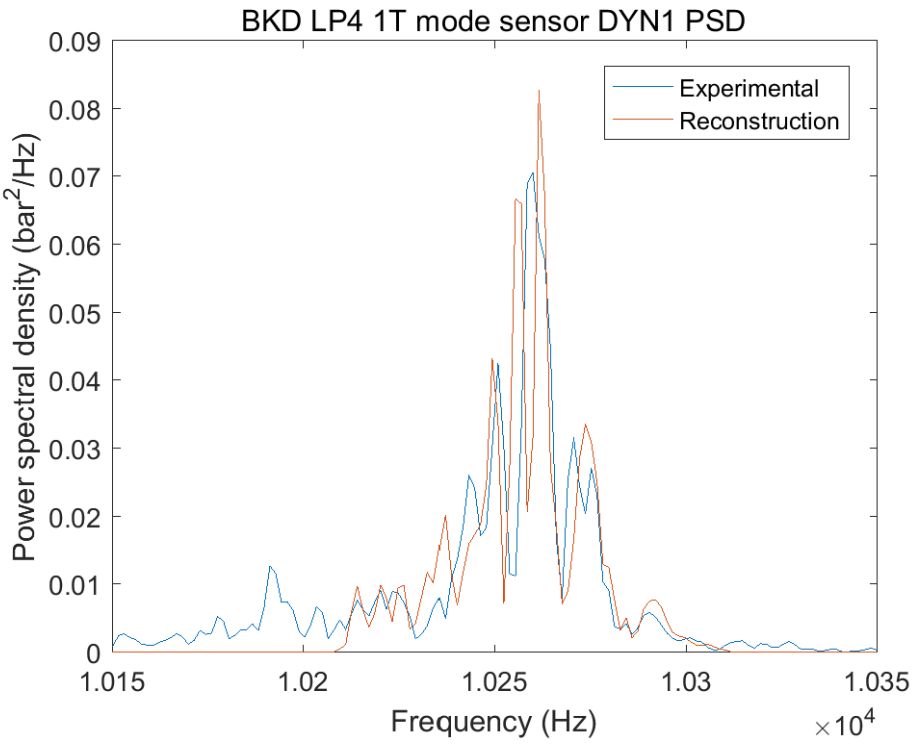

Figure 50: BKD LP4 1T mode experimental and reconstructed PSDs for the DYN1 sensor.

The reconstruction of the LP4 1T mode using two standing modes A and B provides an indication of the relative strength of instability at different 1T mode orientations. The mean and maximum values of the A and B amplitude envelopes are presented in Table 8. It can be seen that the LP4 1T A mode is significantly stronger than the B mode.

Table 8: BKD LP4 1T amplitude envelope mean and maximum values for the A and B modes.

LP4 1T amplitude envelope mean and maximum			
A mode		**B mode**	
mean(A) (bar)	**max(A) (bar)**	**mean(B) (bar)**	**max(B) (bar)**
3.00	4.75	1.23	3.09

5.7 Unstable Load Point LP4 Simplified Model Analysis

This section analyses the applicability of the simplified 2D dynamical model to the LP4 1T mode. The normalised phase difference potential $U(A, B, \phi) \times \frac{64}{3\kappa}$ given by Eq. (38) in section 2.4.9 is plotted vs ϕ in Figure 51 for the entire run time of the LP4 1T mode. Each dot in this plot represents a normalised phase potential for a given A, B and ϕ at a given point in time. The average of these potential values over the run time is -1.8 bar^2 . This is a weak negative value compared to potential well depths at $\phi = \pm\frac{\pi}{2}$ of approximately -20 bar^2, which suggests that ϕ is accumulating in potential wells only weakly. The PDF of ϕ over the run time is shown in Figure 52 at a high resolution. A thin peak close to $\phi = -\frac{\pi}{2}$ is the modal peak, but the overall PDF shape is bimodal with mound centres shifted from the theoretical potential wells at $\phi = \pm\frac{\pi}{2}$. The higher

occurrence and lesser shift at $\phi = -\frac{\pi}{2}$ compared to $\phi = +\frac{\pi}{2}$ may be explained by deeper potential wells at $\phi = -\frac{\pi}{2}$ as shown in Figure 51. The applicability of the 2D simplified model to the LP4 1T mode is ultimately unclear, and requires further investigation than that in this work.

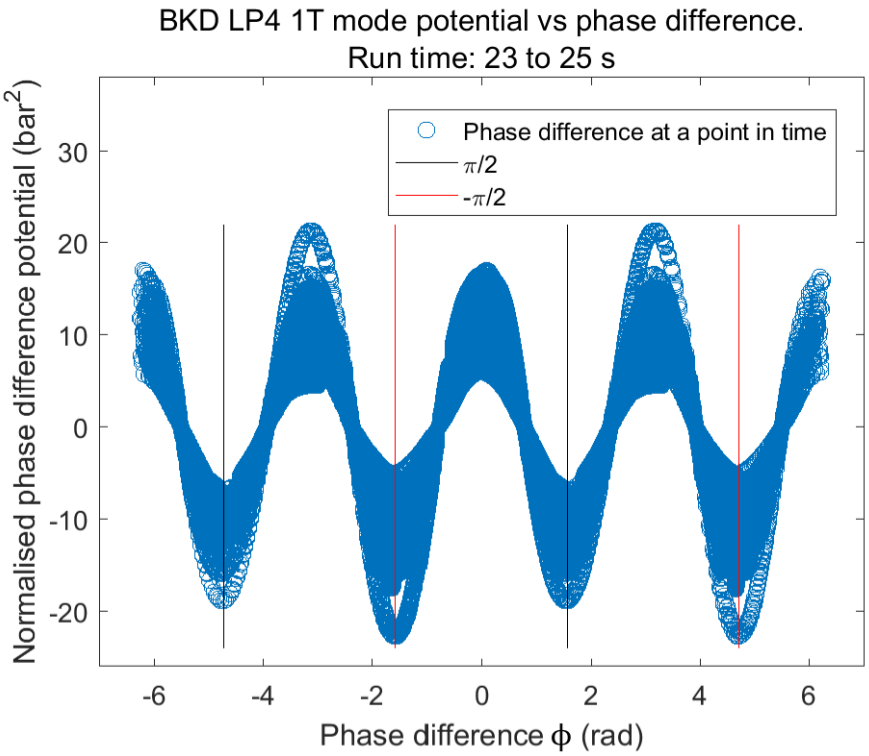

Figure 51: BKD LP4 1T mode normalised phase difference potential for entire run time (23 to 25 s).

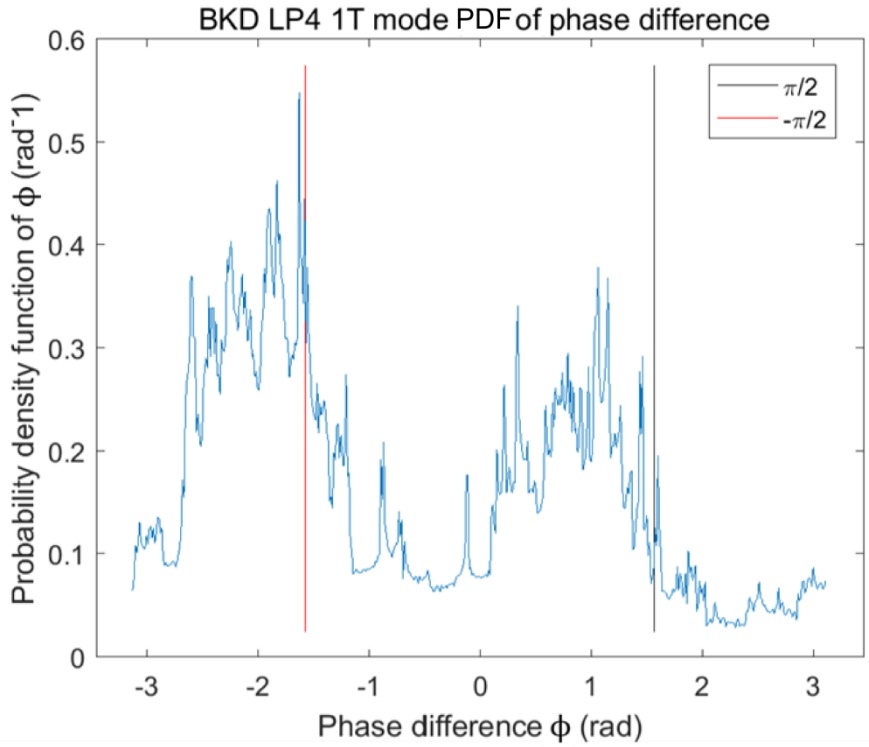

Figure 52: BKD LP4 1T mode PDF of phase difference between A and B modes.

5.8 Summary of Results for Test Case 2

The growth rate and noise intensity of the linearly stable LP7 1T A and B modes were successfully extracted using the 2D Fokker-Planck coefficients method. The 2D linear dynamics assumed were found to be precise, however the applicability of the 2D simplified model to the unstable LP4 1T mode was found to be unclear. Good quality Lorentzian fits which match the PSDs of the reconstructed LP7 1T A and B modes were used to find their growth rates and noise intensities. These were also extracted with two variants of the 2D Fokker-Planck coefficients method consisting of either using the second transition moment to estimate the noise intensity (2D F.P.C. 1 method) or of using the first transition moment to estimate both the noise intensity and the growth rate (2D F.P.C. 2 method). Generally, the 2D Fokker-Planck coefficients underpredicted the net damping rate and the noise intensity with respect to the Lorentzian parameters. The best result for the LP7 1T A mode has an error of 22% for $\nu_a$and 11% for Γ_a using the 2D F.P.C. 1 method, while the best result for the 1T B mode has an error of 8% for ν_b and 14% for Γ_b using the 2D F.P.C. 2 method. The compound exponential extrapolation used in BKH data analyses was applied to these BKD LP7 analyses with similarly good results.

A uniform PDF was observed for the phase difference ϕ between the LP7 1T A and B modes which indicates their dynamical independence in the absence of non-linear coupling. A good agreement was found between the linear terms of the simplified model 2D PDF with Lorentzian parameters and the experimental 2D PDF of the LP7 1T mode. This provides a strong indication that the assumed linear dynamics for the LP7 1T mode are correct, and $\Gamma_a \approx \Gamma_b$ is an appropriate simplification.

Strong directionality was observed in the LP4 1T mode instability, where the A mode is clearly stronger than the B mode. This highlights the importance of allowing for different growth rate values, ν_a and ν_b, in the dynamical modelling. A higher growth rate for the A mode than for the B mode is the only way of accounting for the stronger A mode signal provided that the non-linearity coefficient is not strongly directional.

A bimodal PDF was observed for the phase difference ϕ between the LP4 1T A and B modes. This is indicative of significant coupling between the A and B modes at non-linear conditions, as would be predicted by the assumed 2D dynamical equations. The theoretical phase difference potential has wells at $\phi = \pm\frac{\pi}{2}$ which help to explain the bimodal ϕ PDF. Deeper potential wells at $\phi = -\frac{\pi}{2}$ than at $\phi = +\frac{\pi}{2}$ may account for the dominance of the former in the bimodal ϕ PDF. However, the modal mounds in this PDF are not precisely centred at $\phi = \pm\frac{\pi}{2}$, instead a shift to lower phase difference values can be observed in Figure 52. Hence the applicability of the 2D simplified model, which assumes characteristic phase differences at $\phi = \pm\frac{\pi}{2}$, to the LP4 1T mode is unclear and requires further investigation. Nonetheless, the concept of non-linear A and B mode coupling at characteristic phase differences of $\phi = \pm\frac{\pi}{2}$ helps to explain the phase difference statistics observed for the unstable LP4 1T mode.

6. Conclusions

The aim of extracting key parameters governing thermo-acoustic behaviour in rocket combustors using stochastic signal processing techniques was achieved for four stable rectangular combustor load points and one stable cylindrical combustor load point. Significant progress was made analysing an unstable cylindrical combustor load point. Results supported important dynamical concepts assumed in the formulation of the techniques. The techniques are based on modelling statistics of the acoustic pressure time series of a combustor mode using the Fokker-Planck equation. Two formulations of the stochastic techniques were tested on rocket combustor data. A 1D dynamics formulation was applied to data from a rectangular combustor with standing acoustic modes, and a 2D dynamics formulation was applied to data from a cylindrical combustor with rotational acoustic modes.

The 1D Fokker-Planck coefficients method was applied to the first longitudinal (1L) and first transverse (1T) modes of BKH, a rectangular rocket combustor that is naturally stable. Four different BKH load points were considered with variations in the chamber pressure and the injection velocity ratio (VR). The Fokker-Planck coefficients method yielded growth rates and noise intensities for the 1L and 1T modes of these load points with acceptable random errors for all cases. The best result was obtained for the BKH 1L mode with a supercritical chamber pressure of 60 bar and a low VR ratio of 7.6. In this case, small errors of 0.3% for the growth rate ν and 4.9% for the noise intensity Γ were found with respect to the parameters obtained with Lorentzian fitting. The good agreements found between Lorentzian fitting and the 1D Fokker-Planck coefficients method to extract parameters from BKH load points are a validation of the latter method, at linear conditions, for the first time in rocket engine literature.

The 2D Fokker-Planck coefficients method was applied to a stable first tangential (1T) mode of BKD; a cylindrical rocket combustor with an unstable 1T mode at some load points. The stable 1T mode of the considered load point; dubbed 'LP7', was decomposed into two standing modes 'A' and 'B' with orthogonal orientations to each other. The superposition of these two standing modes, with a phase difference ϕ between them to describe their temporal relationship, represent the BKD 1T mode which can exhibit rotational behaviour in the cylindrical combustion chamber. Lorentzian fits to the acoustic pressure PSDs of the LP7 1T A and B modes were used to find their growth rates $\nu_a$and ν_b and noise intensities Γ_a and Γ_b.

The 2D Fokker-Planck coefficients method was applied to the LP7 1T A and B modes to extract ν_a, ν_b, Γ_a and Γ_b from the A and B acoustic pressure time series. Data analyses for each mode focused on primary variable variations by fixing the secondary variable in the 2D coefficient expressions. This allowed a detailed observation of transition moment signals. A compound exponential function not found in existing literature, given by Eq. (42) in section 4.3, was used for extrapolating the limit to zero of transition moments for both the BKH analyses and this BKD LP7 analysis with good results. The best result was obtained for the LP7 1T B mode where the 2D Fokker-Planck coefficients method yielded ν_b and Γ_b values with errors of 8% and 14% compared to Lorentzian parameters. Since Noiray and Schuermans (PRSA 2013) do not present a linear case

with Lorentzian fitting or an unstable case with active control, the linear LP7 1T mode analysis presented in this work is the first experimental validation of the 2D Fokker-Planck coefficients method in general literature.

The BKH and BKD linear load point analyses investigated the effects of data processing parameters on the Fokker-Planck coefficients method. A band-pass filter analysis was carried out for the BKH LH2 1L mode, where significant errors in the estimated parameters arose when the band-pass width was reduced symmetrically around the peak frequency to $\pm 2 \times \nu$. At this band-pass width, an error of 13% was found for the growth rate and of 32% for the noise intensity compared to Lorentzian parameters. Asymmetric expansion of the band-pass width did not improve results. Hence a symmetric band-pass width of at least $\pm 2 \times \nu$ is considered appropriate.

The BKD LP7 1T A and B modes featured weak neighbouring modes outside the $\pm 2 \times \nu$ region of their Lorentzian profiles. These were included in the LP7 1T mode analysis, and accurate parameter values were obtained with the 2D Fokker-Planck coefficients method. This suggests that weak neighbouring modes removed from the peak frequency do not greatly impact transition moment computations.

The BKD LP7 1T mode analysis also showed that 2D transition moment signals are sensitive to the amplitude bin resolution. Relatively coarse resolutions of 20 and 40 bins were used for the LP7 1T A and B mode analyses, compared to the 100 bins used for 1D BKH analyses. High resolutions reduce signal quality for the LP7 transition moments, presumably due to a reduction in statistical counts which are already diminished for the analysis of a 2D data set compared to a 1D set. Band-pass filtering and amplitude bin resolution were therefore shown to affect results significantly in this work.

The A and B mode decomposition of an unstable BKD 1T mode for a load point 'LP4' provided important insights into BKD 1T mode instability through a comparison with the LP7 1T mode. The LP7 1T mode has a uniform PDF for the phase difference ϕ between the A and B modes which can be attributed to their dynamical independence at linear conditions. An analytical 2D PDF for the A and B amplitudes, which assumes non-coupled linear dynamics and that $\Gamma_a \approx \Gamma_b$, well matches the LP7 experimental 2D PDF if Lorentzian parameters are fed into it (with an averaging of Γ_a and Γ_b). This is a strong indication that the dynamics of the LP7 1T A and B modes are linear, driven by isotropic stochastic forcing, and independent from each other. Unlike the stable LP7 1T mode, the unstable LP4 1T mode has a bimodal ϕ PDF which indicates non-linear coupling between the A and B modes.

From the assumed 2D dynamics, the phase difference has potential wells at $\phi = \pm\frac{\pi}{2}$ where ϕ would theoretically accumulate. While a thin peak in the LP4 1T mode ϕ PDF, shown in Figure 52, closely corresponds to $\phi = -\frac{\pi}{2}$, the mound centres in the bimodal PDF are shifted away from $\phi = \pm\frac{\pi}{2}$. These shifts could be partly caused by strong stochastic forcing that does not allow ϕ to settle in potential wells. A lesser shift and greater occurrence at $\phi = -\frac{\pi}{2}$ than at $\phi = +\frac{\pi}{2}$ can be

explained by deeper potential wells at $\phi = -\frac{\pi}{2}$ as shown in Figure 51. Hence the observed ϕ statistics for the unstable LP4 1T mode can be explained with the assumed 2D dynamics, which account for non-linear coupling between the A and B modes.

If phase difference dynamics are simplified to two characteristic values at $\phi = \pm\frac{\pi}{2}$, a simplified 2D dynamical model can be obtained and an analytical 2D PDF derived with the additional assumptions that $\Gamma_a \approx \Gamma_b$ and $\kappa_a \approx \kappa_b$. An analytical 2D PDF would be useful in an unstable case analysis. It would generate a simulated 2D PDF, fed with parameters obtained using the 2D Fokker-Planck coefficients method, which can be compared to the experimental 2D PDF to assess the accuracy of the estimated parameters. However, since the PDF of ϕ of the LP4 1T mode shows phase shifts away from $\phi = \pm\frac{\pi}{2}$ the applicability of the 2D simplified model to an unstable BKD 1T mode is unclear and requires further investigation.

The A and B mode decomposition of the LP4 1T mode provided insight into the directionality of BKD 1T mode instability. The LP4 1T A mode was found to be significantly stronger than the B mode, with a mean amplitude envelope 2.4 times that of the B mode. This directionality demonstrates the need of having different A and B growth rates in the assumed dynamics, that is $\nu_a \neq \nu_b$ generally.

In summary, the three objectives set out in section 0 in pursuit of the aim of this work; to extract key parameters governing thermo-acoustic behaviour in rocket combustors using stochastic signal processing techniques, were achieved. The 1D Fokker-Planck coefficients method was applied to the stable 1L and 1T modes of multiple BKH load points. The extracted growth rates and noise intensities compared well with Lorentzian fitting results. Similarly, the 2D Fokker-Planck coefficients method was applied to a stable BKD 1T mode with parameter extraction results in good agreement with those from Lorentzian fitting. These BKH and BKD linear load point analyses fulfilled objectives 1 and 2 as set out in section 0. While the 2D Fokker-Planck coefficients method was not applied to an unstable BKD 1T mode in this work, significant analyses were carried out for the unstable LP4 1T mode which support underlying concepts in the assumed 2D dynamics. A bimodal PDF for the phase difference ϕ between the A and B modes was observed for the LP4 1T mode, which can be explained using a theoretical ϕ potential which has potential wells at $\phi = \pm\frac{\pi}{2}$ based on the assumed dynamics. The bimodal ϕ PDF of the unstable LP4 1T mode constrasts the uniform ϕ PDF of the stable LP7 1T mode, which supports the assumption that coupling between the A and B modes only occurs at non-linear amplitudes. This phase difference analysis of the unstable LP4 1T mode fulfilled objective 3 as set out in section 0. Therefore, the three main objectives of this work were achieved. These established the applicability of the Fokker-Planck coefficients parameter extraction method to stable rocket combustor load points, and provided positive indications of the method's applicability to rocket combustion instability.

7. Future Work

Future work to further fulfill the aim of extracting parameters from time series data using stochastic signal processing techniques should focus on non-linear BKD data analyses.

Firstly, the discrepancy in the bimodal PDF of the phase difference ϕ between the unstable BKD LP4 1T A and B modes from expected accumulations at $\phi = \pm\frac{\pi}{2}$ should be addressed. If phase difference dynamics are simplified to two characteristic values at $\phi = \pm\frac{\pi}{2}$, a simplified 2D dynamical model can be obtained and an analytical 2D PDF derived with the additional assumptions that $\Gamma_a \approx \Gamma_b$ and $\kappa_a \approx \kappa_b$. An analytical 2D PDF would be useful in an unstable case analysis. It would generate a simulated 2D PDF, fed with parameters obtained using the 2D Fokker-Planck coefficients method, which can be compared to the experimental 2D PDF to assess the accuracy of the estimated parameters. However, since the PDF of ϕ of the LP4 1T mode shows phase shifts away from $\phi = \pm\frac{\pi}{2}$ the applicability of the 2D simplified model to an unstable BKD 1T mode is unclear and requires further investigation.

A future step would be to apply the 2D Fokker-Planck coefficients method to the unstable BKD LP4 1T mode. Since non-linear results cannot be checked with a Lorentzian fit, synthetic signals representing instability would provide a valuable test of non-linear parameter extractions where the correct answers are known.

Synthetic signals could be generated with a Simulink model of the assumed 2D dynamics. This would also allow the simulation of a 2D PDF using non-simplified dynamics. For analyses of unstable BKD data, the experimental 2D PDF could be compared to a numerical 2D PDF generated with Simulink, and to an analytical 2D PDF based on simplified dynamics. This would also serve as an assessment of the applicability of the 2D simplified model to an unstable BKD 1T mode. Therefore, while significant outcomes have been achieved in this work, there is a clear and important body of future work to be carried out for non-linear conditions, where the stochastic signal processing techniques are of practical utility.

Appendix A

This appendix is comprised of two sections A1 and A2 which provide details on Lorentzian profile theory and noise intensity theory respectively.

A1 - Lorentzian Profile Theory

This section presents the theory behind the use of Lorentzian fits for parameter extraction from experimental PSDs. This consists of the approximation of the natural frequency ω_0 using the experimental peak frequency, and the approximation of Eq. (3) in section 2.4.1 with the Lorentzian profile of Eq. (4).

The natural frequency of a system is the frequency at which it oscillates without damping or driving. For a damped-driven harmonic oscillator with time-dependent variable $x(t)$ driven by a sinusoidal driving force $f_{dr}\cos(\omega t)$ the dynamics are given by Eq. (A1):

$$\frac{d^2x(t)}{dt^2} + 2\zeta\omega_o \frac{dx(t)}{dt} + \omega_o{}^2\, x(t) = f_{dr}\cos(\omega t) \tag{A1}$$

where ω_o is the natural frequency, ω is the driving frequency and ζ is the damping ratio. In the case of the thermo-acoustic dynamics of Eq. (1), $\zeta = -\nu/\omega_o$ where ν is the growth rate (with a negative value for linearly stable dynamics).

The resonant frequency, which is the peak frequency in a white noise driven spectrum, of the dynamics in Eq. (A1) is given by Eq. (A2):

$$\omega_{res} = \omega_o\sqrt{1-2\zeta^2} \tag{A2}$$

where ω_{res} is the resonance frequency.

Hence for $\nu << \omega_o$ the damping ratio ζ is sufficiently small such that $\omega_{res} \cong \omega_o$.

The response of the system in Eq. (A1) to forcing is given by Eq. (A3) and Eq. (A4).

$$x(t) = A_x\cos(\omega t - \varphi) \tag{A3}$$

where A_x is the amplitude response and φ is the phase.

$$A_x = \frac{f_{dr}}{\sqrt{(\omega_o{}^2 - \omega^2)^2 + 4\nu^2\omega^2}} \tag{A4}$$

The expression for $A_x{}^2$ (since the PSD in Eq. (3) consists of squaring the signal) can be approximated by a Lorentzian equation as written in Eq. (A5).

$$A_x{}^2 = \frac{f_{dr}{}^2}{(\omega_o{}^2 - \omega^2)^2 + 4\nu^2\omega^2} \cong M\frac{\nu^2}{(\omega_0 - \omega)^2 + \nu^2} \tag{A5}$$

where M is the maximum of the Lorentzian profile.

The approximation in Eq. (A5) can be derived by simplifying $\omega_o{}^2 - \omega^2$ as written in Eq. (A6) :

$$\omega_o{}^2 - \omega^2 = (\omega + \delta\omega)^2 - \omega^2 = 2\omega\delta\omega + \delta\omega^2 \cong 2\omega\delta\omega = 2\omega(\omega_0 - \omega) \tag{A6}$$

where $\delta\omega = \omega_0 - \omega$ and must be relatively small compared to ω.

The approximation condition in Eq. (A6) of $\delta\omega = \omega_0 - \omega$ being relatively small for the considered frequencies ω (i.e. the frequencies with a significant response around the modal resonance peak) occurs when $\nu << \omega_o$. Hence, when the modal resonance profile is relatively 'thin' compared to the value of its peak frequency, the discussed approximations apply.

A2 - Noise Intensity Theory

This section presents the theoretical definition of the noise intensity, and explains its extraction from experimental PSDs using a Lorentzian fit. The modelling by Noiray and Schuermans (IJNLM 2013) assumes that the stochastic heat release ξ is delta-correlated as according to Eq. (A7):

$$\langle \xi\xi_\tau \rangle = \langle \xi(t)\xi(t+\tau) \rangle = \Gamma\delta(\tau) \qquad \text{(A7)}$$

where $\langle \xi\xi_\tau \rangle$ is the autocorrelation of ξ for a time shift τ (the mean of the time series multiplication of $\xi(t)$ and $\xi(t+\tau)$), $\delta(\tau)$ is the Dirac-delta function of τ, and Γ is the noise intensity representing the 'strength' of the delta autocorrelation.

The generic Dirac-delta function $\delta(\tau)$ is a spike defined by $\delta(\tau = 0) = +\infty$ and $\delta(\tau \neq 0) = 0$, and has an area of unity such that $\int_{-\infty}^{\infty} \delta(\tau)\, d\tau = 1$. The units of the Dirac-delta function are the inverse of those of its argument; in this case 1/s. The 'strength' Γ of a scaled Dirac-delta function $\Gamma\delta(\tau)$ represents the area of the function since $\int_{-\infty}^{\infty} \Gamma\delta(\tau)\, d\tau = \Gamma$.

In reality, ξ is quasi delta-correlated and not perfectly thin nor infinite. The area covered by $\langle \xi\xi_\tau \rangle$ is its noise intensity Γ; as is intuitively obvious, a greater noise level raises the $\langle \xi\xi_\tau \rangle$ profile.

From Eq. (A7), the PSD of ξ can be derived using the autocorrelation definition of a two-sided PSD given by Eq. (A8).

$$S_{\xi\xi}(\omega) = \frac{1}{\pi} \int_0^{\infty} \langle \xi\xi_\tau \rangle \cos(\omega\tau)\ d\tau \qquad \text{(A8)}$$

Since $\langle \xi\xi_\tau \rangle$ is only valued at $\tau = 0$ where $\cos(\omega\tau) = 1$, and the integration is for positive τ only, the integration results in half of the area of $\langle \xi\xi_\tau \rangle$. Accordingly, the PSD of ξ is written in Eq. (A9) for radians and in Eq. (A10) for Hertz. These relations show that delta correlation ≡ white noise.

$$S_{\xi\xi}(\omega) = \frac{\Gamma}{2\pi} \qquad \text{(A9)}$$

$$S_{\xi\xi}(f) = \Gamma \qquad \text{(A10)}$$

Hence, the noise intensity Γ can be thought of as the constant PSD height of the stochastic heat release driving; analogous to the driving force in Eq. (A5). Accordingly, in this work, Γ was extracted from the maximum M of a Lorentzian profile fitted onto an experimental one-sided PSD $G_{p'p'}(f)$ (twice the two-sided PSD: $G_{p'p'}(f) = 2\, S_{p'p'}(f)$) using the relation of Eq. (A11), which is based on the approximation of Eq. (A5).

$$\Gamma = 0.5 \times M_{G_{p'p'}(f)} \times 4\nu^2\omega^2 \qquad \text{(A11)}$$

Appendix B

This appendix is comprised of two sections B1 and B2 providing details of the data processing during experiments, and of the data post-processing in the application of parameter extraction methods.

B1 - Experimental Data Processing

For both BKH and BKD experiments, the dynamic pressure signals were obtained with quartz cylinder pressure probes of the Kistler model 6043A60 at a 100 kHz sampling rate and with a ± 0.04 bar uncertainty.

The data was passed through a charge amplifier (Kistler model 5011B) with a 30 kHz low-pass filter for anti-aliasing. This uses a second-order Butterworth filter. This type of filter maximises the flatness of the amplitude response, and in this case it ensures a flat amplitude response in the frequency range of interest (<11 kHz). The phase response of a standard second-order low-pass filter is given by Eq. (B1):

$$\varphi(\omega) = -\tan^{-1}\left(\frac{1}{\alpha}\left(2\frac{\omega}{\omega_0}+\sqrt{4-\alpha^2}\right)\right)-\tan^{-1}\left(\frac{1}{\alpha}\left(2\frac{\omega}{\omega_0}-\sqrt{4-\alpha^2}\right)\right) \qquad \text{(B1)}$$

where $\varphi(\omega)$ is the phase response, ω_0 is the cut-off frequency (in this case 30 kHz) and α is the damping ratio (equal to the inverse of the quality factor). For a Butterworth filter, α = 1.414.

The ideal phase response of a filter is a linear function with a negative slope, which ensures that the signal is not distorted in the time domain. Although Eq. (B1) is not a linear function, for the frequency range up to $\frac{\omega}{\omega_0}$ = 1 and with α = 1.414 Eq. (B1) closely approximates a linear function as shown in Figure 53. Hence, non-ideal phase effects in the experimental data are minimal.

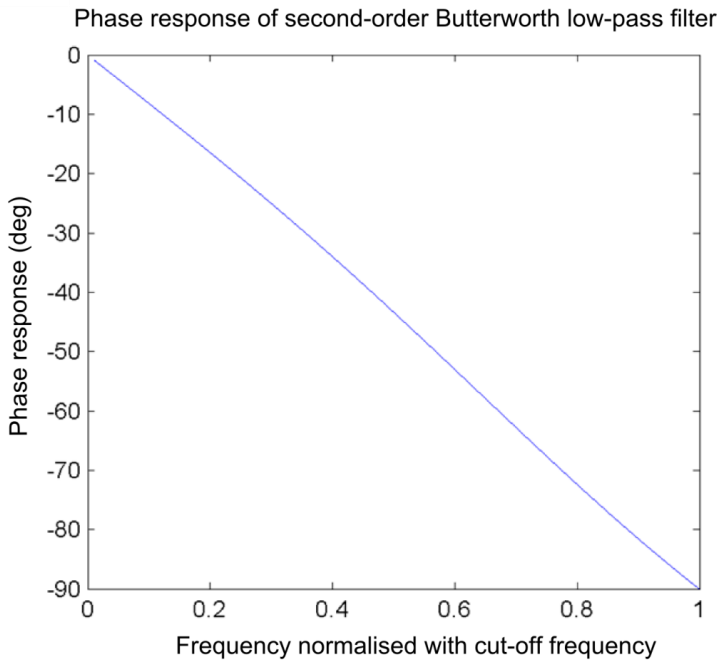

Figure 53: Phase response of second-order Butterworth low-pass filter until the cut-off frequency.

B2 - Experimental Data Post-processing

The experimental data was post-processed to generate PSDs and filtered time series. The PSDs were all generated using Hanning windows without overlap. The frequency resolution for the BKH acoustic pressure PSDs is 1 Hz, and that for the acoustic pressure PSDs of the BKD LP7 A and B modes is 6 Hz. These resolutions are sufficiently fine such that bias errors in the Lorentzian PSD profiles are negligible.

The normalised bias error ε_b of an estimator $\hat{\theta}$ for a variable θ is given by Eq. (B2):

$$\varepsilon_b = \frac{b(\hat{\theta})}{\theta} = \frac{E(\hat{\theta})}{\theta} - 1 \qquad \text{(B2)}$$

where $E(\hat{\theta})$ is the expected value of the estimator (its mean value, independent of random error).

A Lorentzian PSD profile is flattened at its peak and raised at its skirts due to discrete frequency bands that average mean square values over their range. With a coarser frequency resolution, the Lorentzian peak is flattened due to the decaying spectrum around the peak, while the Lorentzian skirts are raised due the Lorentzian profile rising closer to its peak more strongly than decaying away from it. The normalised Lorentzian bias error is given by Eq. (B3) (Bendat & Piersol, 2010):

$$\varepsilon_b = -\frac{1}{3}\left(\frac{B_e}{B_r}\right)^2 \qquad \text{(B3)}$$

where B_e is the bandwidth (frequency resolution), and B_r is the full-width half-maximum of the Lorentzian profile (two times its net damping rate).

The $\frac{B_e}{B_r}$ ratio for the considered Lorentzian profiles in this work is highest for the BKD LP7 A mode, where $\frac{B_e}{B_r}$ = 0.019, which makes the bias error negligible at ε_b = -0.012 %. Hence, in this work, parameter extraction using Lorentzian fits is not influenced by bias error.

The frequency resolution of the PSDs of acoustic amplitude envelope and envelope fluctuation was increased until the PSDs were well-resolved and their profiles did not observably change with increasing resolution. Formal analyses of their bias errors is not presented since these PSDs were not for parameter extraction, but simply for qualitative comparison with expected profiles.

The presence of random error in the PSDs is attributable to the highly turbulent rocket flames which cause the driving white noise spectrum to have significant fluctuations instead of being smoothly flat. However, since Lorentzian fits were applied to a relatively wide frequency range (compared to the frequency resolution of PSDs) the effect of this random error on fit quality is assumed to be negligible.

To produce the filtered time series for data analysis with the Fokker-Planck coefficients method, an inbuilt Matlab function 'idealfilter' was used. This post-processing function is an ideal filter with no amplitude attenuation nor signal distortion.

Appendix C

This appendix is comprised of three sections C1, C2 and C3 providing details of the BKH data analyses. The first section shows the selections of the time series for the 1L, 1T and 1L1T modes of the BKH load points from experimental spectrograms, the second presents the Lorentzian fits to these BKH acoustic modes, and the third presents the transition moments and associated extrapolations for the 1L and 1T modes.

C1 - Selection of Times Series for BKH Load Points

The time series selections for the four BKH load points are shown in Figures 54 to 57. The time series are selected such that external driving effects from the secondary nozzle, which are present in the experimental runs, are avoided.

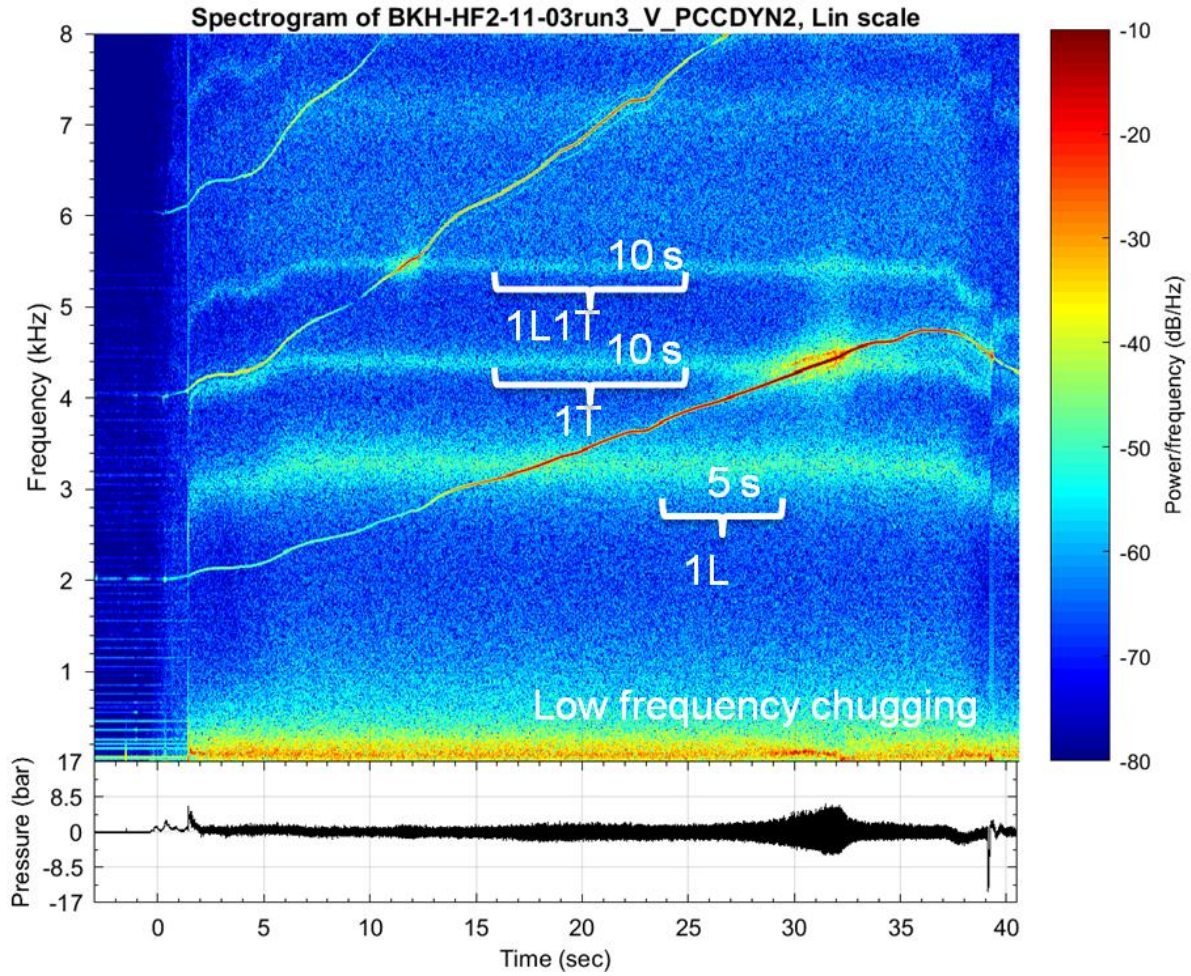

Figure 54: BKH GH2 60 bar time series selections for the 1L, 1T and 1L1T modes from the spectrogram of the PCCdyn2 sensor during an experimental run. The frequency of the secondary nozzle driving is linearly ramped during the experiment. The time series for the modes were selected to avoid external driving effects. Low frequency chugging can be observed at the bottom of the spectrogram.

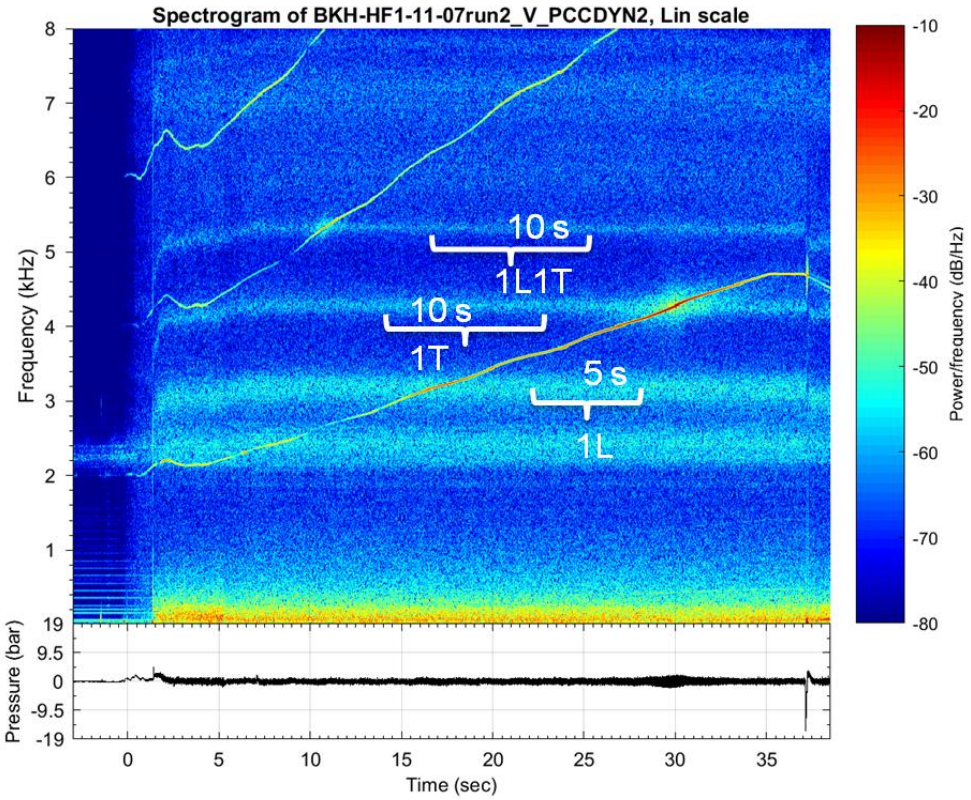

Figure 55: BKH GH2 40 bar time series selections for the 1L, 1T and 1L1T modes from the spectrogram of the PCCdyn2 sensor during an experimental run. The frequency of the secondary nozzle driving is linearly ramped during the experiment. The time series for the modes were selected to avoid external driving effects.

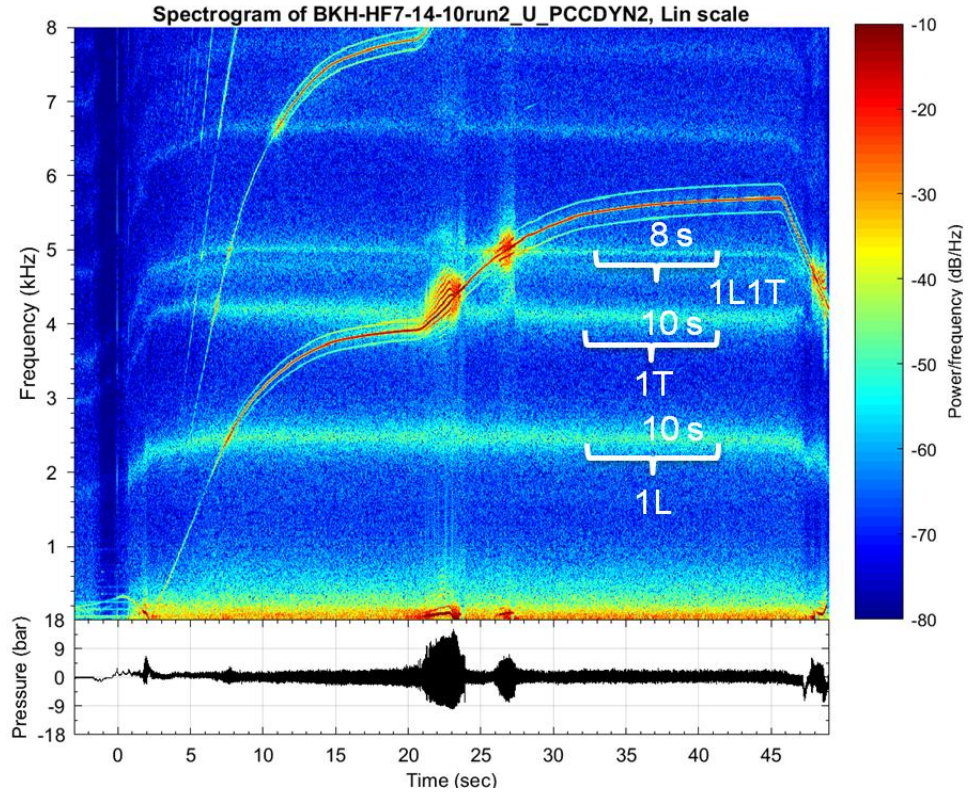

Figure 56: BKH LH2 60 bar time series selections for the 1L, 1T and 1L1T modes from the spectrogram of the PCCdyn2 sensor during an experimental run. The frequency of the secondary nozzle driving is linearly ramped during the experiment. The time series for the modes were selected to avoid external driving effects.

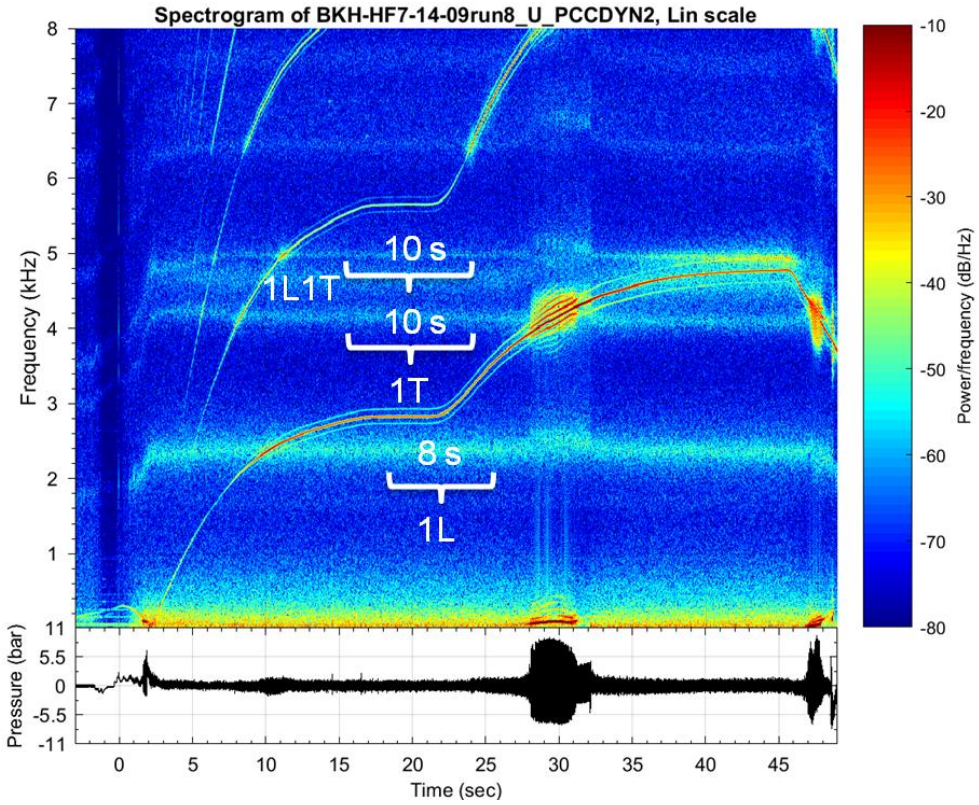

Figure 57: BKH LH2 40 bar time series selections for the 1L, 1T and 1L1T modes from the spectrogram of the PCCdyn2 sensor during an experimental run. The frequency of the secondary nozzle driving is linearly ramped during the experiment. The time series for the modes were selected to avoid external driving effects.

C2 - Lorentzian Fits to BKH Acoustic Modes

The Lorentzian fits to the 1L, 1T and 1L1T modes of the four BKH load points are shown in Figures 58 to 69. An optimisation algorithm which minimises the least squares error was used to fit the Lorentzian profile onto the experimental PSDs. It can be seen that the Lorentzian profiles for the 1L1T mode have a reduced frequency range compared to the 1L and 1T modes, and hence the stochastic signal processing techniques were not applied to 1L1T mode data. The PSDs are all one-sided and have a frequency resolution of 1 Hz.

Strong noise forcing can make non-linear effects significant in a stable mode. However, since a clear Lorentzian fit was obtained for the GH2 60 bar 1L mode, which has the highest noise intensity of all the BKH modes studied in this work, the BKH load points studied in this work are considered to have linearly stable modes since a Lorentzian profile occurs only at linear conditions.

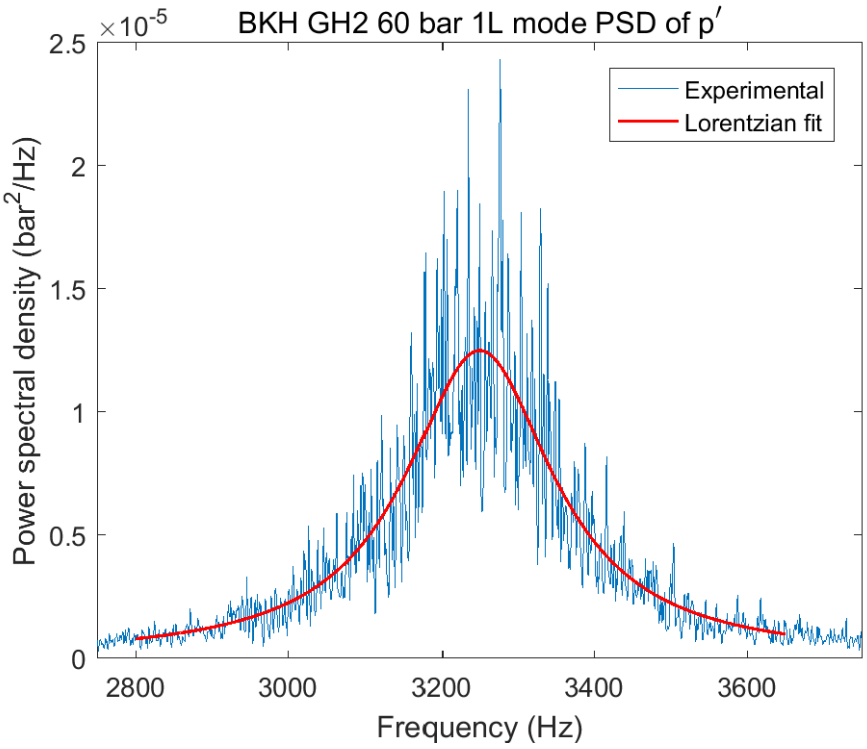

Figure 58: BKH GH2 60 bar 1L mode Lorentzian fit.

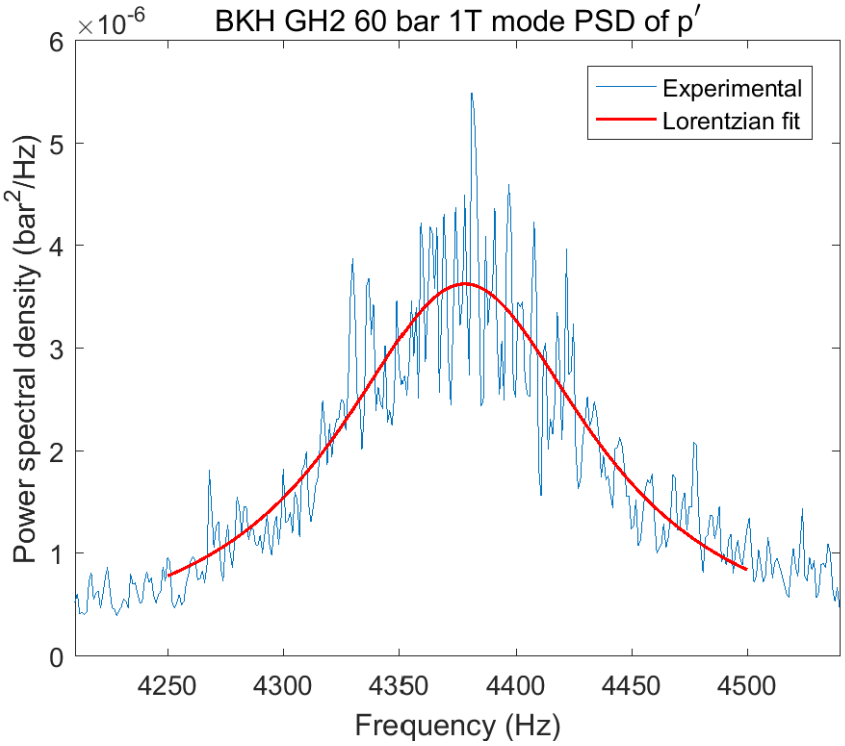

Figure 59: BKH GH2 60 bar 1T mode Lorentzian fit.

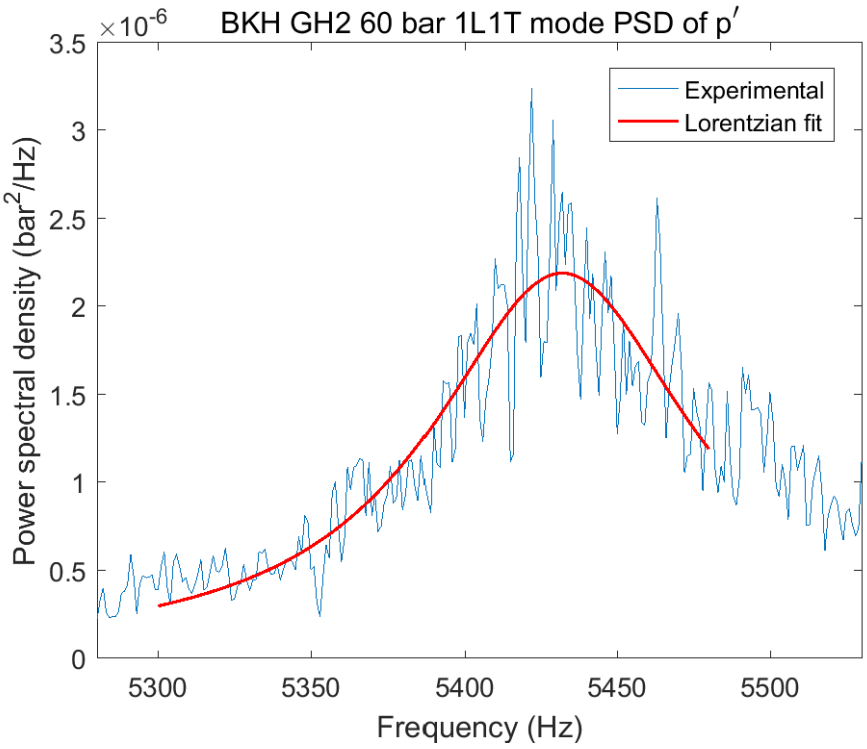

Figure 60: BKH GH2 60 bar 1L1T mode Lorentzian fit.

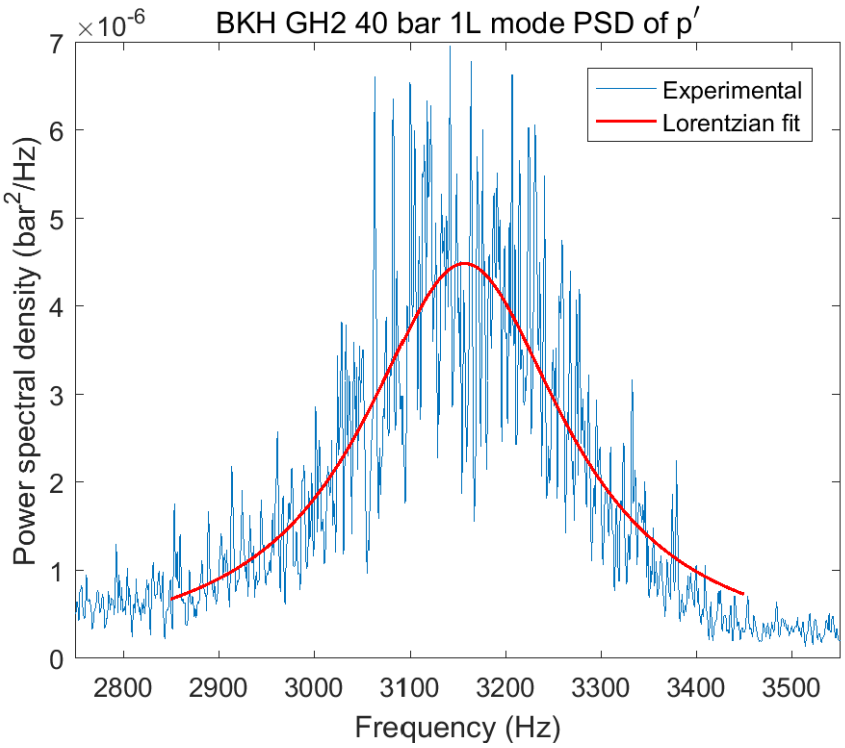

Figure 61: BKH GH2 40 bar 1L mode Lorentzian fit.

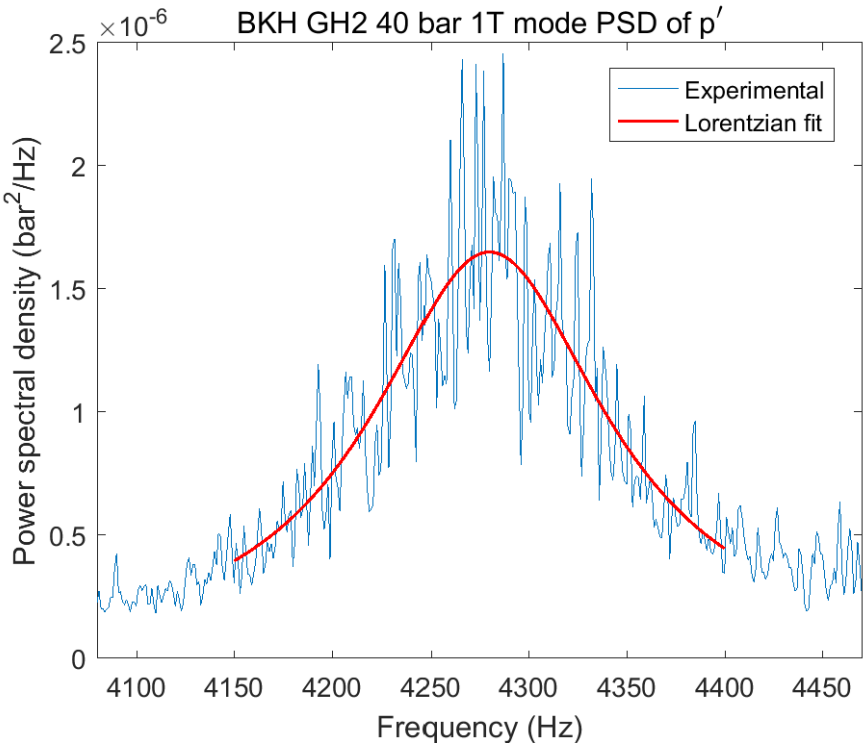

Figure 62: BKH GH2 40 bar 1T mode Lorentzian fit.

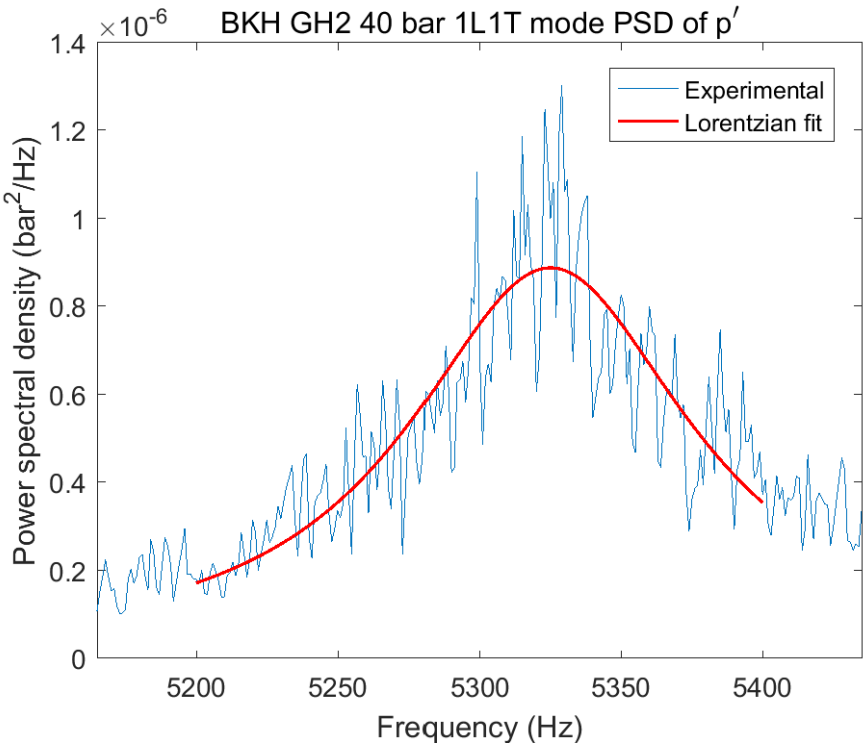

Figure 63: BKH GH2 40 bar 1L1T mode Lorentzian fit.

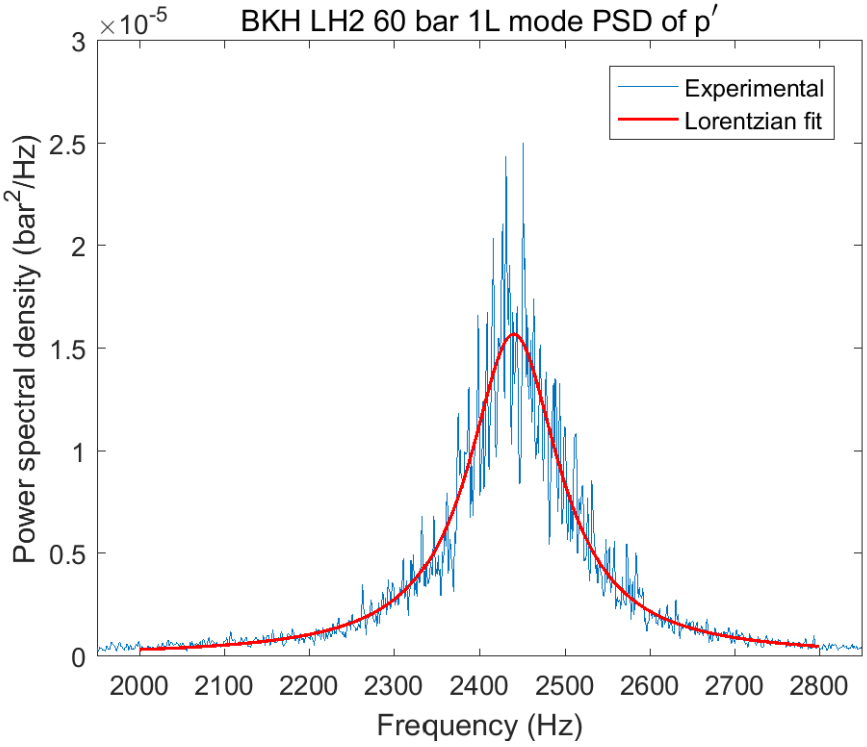

Figure 64: BKH LH2 60 bar 1L mode Lorentzian fit.

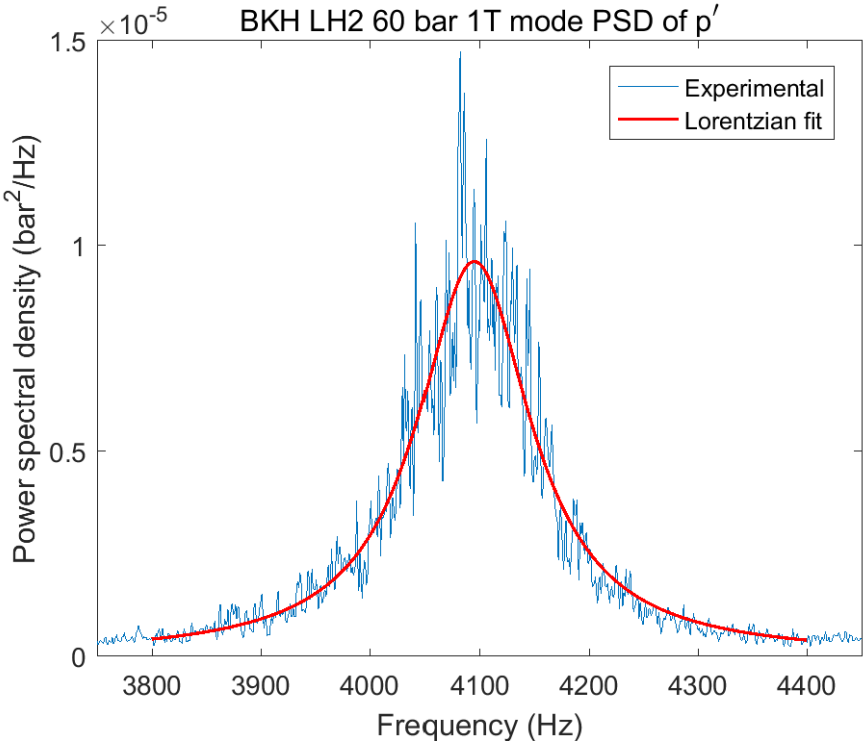

Figure 65: BKH LH2 60 bar 1T mode Lorentzian fit.

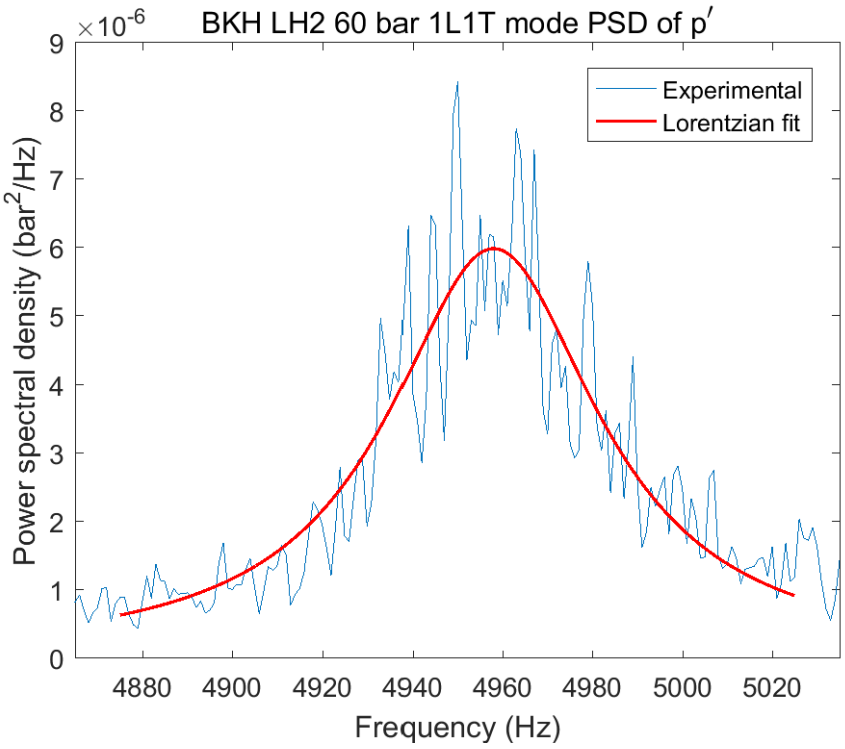

Figure 66: BKH LH2 60 bar 1L1T mode Lorentzian fit.

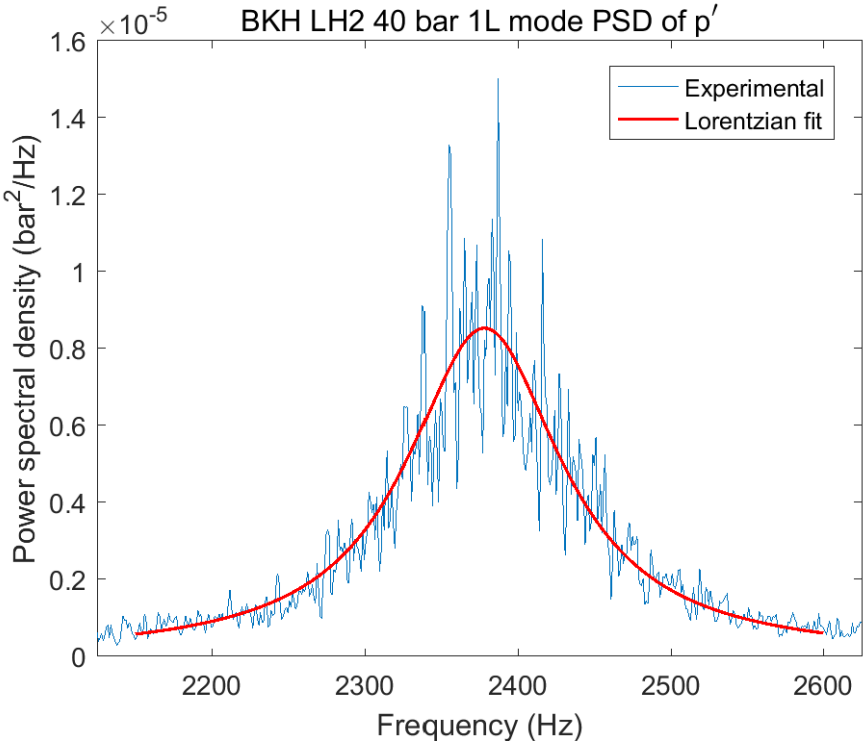

Figure 67: BKH LH2 40 bar 1L mode Lorentzian fit.

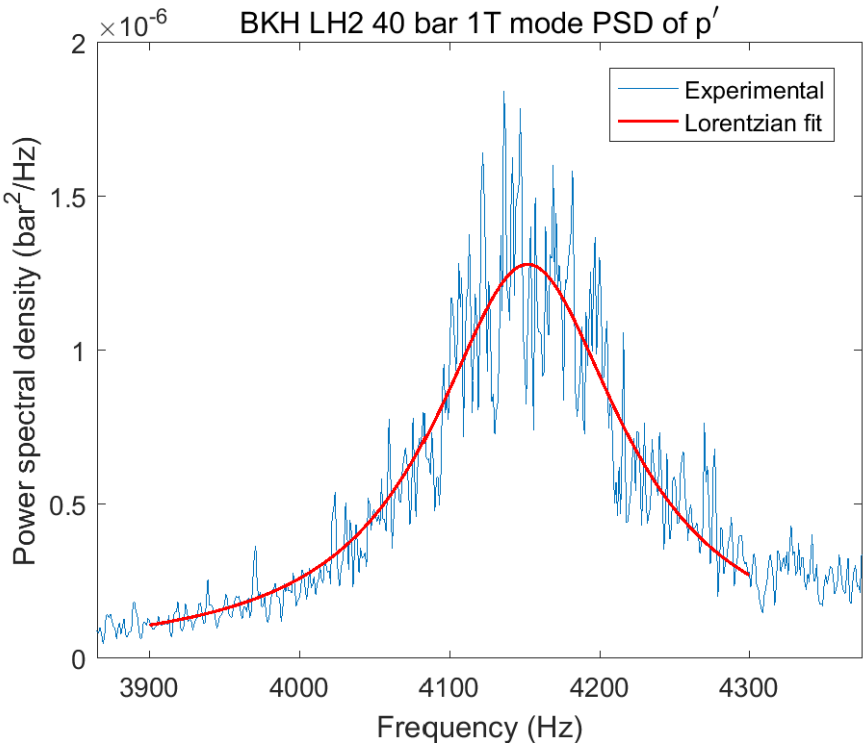

Figure 68: BKH LH2 40 bar 1T mode Lorentzian fit.

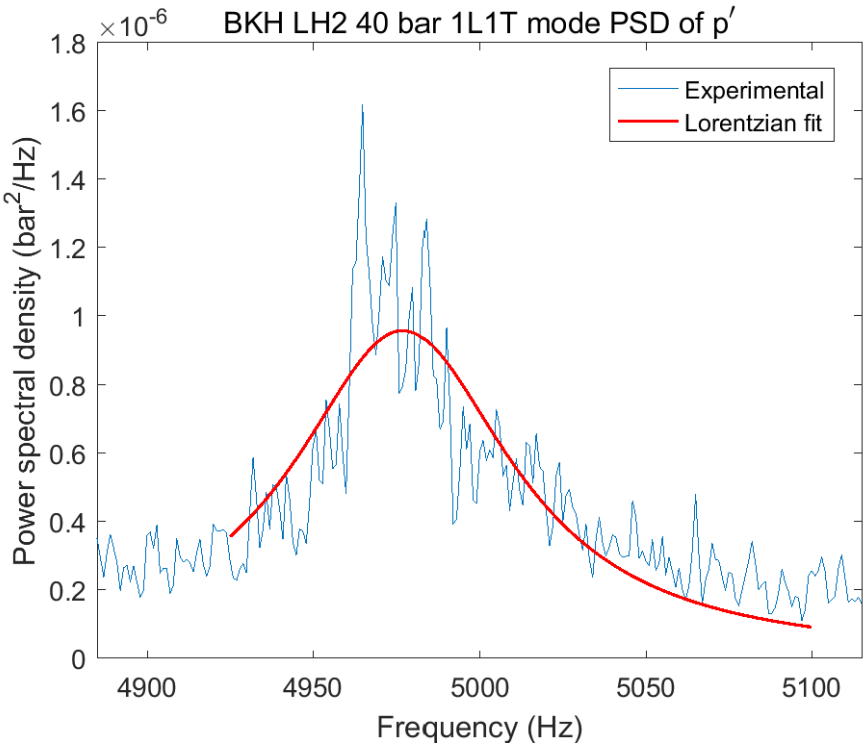

Figure 69: BKH LH2 40 bar 1L1T mode Lorentzian fit.

C3 - Extrapolation of Transition Moments for BKH 1L and 1T Modes

The extrapolation coefficients used for the transition moments of the BKH 1L and 1T modes are specified in Table 9, and the extrapolations of transition moments are shown in Figures 70 to 77.

Table 9: Extrapolation coefficients for the first and second transition moments of the 1L and 1T modes of the four BKH load points.

BKH load point	Extrapolation coefficient c (s^{-1}) for each amplitude percentile							
	10th	20th	30th	40th	50th	60h	70th	80th
GH2, 60 bar								
1L $D_\tau^{(1)}$	-89.5	-94.8	-160	-91.0	-93.6	-93.6	-93.6	-94.8
1L $D_\tau^{(2)}$	-96.9	-91.0	-87.9	-89.5	-94.8	-97.9	-95.9	-97.9
1T $D_\tau^{(1)}$	-104	-117	-102	-109	-111	-112	-115	N.A.
1T $D_\tau^{(2)}$	-111	-98.8	-101	-109	-114	-118	-121	N.A.
GH2, 40 bar								
1L $D_\tau^{(1)}$	-92.4	-97.4	-203	-93.6	-96.9	-96.9	-96.9	-99.7
1L $D_\tau^{(2)}$	-99.1	-89.5	-91.0	-93.6	-96.9	-99.7	-104	-107
1T $D_\tau^{(1)}$	-103	-112	-100	-106	-109	-110	-112	N.A.
1T $D_\tau^{(2)}$	-113	-104	-100	-104	-109	-114	-116	N.A.
LH2, 60 bar								N.A.
1L $D_\tau^{(1)}$	-73.0	-73.0	-89.5	-73.0	-73.0	-73.0	-73.0	N.A.
1L $D_\tau^{(2)}$	-73.0	-73.0	-91.0	-93.6	-73.0	-73.0	-73.0	N.A.
1T $D_\tau^{(1)}$	-73.0	-73.0	-91.0	-73.0	-73.0	-73.0	-73.0	N.A.
1T $D_\tau^{(2)}$	-73.0	-73.0	-92.4	-73.0	-73.0	-73.0	-73.0	N.A.
LH2, 40 bar								N.A.
1L $D_\tau^{(1)}$	-73.0	-73.0	-73.0	-73.0	-73.0	-73.0	-73.0	N.A.
1L $D_\tau^{(2)}$	-73.0	-73.0	-73.0	-73.0	-73.0	-73.0	-73.0	N.A.
1T $D_\tau^{(1)}$	-73.0	-73.0	-73.0	-73.0	-73.0	-73.0	-73.0	N.A.
1T $D_\tau^{(2)}$	-73.0	-73.0	-73.0	-73.0	-73.0	-73.0	-73.0	N.A.

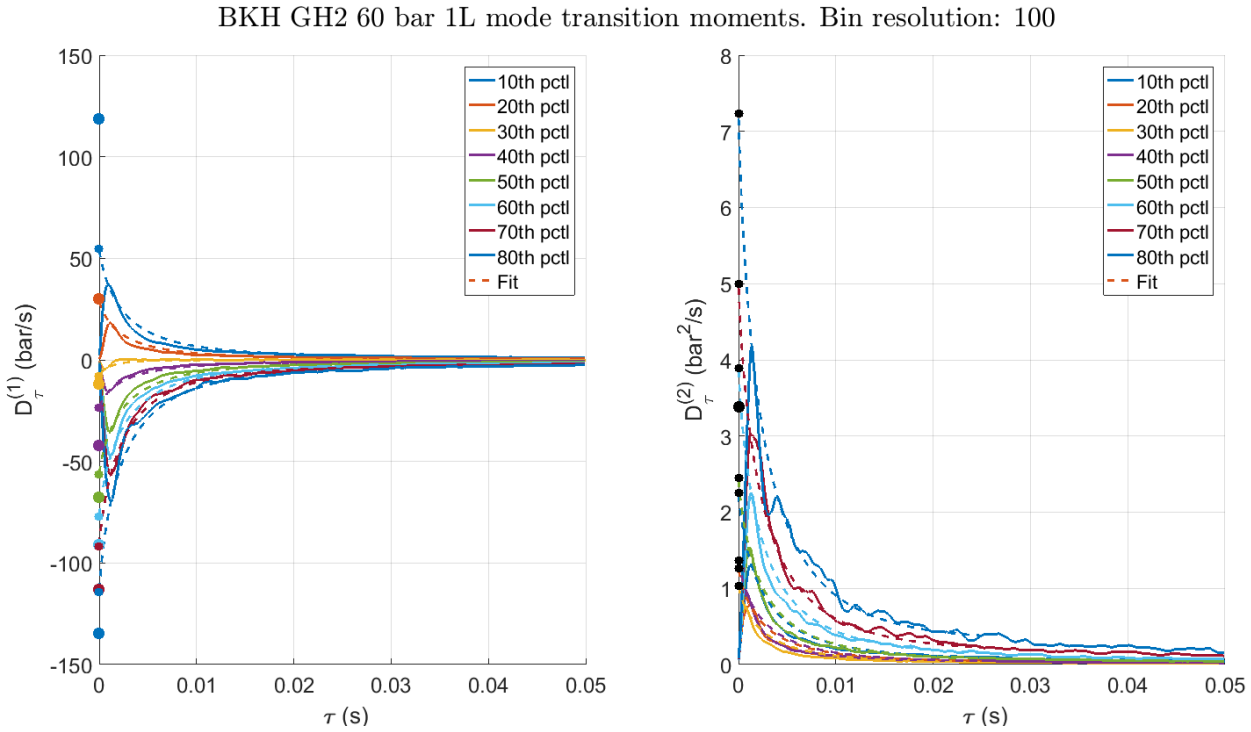

Figure 70: BKH GH2 60 bar 1L mode transition moments and extrapolations. Small dots on the y-axis are the limits to zero of the transition moments obtained with extrapolations, while big dots are the expected values based on parameters found with Lorentzian fitting.

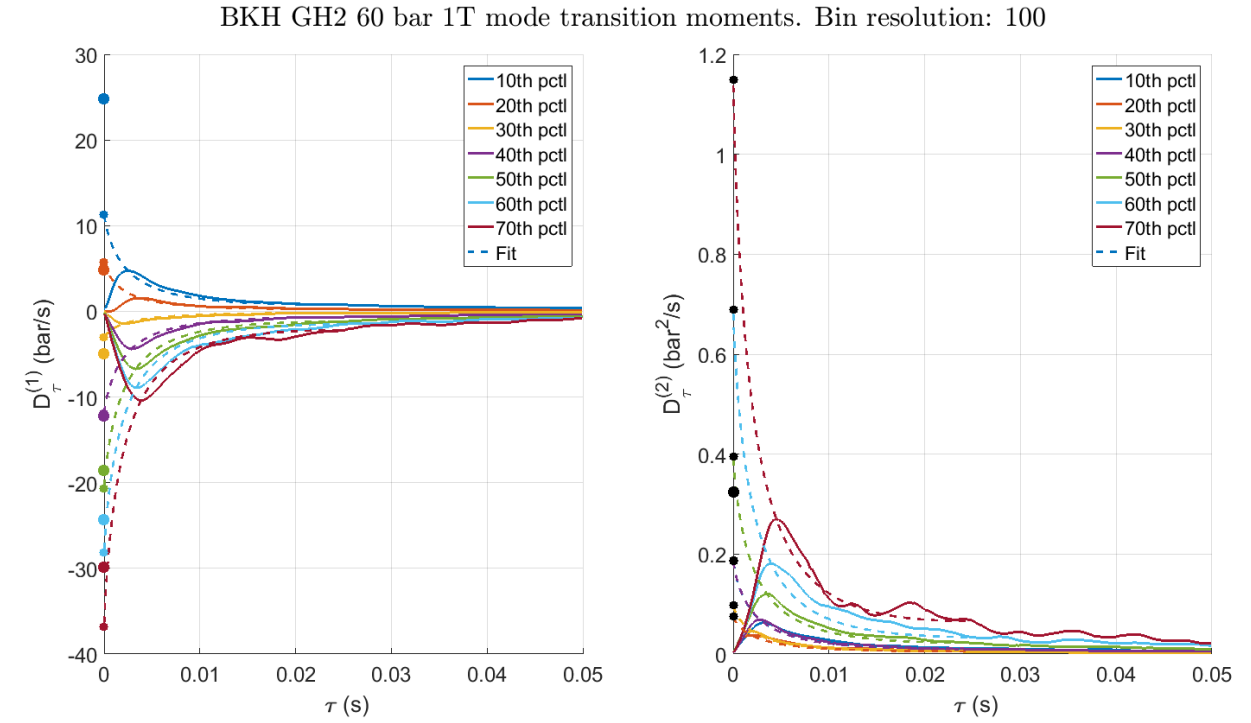

Figure 71: BKH GH2 60 bar 1T mode transition moments and extrapolations. Small dots on the y-axis are the limits to zero of the transition moments obtained with extrapolations, while big dots are the expected values based on parameters found with Lorentzian fitting.

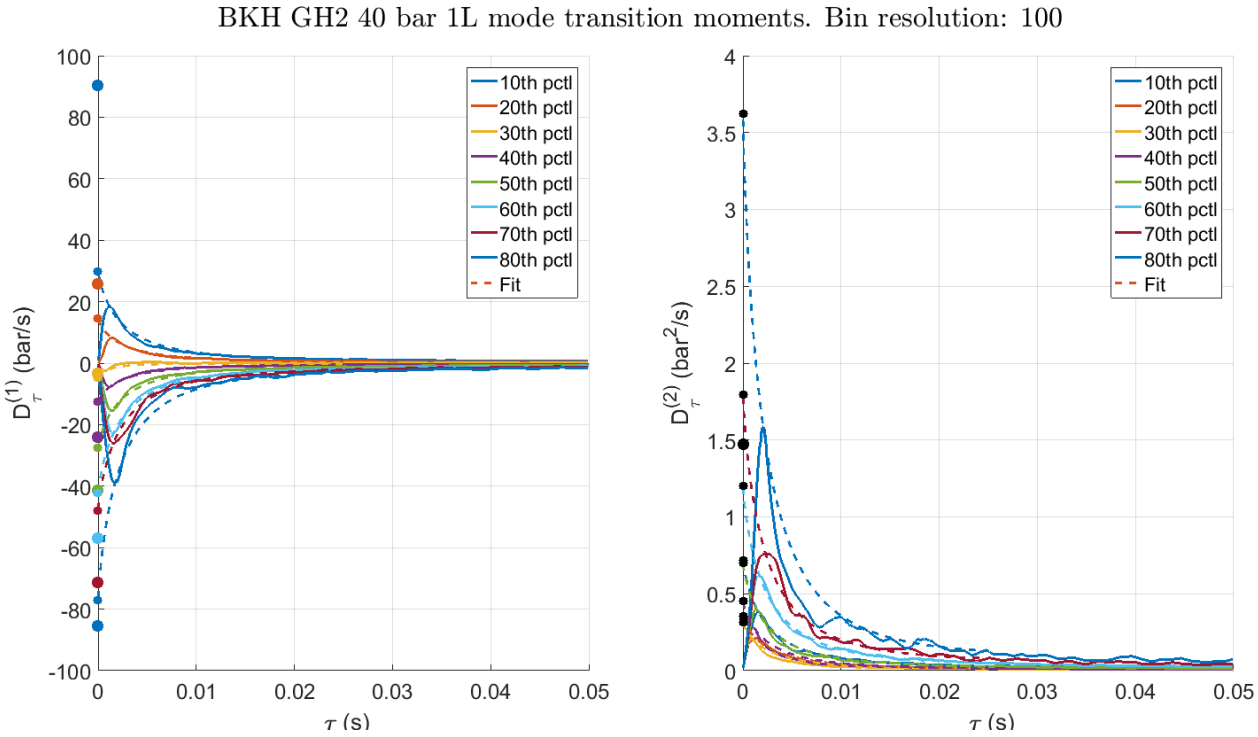

Figure 72: BKH GH2 40 bar 1L mode transition moments and extrapolations. Small dots on the y-axis are the limits to zero of the transition moments obtained with extrapolations, while big dots are the expected values based on parameters found with Lorentzian fitting.

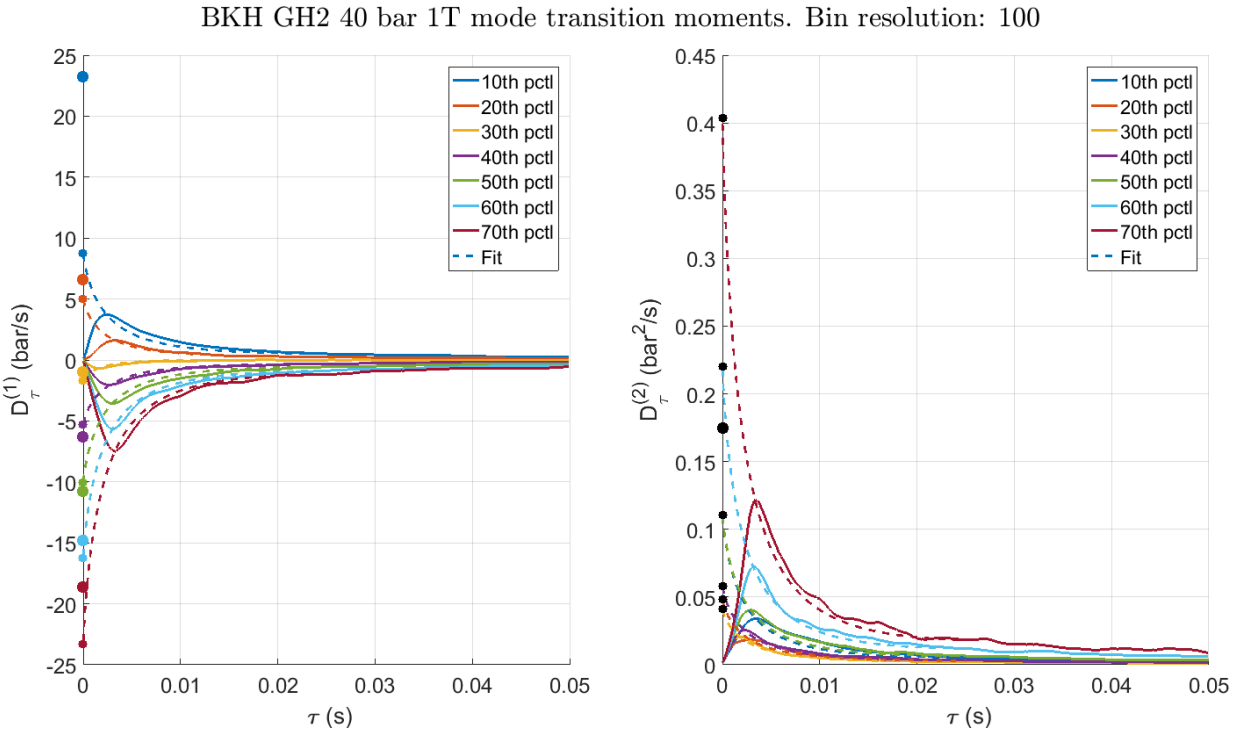

Figure 73: BKH GH2 40 bar 1T mode transition moments and extrapolations. Small dots on the y-axis are the limits to zero of the transition moments obtained with extrapolations, while big dots are the expected values based on parameters found with Lorentzian fitting.

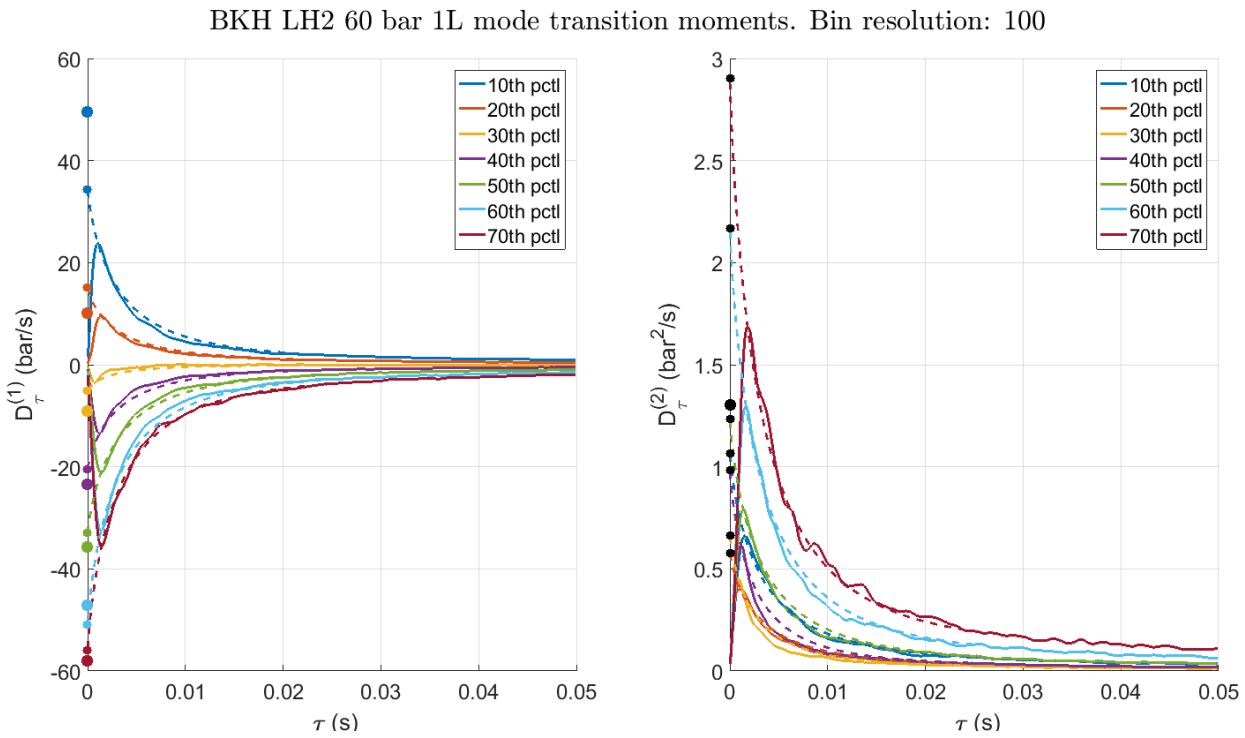

Figure 74: BKH LH2 60 bar 1L mode transition moments and extrapolations. Small dots on the y-axis are the limits to zero of the transition moments obtained with extrapolations, while big dots are the expected values based on parameters found with Lorentzian fitting.

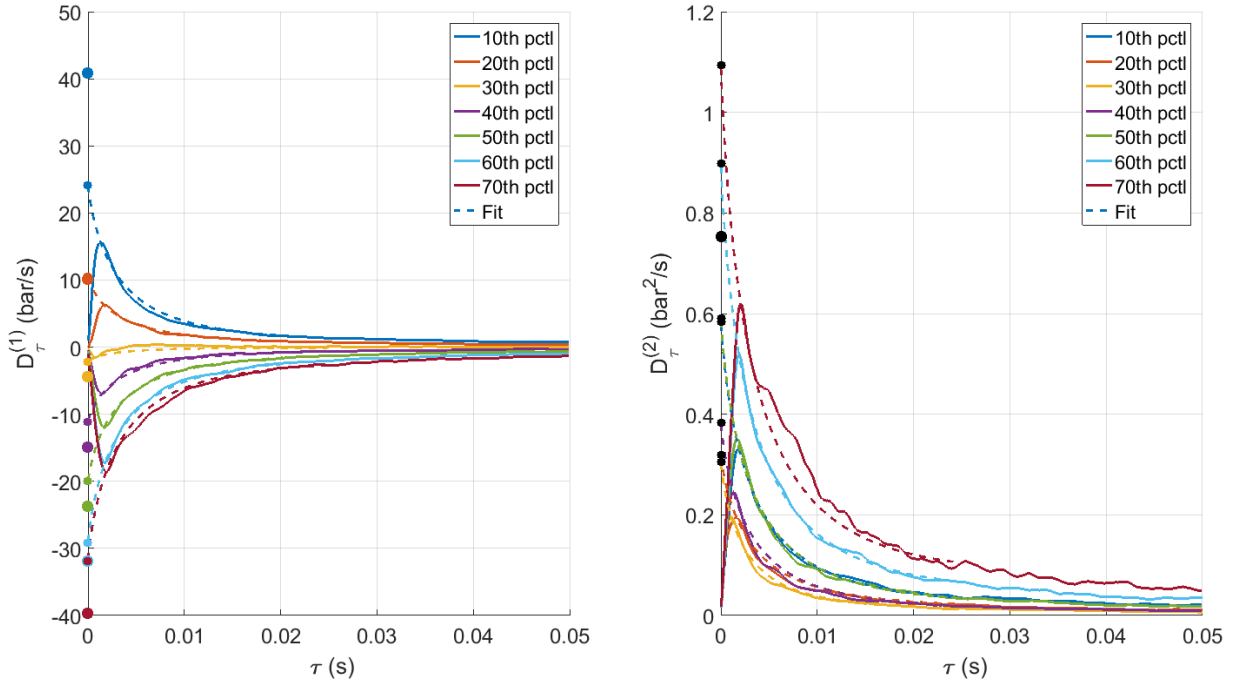

Figure 75: BKH LH2 60 bar 1T mode transition moments and extrapolations. Small dots on the y-axis are the limits to zero of the transition moments obtained with extrapolations, while big dots are the expected values based on parameters found with Lorentzian fitting.

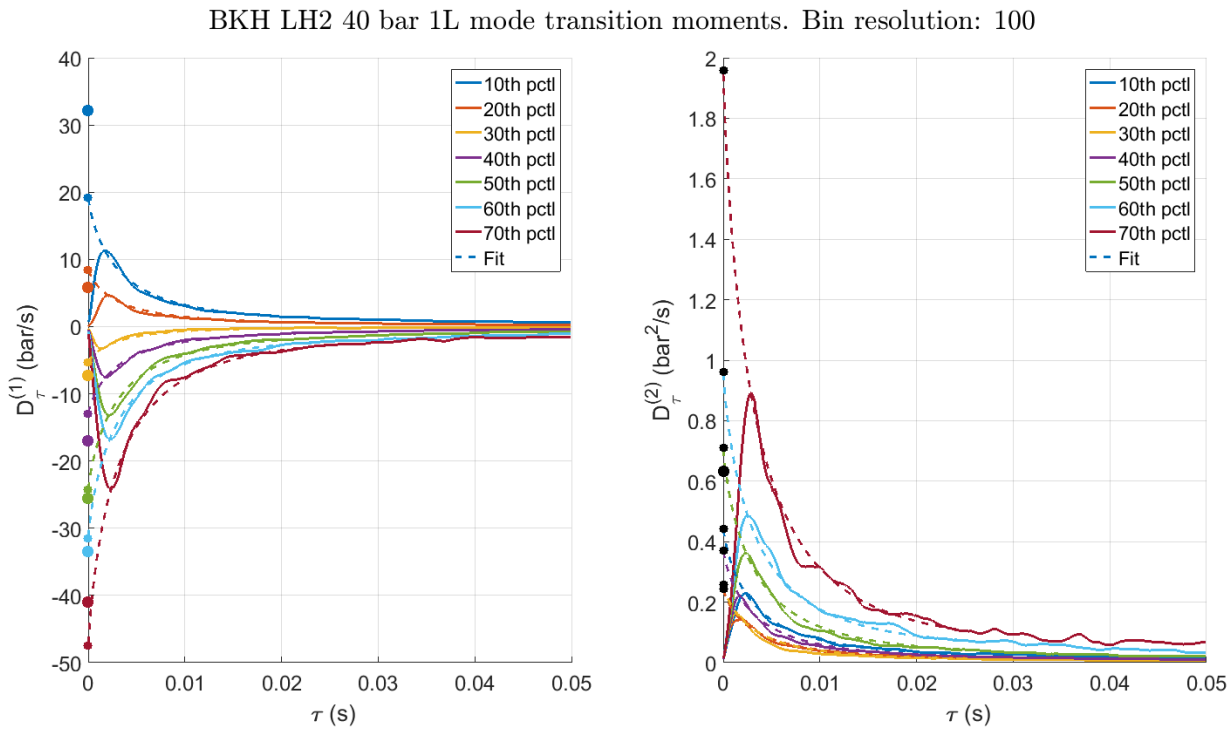

Figure 76: BKH LH2 40 bar 1L mode transition moments and extrapolations. Small dots on the y-axis are the limits to zero of the transition moments obtained with extrapolations, while big dots are the expected values based on parameters found with Lorentzian fitting.

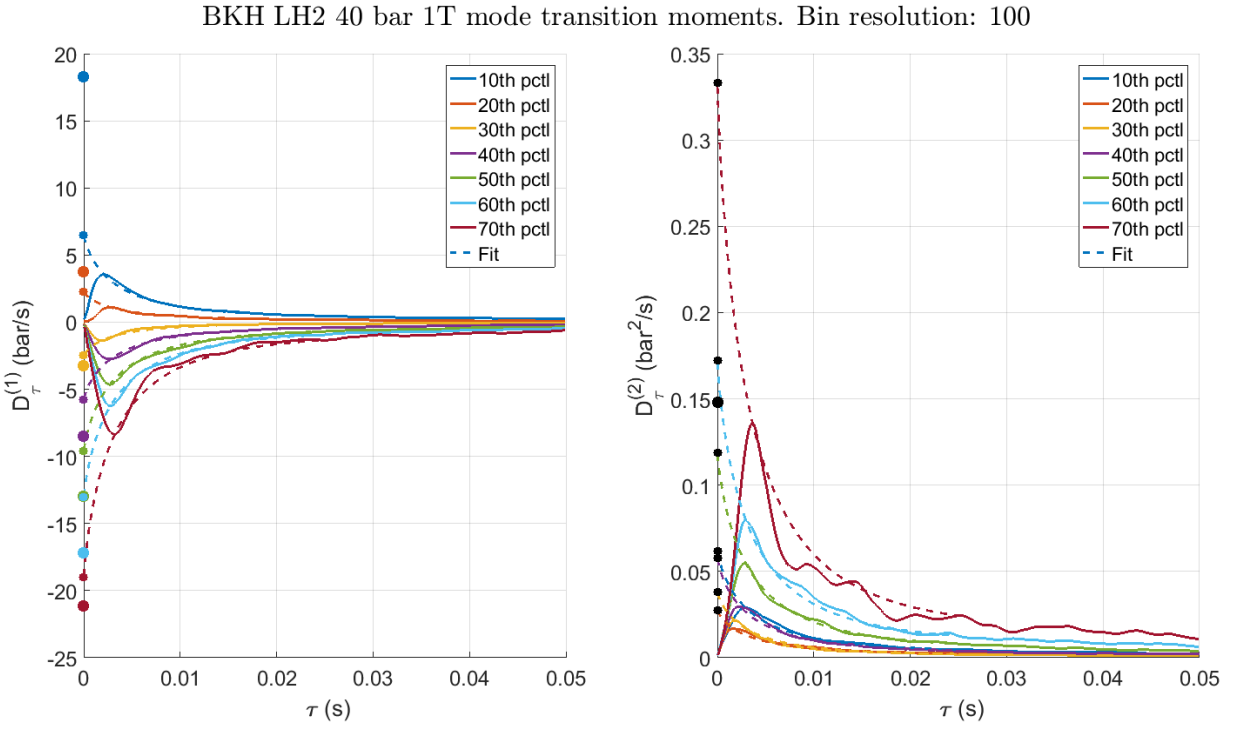

Figure 77: BKH LH2 40 bar 1T mode transition moments and extrapolations. Small dots on the y-axis are the limits to zero of the transition moments obtained with extrapolations, while big dots are the expected values based on parameters found with Lorentzian fitting.

Appendix D

This appendix is comprised of three sections D1, D2 and D3 providing details of the BKD data analyses. The first section provides the extrapolation coefficient c values used for BKD data analyses, the second and third sections D2 and D3 provide the resolution analyses for the BKD 1T A and B mode analyses respectively.

D1 - Extrapolation Coefficient Values for BKD 1T Mode Analyses

The extrapolation coefficient c values used for BKD 1T mode analyses are presented in Table 10.

Table 10: Extrapolation coefficient c values used for BKD data analyses.

BKD LP7 analysis case	**Extrapolation coefficient c (s^{-1}) for each amplitude**						
1T A (1x20)	**A1**	**A2**	**A3**	**A4**	**A5**	**A6**	**A7**
m							
$D_{\tau}^{(1)}$	-550	-500	-500	-500	-771	-771	-771
$D_{\tau}^{(2)}$	-771	-771	-771	-771	-771	-771	-771
v2							
$D_{\tau}^{(1)}$	-550	-500	-500	-500	-236	-771	-771
$D_{\tau}^{(2)}$	-771	-771	-771	-771	-771	-771	-771
v3							
$D_{\tau}^{(1)}$	-550	-500	-500	-500	-104	-771	-771
$D_{\tau}^{(2)}$	-771	-771	-771	-771	-771	-771	-771
1T B (2x20)	**B1**	**B2**	**B3**	**B4**	**B5**	**B6**	**B7**
m							
$D_{\tau}^{(1)}$	-771	-771	-771	-771	-771	-771	-771
$D_{\tau}^{(2)}$	-771	-771	-771	-771	-771	-771	-771

D2 - BKD 1T A Mode Resolution Analysis

First and second transition moments were computed for the BKD 1T A mode using two bin resolutions of 1x20 and 2x20 bins. Since signal quality is visibly lower for 2x20 bins, the analysis focused on 1x20 bins. For the 1x20 bin resolution, three cases were considered consisting of fixing $\breve{B}$ to its exact modal value (m) or to two neighbouring values (v2 and v3) in the $\breve{B}$ histogram. The transition moment signals for the 1x20, 1x20 v2, 1x20 v3 and 2x20 bin resolution cases are shown in Figures 78, 79, 80 and 81.

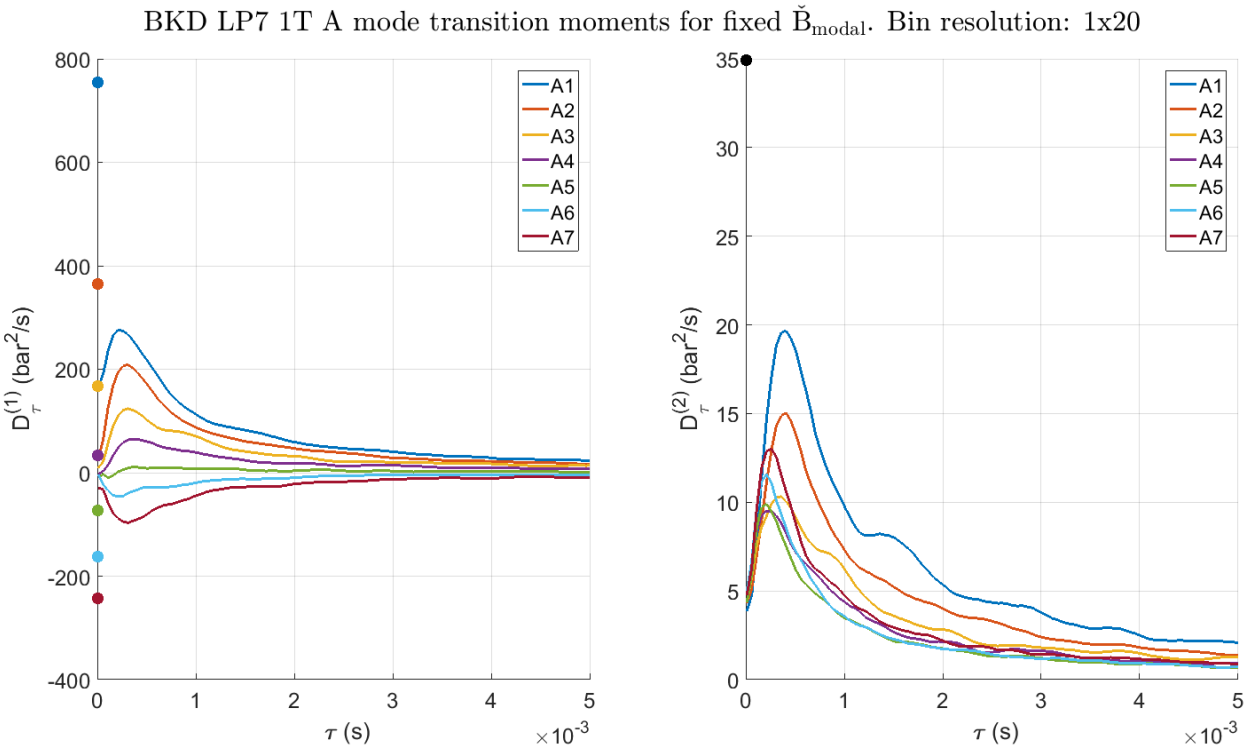

Figure 78: BKD LP7 1T A mode transition moments for the modal (m) value of $\check{B}$. Bin resolution: 1x20.

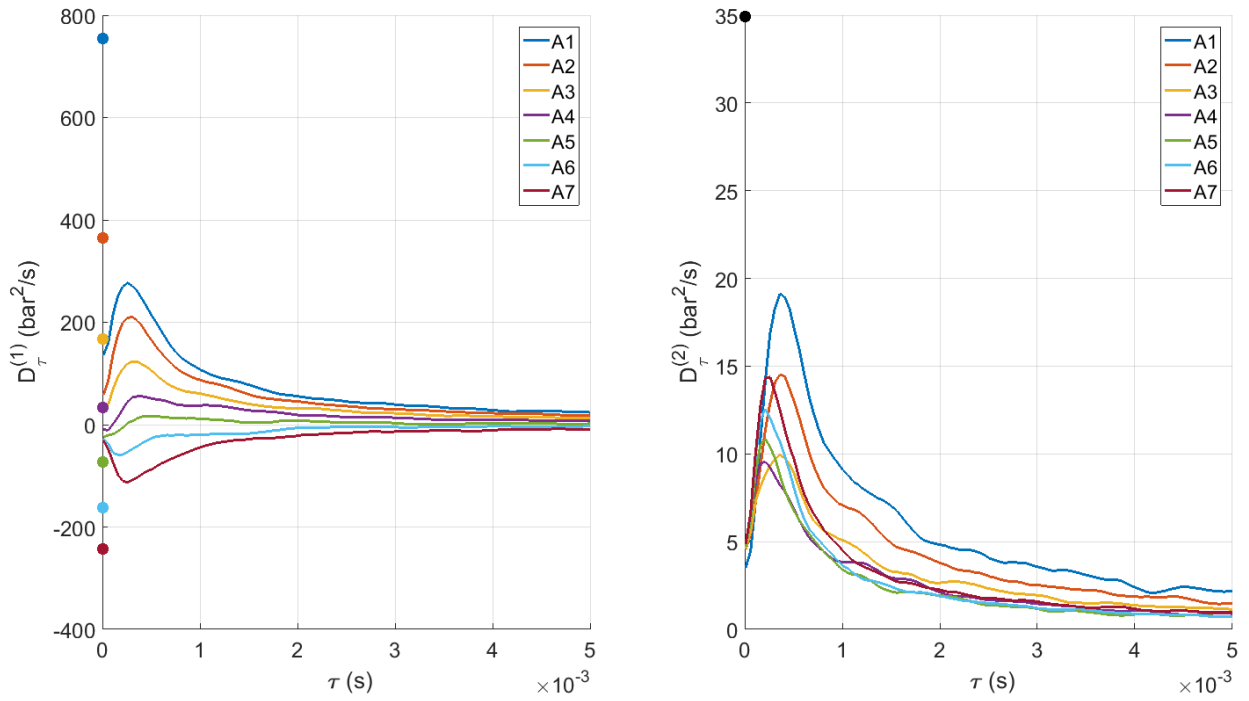

Figure 79: BKD LP7 1T A mode transition moments for the modal (v2) value of $\check{B}$. Bin resolution: 1x20.

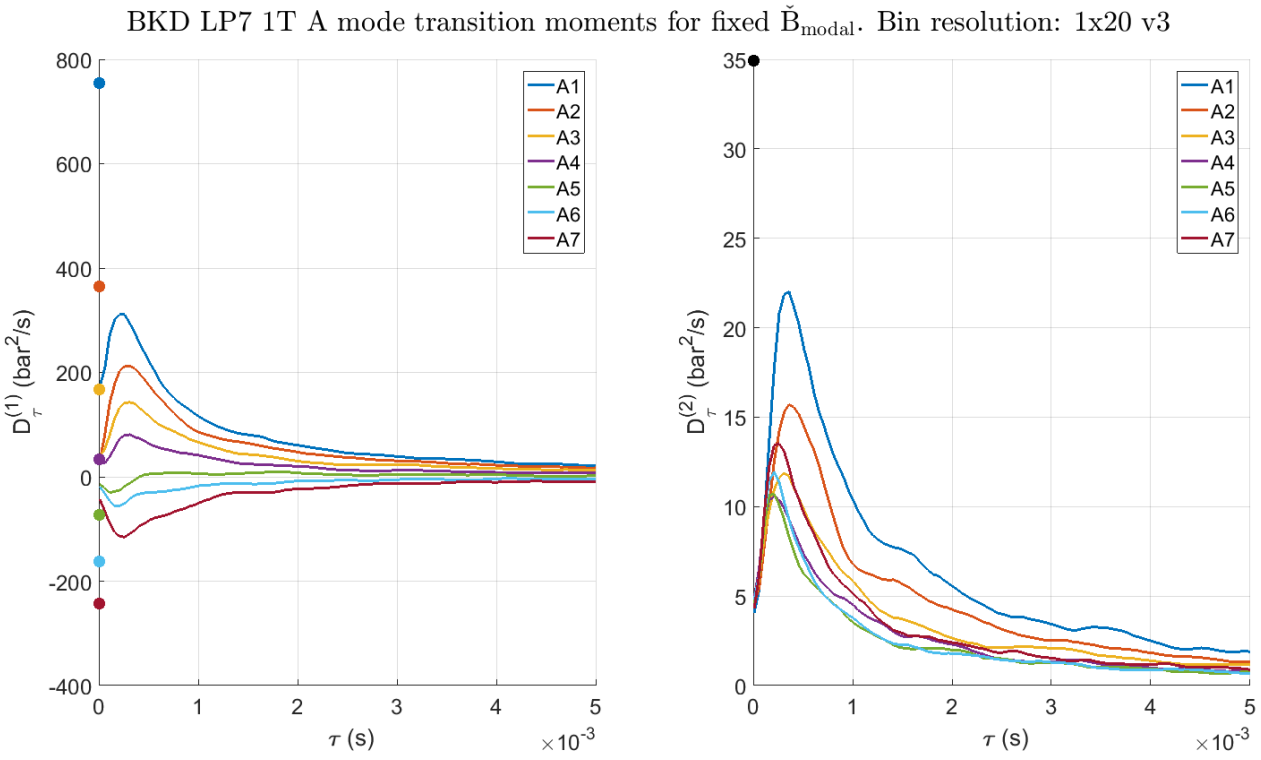

Figure 80: BKD LP7 1T A mode transition moments for the modal (v3) value of $\check{B}$. Bin resolution: 1x20.

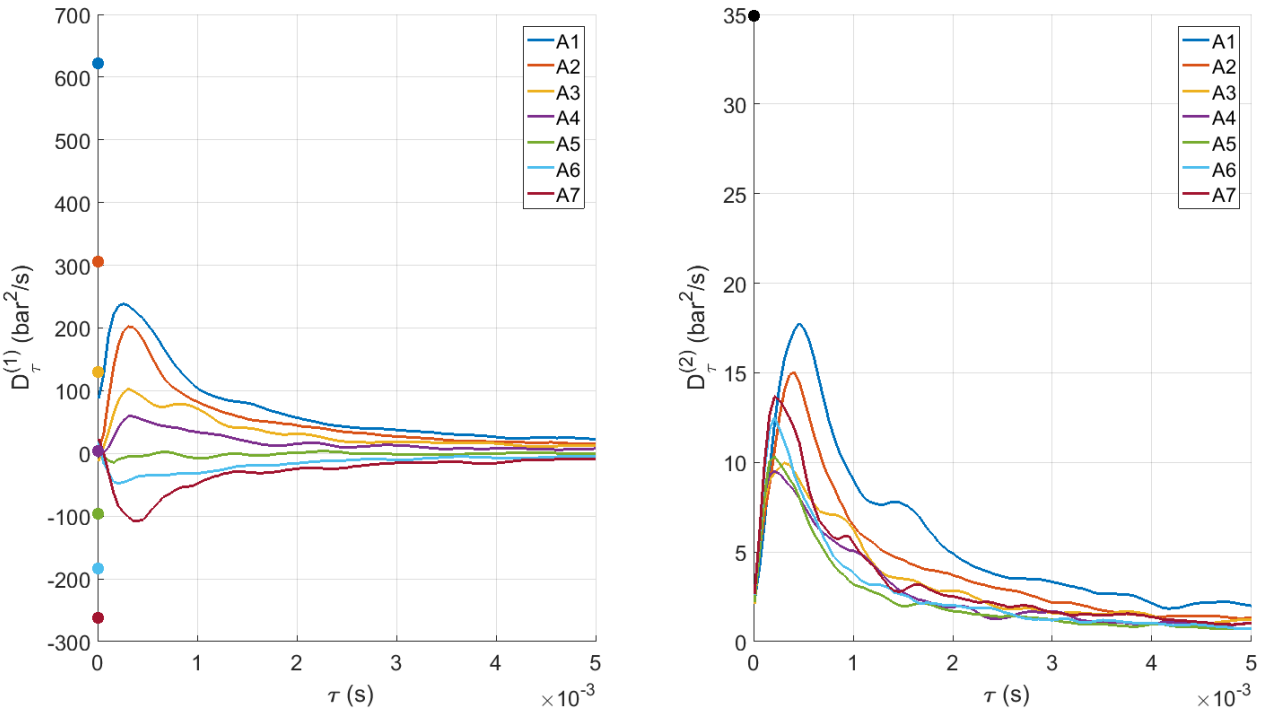

Figure 81: BKD LP7 1T A mode transition moments for the modal (m) value of $\check{B}$. Bin resolution: 2x20.

D3 - BKD 1T B Mode Resolution Analysis

First and second transition moments were computed for the BKD 1T B mode using four bin resolutions of 1x20, 2x20, 3x20 and 4x20 bins. Signal quality is visibly lesser for the 3x20 and 4x20 bin resolutions than for the 1x20 and 2x20 bin resolutions if the exact modal value is used for fixing $\breve{A}$. The analysis focused on a resolution of 2x20 bins since it is a higher resolution than 1x20 bins and still has good signal quality. For the 2x20 bin resolution, three cases were considered consisting of fixing $\breve{A}$ to its exact modal value (m) or to two neighbouring values (v2 and v3) in the $\breve{A}$ histogram. The transition moment signals for the 1x20, 2x20, 2x20 v2, 2x20 v3, 3x20 and 4x20 bin resolution cases are shown in Figures 82, 83, 84, 85, 86 and 87.

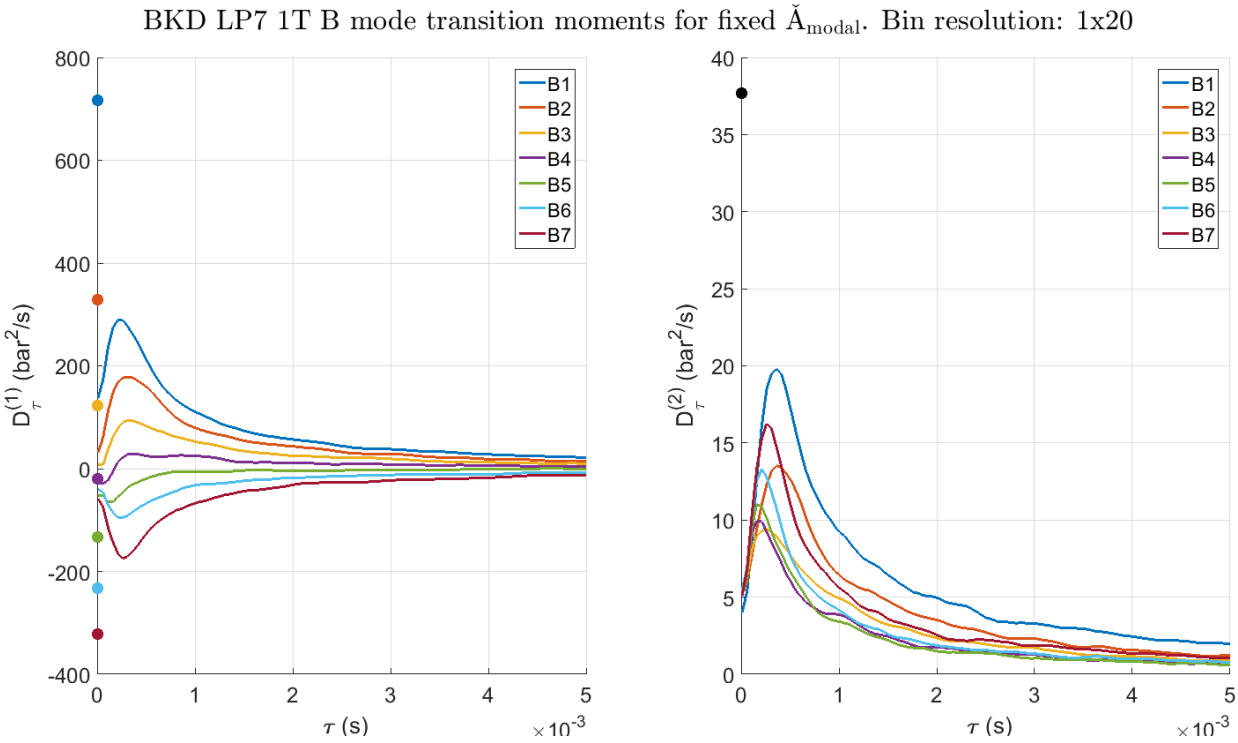

Figure 82: BKD LP7 1T B mode transition moments for the modal (m) value of $\breve{B}$. Bin resolution: 1x20.

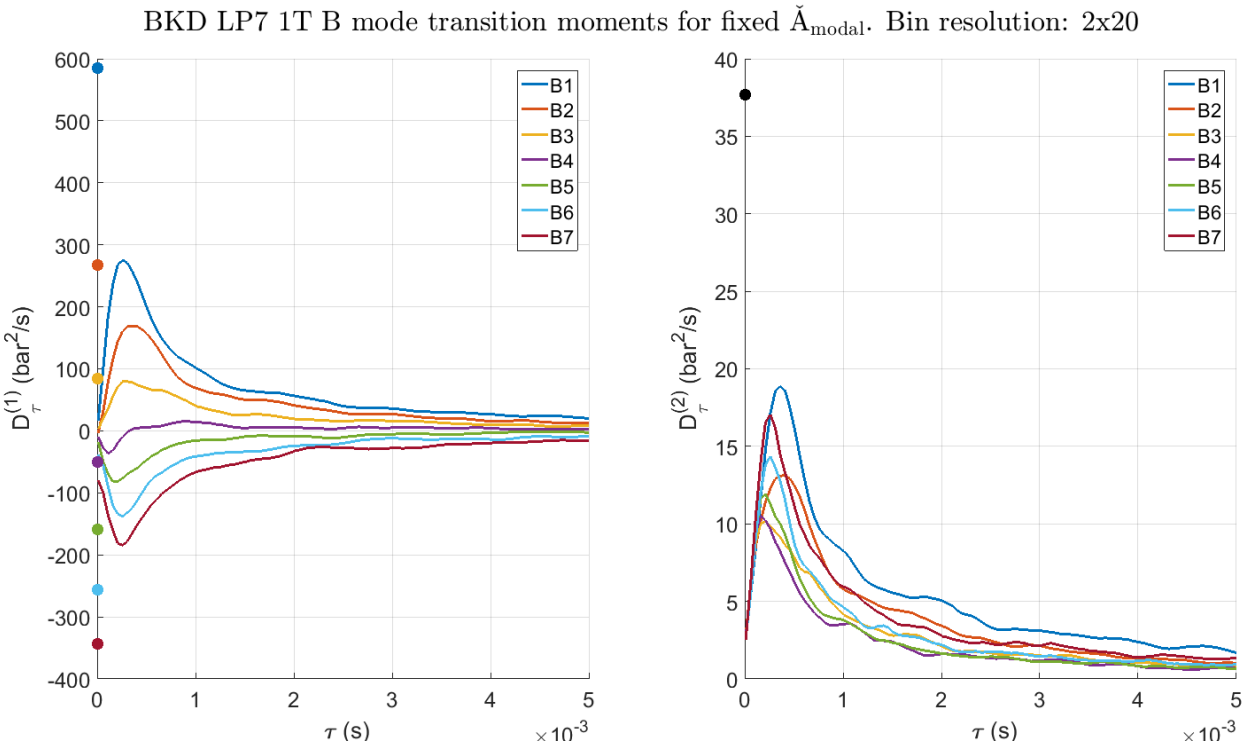

Figure 83: BKD LP7 1T B mode transition moments for the modal (m) value of B̆. Bin resolution: 2x20.

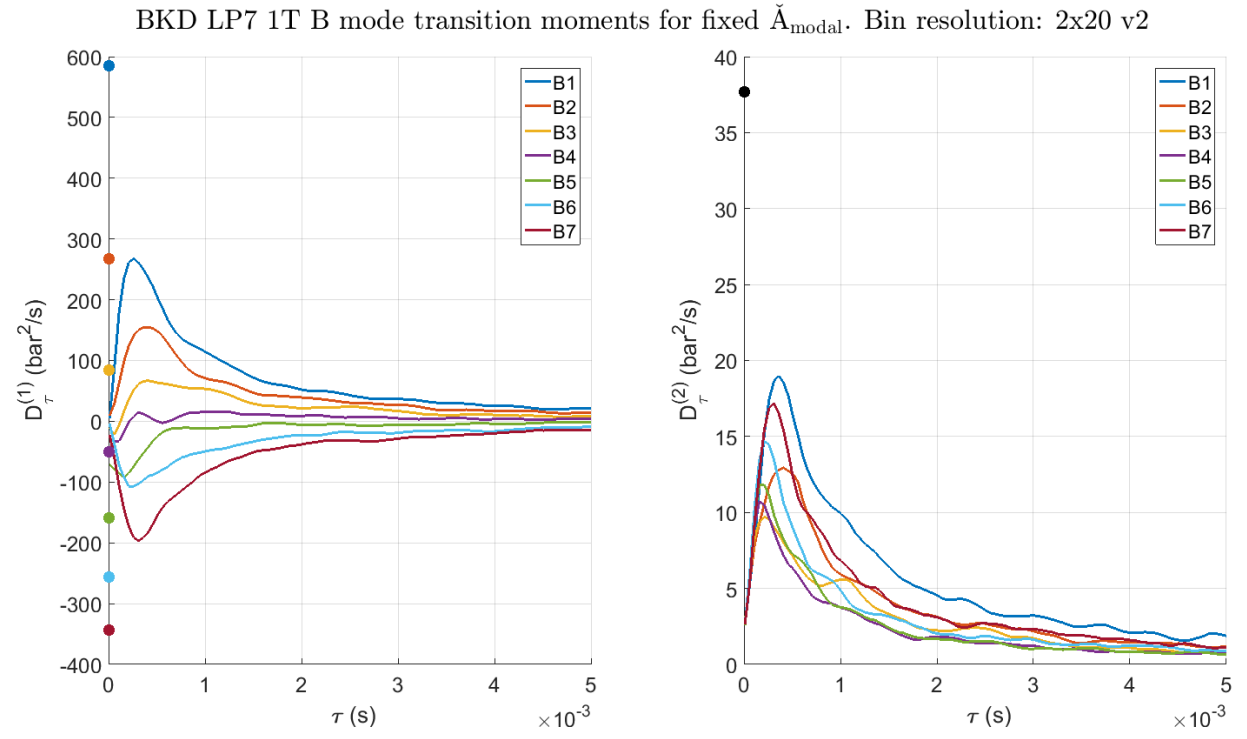

Figure 84: BKD LP7 1T B mode transition moments for the modal (v2) value of B̆. Bin resolution: 2x20.

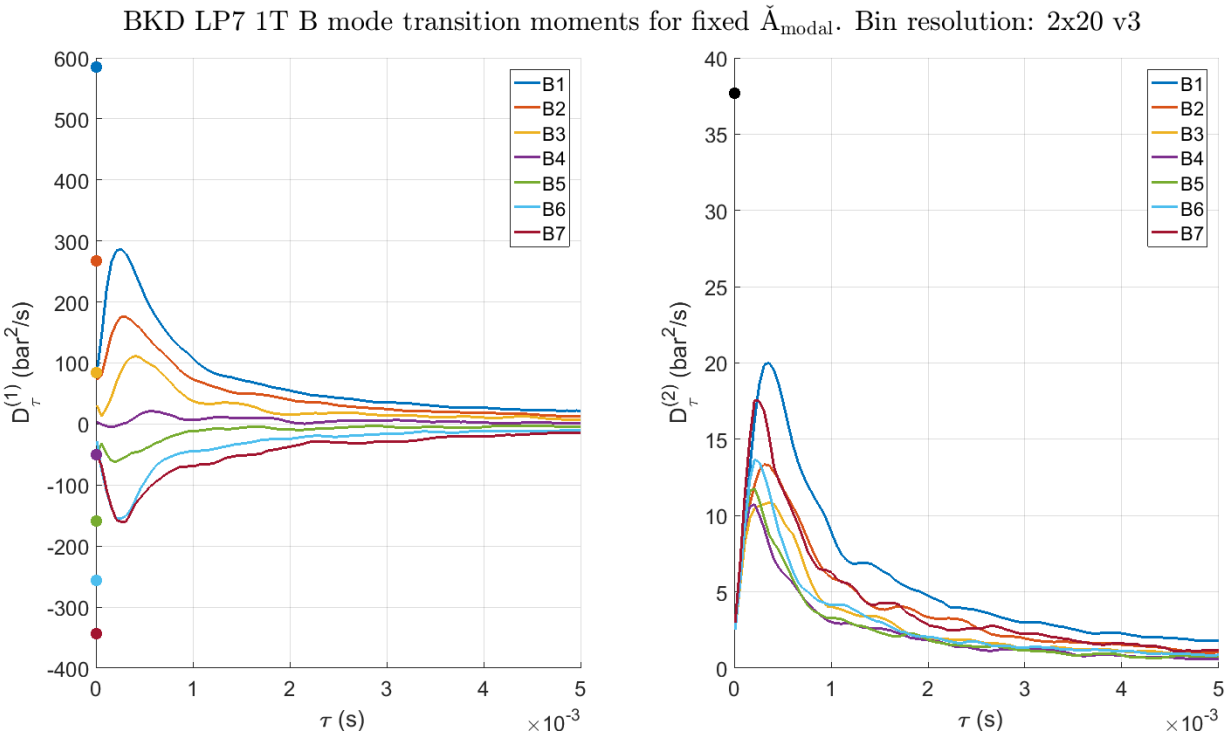

Figure 85: BKD LP7 1T B mode transition moments for the modal (v3) value of B̆. Bin resolution: 2x20.

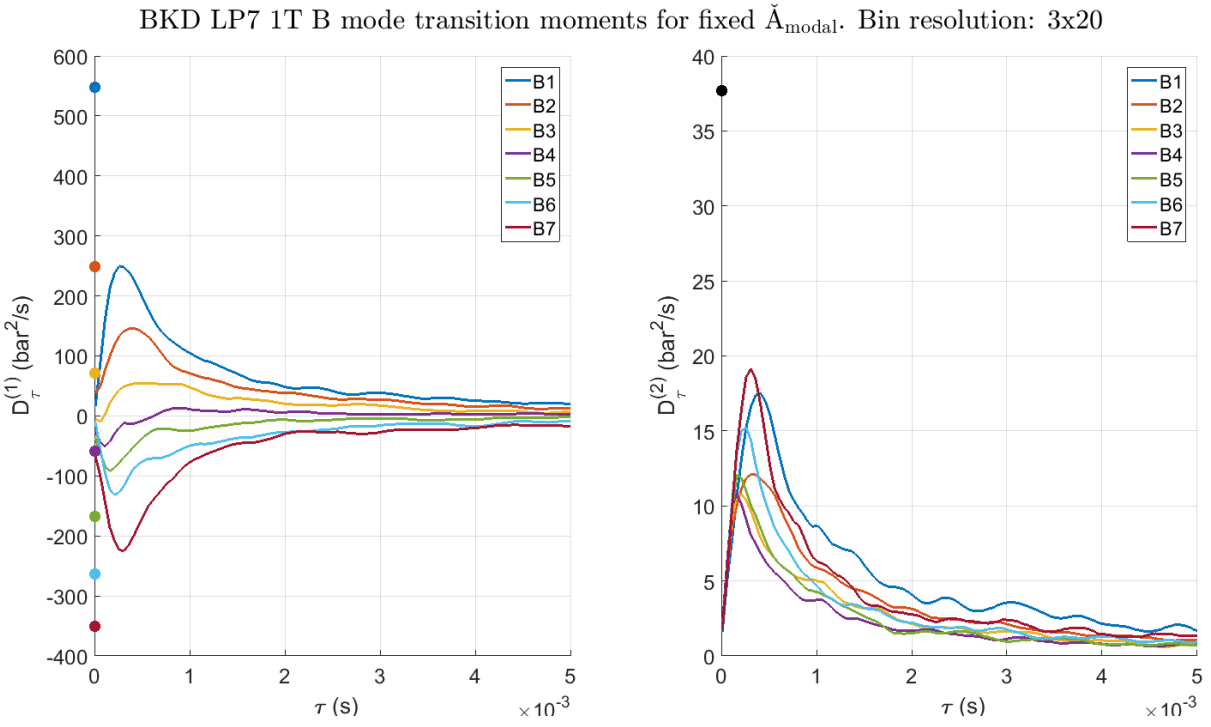

Figure 86: BKD LP7 1T B mode transition moments for the modal (m) value of B̆. Bin resolution: 3x20.

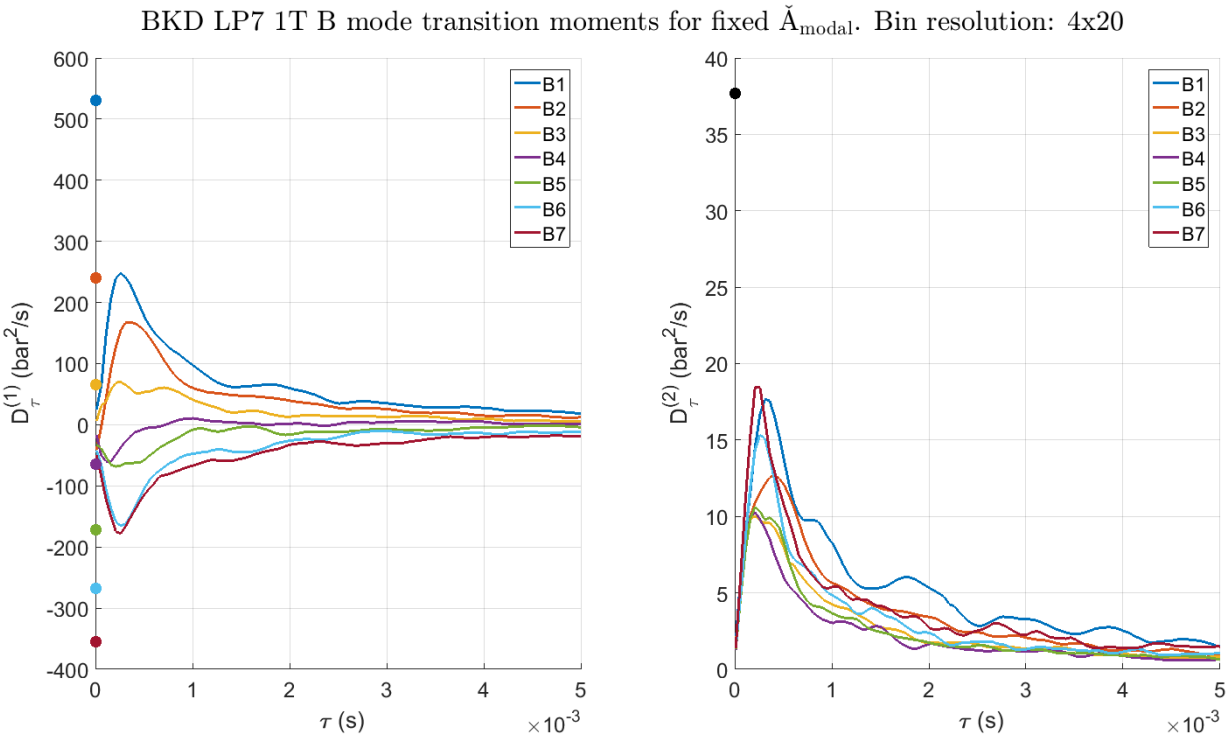

Figure 87: BKD LP7 1T B mode transition moments for the modal (m) value of B̆. Bin resolution: 4x20.

References

Bendat, J. S., & Piersol, A. G. (2010). *Random Data: Analysis and Measurement Procedures, Fourth Edition.* Hoboken: John Wiley & Sons, Inc.

Bonciolini, G., Boujo, E., & Noiray, N. (2017). Output-only parameter identification of colored-noise-driven Van-der-Pol oscillator: Thermoacoustic instabilities as an example. *Physical Review E , 95*, 1-15.

Boujo, E., & Noiray, N. (2017). Robust identification of harmonic oscillator parameters using the adjoint Fokker-Planck equation. *Proceedings of the Royal Society A , 473*, 1-18.

Boujo, E., Denisov, A., Schuermans, B., & Noiray, N. (2016). Quantifying acoustic damping using flame chemiluminescence. *Journal of Fluid Mechanics , 808*, 245-257.

CPIA. (1997). *Guidelines for Combustion Stability Specification and Validation Procedures for Liquid Rocket Engines.* Columbia Maryland: Chemical Propulsion Information Agency Publication.

Culick, F. E., & Yang, V. (1995). *Overview of Combustion Instabilities in Liquid-Propellant Rocket Engines.* New York: Progress in astronautics and aeronautics: an American Institute of Aeronautics and Astronautics series.

Groning, S., Hardi, J., Suslov, D., & Oschwald, M. (2016). Injector-driven combustion instabilities in a hydrogen/oxygen rocket combustor. *Journal of Propulsion and Power , 32*, 560-573.

Groning, S., Suslov, D., Oschwald, M., & Sattelmayer, T. (2013). Stability behaviour of a cylindrical rocket engine combustion chamber operated with liquid hydrogen and liquid oxygen. Munich: 5th European Conference for Aeronautics and Space Sciences.

Hardi, J. S. (2012). *Experimental Investigation of High Frequency Combustion Instability in Cryogenic Oxygen-Hydrogen Rocket Engines.* PhD Thesis: University of Adelaide.

Lord Rayleigh, J. (1945). *The Theory of Sound* (2nd ed.). New York : Dover Publications.

Mayer, W., & Tamura, H. (1996). Propellant injection in a liquid oxygen/gaseous hydrogen rocket engine. *Journal of Propulsion and Power , 12*, 1137-1147.

Miller, K., Sisco, J., Nugent, N., & Anderson, W. (2005). Experimental study of combustion instabilities in a single-element coaxial swirl injector . *41st AIAA/ASME/SAE/ASEE Joint Propulsion Conference & Exhibit.* Tucson Arizona.

Noiray, N. (2017). Linear Growth Rate Estimation from Dynamics and Statistics of Acoustic Signal Envelope in Turbulent Combustors. *Journal of Engineering for Gas Turbines and Power , 139*, 1-11.

Noiray, N., & Denisov, A. (2016). A method to identify thermoacoustic growth rates from dynamic pressure time series. *Proceedings of the Combustion Institute , 36*, 3843-3850.

Noiray, N., & Schuermans, B. (2013). Deterministic quantities characterizing noise driven Hopf bifurcations in gas turbine combustors. *International Journal of Non Linear Mechanics , 50*, 152-163.

Noiray, N., & Schuermans, B. (2013). On the dynamic nature of azimuthal thermoacoustic modes in annular gas turbine combustion chambers. *Proceeedings of the Royal Society A , 469*, 1-15.

Schulze, M. (2016). *Linear Stability Assessment of Cryogenic Rocket Engines.* PhD Thesis: Technical University of Munich.

Webster, S. L. (2016). *Analysis of Pressure Dynamics, Forced Excitation and Damping in a High Pressure LOx/H2 Combustor.* PhD thesis: Aachen University.

Webster, S., Hardi, J., & Oschwald, M. (2015). Characterisation of acoustic energy content in an experimental combustion chamber with and without external forcing. *CEAS Space Journal , 7*, 1-15.